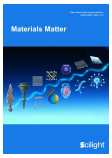
Scilight

Materials Matter

https://www.sciltp.com/journals/mm



Review

Check for updates

Dynamic Machine Learning for the Oxygen Evolution Reaction: From Static Catalyst Screening to Working-State Trajectory Learning

Zihang Zhao [1,2], Keyi Xiang [1,2,3], Chengxu Zhang [1] and Jue Hu [1,2,3,*]

[1] School of Metallurgical and Energy Engineering, Kunming University of Science and Technology, Kunming 650093, China
[2] Key Laboratory of Unconventional Metallurgy, Kunming University of Science and Technology, Kunming 650093, China
[3] Southwest United Graduate School, Kunming 650092, China
* Correspondence: hujue@kust.edu.cn

How To Cite: Zhao, Z.; Xiang, K.; Zhang, C.; et al. Dynamic Machine Learning for the Oxygen Evolution Reaction: From Static Catalyst Screening to Working-State Trajectory Learning. *Materials Matter* **2026**, *1*(1), 7. https://doi.org/10.53941/mm.2026.100007

Received: 6 August 2026
Revised: 10 September 2026
Accepted: 24 September 2026
Published: 8 October 2026

Abstract: Efficient water electrolysis is limited not only by the sluggish kinetics of the oxygen evolution reaction (OER), but also by the dynamic reconstruction and degradation of catalysts under operating bias. Machine learning (ML) has accelerated OER catalyst screening by linking precursor composition, structural descriptors and adsorption energetics to endpoint activity, yet static endpoint models cannot determine when a working interface forms, how reaction pathways redistribute, or where stability costs accumulate during operation. This Review does not treat catalyst reconstruction or ML-assisted operando analysis as new concepts; instead, it formalizes their intersection as a supervised trajectory-learning problem. We define dynamic OER ML operationally as learning in which ordered operating history enters the prediction and the target contains at least one time-resolved state, transition event, pathway redistribution, degradation event or transfer trajectory. The field is organized around three learning targets: active-interface formation from precursors, coupled evolution of OER mechanisms and degradation routes, and transfer of material behavior across pH, electrolyte, potential program, transport and device boundaries. Static ML is repositioned as a source of precursor priors, whereas dynamic ML must learn state transitions, rates, latent working states, uncertainty and protocol-dependent transfer from time-resolved evidence. We further provide operational routes from raw operando signals to quantitative labels, target-specific evaluation metrics, baseline comparisons and leakage-safe validation rules. By shifting OER learning from material-endpoint ranking to material-condition-trajectory prediction, dynamic ML can support the prediction, preservation and control of real catalyst working states.

Keywords: oxygen evolution reaction; dynamic machine learning; working-state trajectories; active-state reconstruction; mechanism–degradation coupling; trajectory-resolved datasets

1. Introduction

Green hydrogen is increasingly considered an important decarbonization option for hard-to-abate sectors, particularly iron and steel and chemical production, although its climate value depends strongly on the production route and on the specific fossil process it replaces [1–5]. Renewable-powered water electrolysis provides a direct route for coupling low-carbon electricity to hydrogen production [6–8]. However, the overall efficiency of water electrolysis is still strongly constrained by the oxygen evolution reaction (OER). This anodic half-reaction involves

Copyright: © 2026 by the authors. This is an open access article under the terms and conditions of the Creative Commons Attribution (CC BY) license (https://creativecommons.org/licenses/by/4.0/).
Publisher's Note: Scilight stays neutral with regard to jurisdictional claims in published maps and institutional affiliations.

four-electron transfer, multiple proton-coupled steps, high kinetic barriers and continuous changes at the catalyst/electrolyte interface. These features make OER catalyst design different from a simple search for a material with a favorable pristine structure-activity relationship. The more fundamental question is how the initially loaded catalyst evolves into the working state that actually carries current, and how this state can be identified, predicted and preserved [9].

Machine learning (ML) is naturally attractive for this problem because it can connect composition, structure, electronic descriptors and catalytic performance across chemical spaces that are too large for exhaustive experimental exploration. Descriptor-based modeling, high-throughput computation and data-driven screening have already shown that ML can accelerate OER catalyst discovery, extract composition-property trends and guide candidate selection [10–13]. In this role, ML has greatly improved the efficiency of static catalyst screening. However, the target learned by most current models remains relatively narrow. Many studies still use static inputs and endpoint labels, such as precursor composition, calculated adsorption energies, measured overpotential or stability retention after testing [14,15]. These models are useful for ranking candidates, but they do not directly describe how a catalyst enters, maintains or loses its working state during OER.

The need for this distinction has become increasingly clear from operando and *in situ* studies. Many OER catalysts are not fixed solids under reaction conditions. Under anodic bias, they can reconstruct, leach, hydrate, change valence, form oxyhydroxide layers, redistribute active sites or undergo pathway-dependent degradation [16–23]. These processes are not merely post-reaction modifications. They can determine which phase is active, which OER pathway is favored and which degradation route is opened. Therefore, activity and durability are governed not only by the pristine composition or a final performance value, but also by the operating history through which the active interface is generated.

The current literature has already established both foundations on which this Review builds. Operando and *in situ* OER studies have shown that the pristine structure is not necessarily the current-carrying working catalyst, and dedicated reviews have summarized reconstruction, active-species identification and time-resolved mechanistic characterization [24,25]. In parallel, artificial intelligence, machine learning, high-throughput experimentation and data-mining workflows are increasingly being combined with electrocatalyst characterization and discovery [26,27]. These developments are therefore not claimed here as new. The narrower unresolved gap is operational: there is still no broadly adopted mapping from evolving catalyst evidence to supervised trajectory targets, quantitative labels, prediction horizons, evaluation metrics and leakage-safe transfer tests. Accordingly, the key learning question is not whether catalysts evolve or whether ML can analyze operando data, but what an ML model should predict from that evolution, from which information, over what time horizon, and by what quantitative standard success should be judged.

In this Review, dynamic ML denotes a learning problem in which the prediction explicitly depends on ordered operating history and the target contains at least one time-resolved state variable, transition event, pathway redistribution, degradation event or transfer trajectory. A workflow is not classified as dynamic ML merely because it uses automation, active learning, Bayesian optimization, reinforcement learning or time-stamped measurements if the learned target remains a static endpoint. Thus, composition-to-overpotential regression and closed-loop searches that optimize only final activity remain endpoint-learning tasks, whereas early operando signals used to predict later reconstruction, waveform histories used to forecast dissolution onset, or multimodal measurements used to infer pathway weights versus time are dynamic-learning tasks. Formally, each record contains a precursor state x_0, an operating history $u(0{:}\tau)$, observations $m(0{:}\tau)$ available before a fixed prediction horizon τ, and a future response $y(\tau{:}T)$.

This Review addresses that operational gap by treating OER catalyst design as a trajectory-learning problem [28–37]. We focus on three linked issues: which active states can be accessed from a given precursor, how OER mechanisms and degradation co-evolve under operating conditions, and when material behavior can transfer across protocols, electrolytes and device environments. In this framework, static ML is not discarded; instead, it is repositioned as a precursor prior that estimates chemical accessibility, stability risk and local structural propensity. The missing task is dynamic learning: to learn and test how catalyst states change under defined operating histories (Figure 1). Therefore, the central contribution of this Review is not a new claim that catalysts reconstruct, nor a new claim that ML can be combined with operando measurements, but a formalization of the supervised object from a material-endpoint pair to a material-condition-trajectory record. Through active-interface formation, mechanism-degradation coupling and cross-protocol/device transfer, we specify what should be measured, labelled, predicted and validated for working-state trajectories to become reusable learning objects.

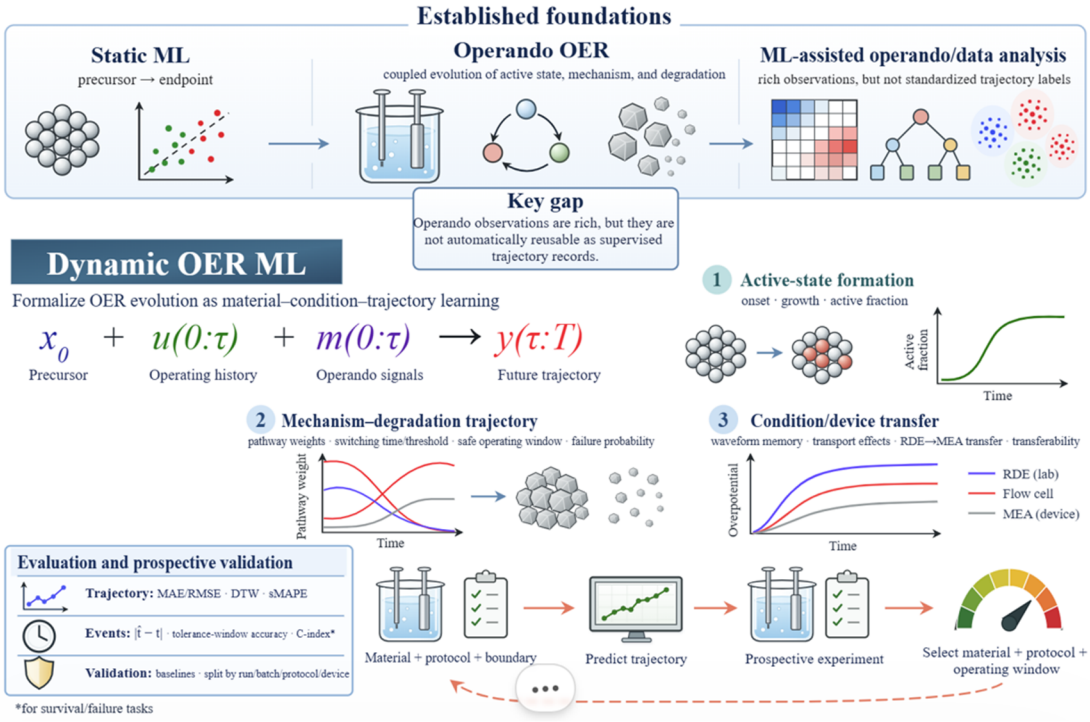


Figure 1. Conceptual framework of dynamic machine learning for the oxygen evolution reaction (OER). Static ML, operando characterization, and ML-assisted operando/data analysis provide established foundations, but time-resolved observations are not automatically reusable as supervised trajectory records. Dynamic OER ML formalizes catalyst evolution as material–condition–trajectory learning, using the precursor state, operating history, and operando signals before a fixed prediction horizon to predict future working-state trajectories. The framework focuses on active-state formation, mechanism–degradation trajectories, and condition/device transfer, with trajectory-specific evaluation, leakage-safe validation, and prospective material–protocol optimization.

2. From Precursors to Working States: Learning Active-Interface Formation

The precursor is not the catalyst identity; it is the starting condition from which the working interface is selected. Under anodic polarization, an oxide, hydroxide or perovskite can oxidize, hydrate, leach, exchange ions with the electrolyte, or form a spatially confined surface layer [38–43]. The sharper question is which reconstructed state carries current, how it is reached, and where the precursor still matters after that state appears. This section treats active-state formation as the first trajectory-learning problem. Static models define chemical accessibility; dynamic models must resolve onset, growth, self-termination, spatial propagation and reversibility. The section separates the phenomenon, the static precursor prior, the current state of dynamic ML and the route toward learnable state-transition rules (Figure 2).

2.1. Precursor Transformation Redefines Active-Site Identity

Active-state formation changes the object that structure-activity relationships are supposed to explain. When the active phase is generated during operation, a correlation between the pristine phase and the final overpotential no longer has a single meaning. It may reflect the accessibility of the precursor, the efficiency of the activation process, or the performance of the newly formed working state. These contributions must be separated before ML can make a mechanistic claim. Active-state formation is therefore not an auxiliary phenomenon in OER catalysis. It is the process by which the working catalyst is selected from the precursor under potential, electrolyte and transport constraints.

This selection does not follow a single route. In some catalysts, the precursor is converted into an oxyhydroxide active layer. In others, selective leaching removes unstable species and may be followed by redeposition from the electrolyte. In defect-rich materials, local vacancies, strain or low-coordination motifs open the pathway to reconstruction. At the particle or electrode scale, surface and bulk regions can transform at different rates, leaving a spatially heterogeneous working state. These four routes—oxyhydroxide active-layer formation, selective leaching and redeposition, defect-gated reconstruction, and spatially asynchronous surface-bulk evolution—define the main ways in which an active state is generated during OER (Figure 3) [44–50]. They are discussed separately below because each route creates a different ML target: formation onset and converted

fraction, productive versus destructive metal loss, defect-triggered transition probability, or the spatial distribution of current-carrying domains.

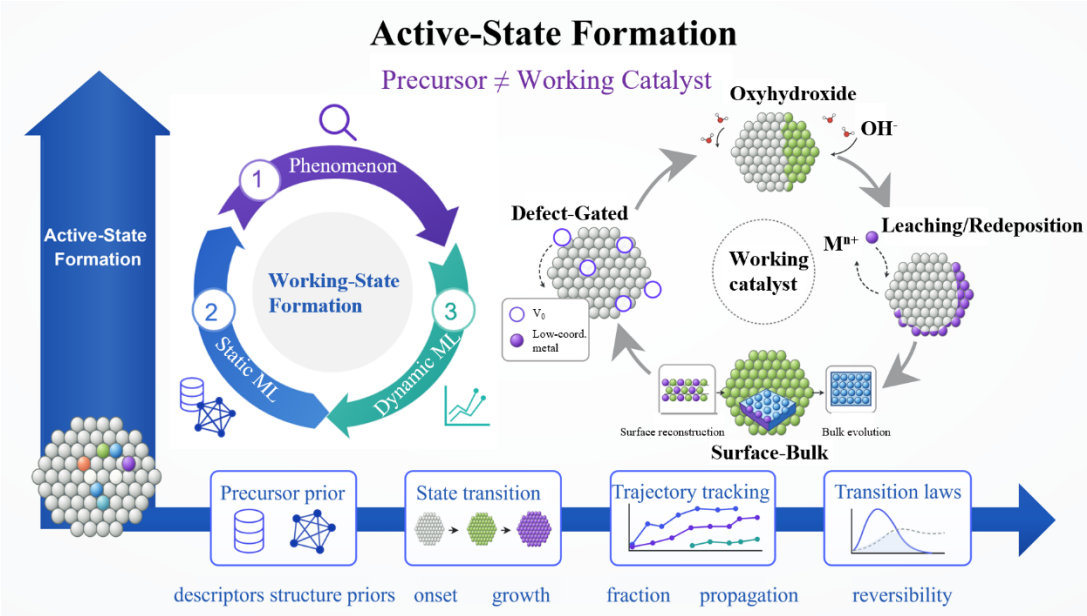


Figure 2. Active-state formation in dynamic OER machine learning. The precursor serves as the starting state rather than the working catalyst. During OER, it evolves through oxyhydroxide formation, leaching/redeposition, defect-gated reconstruction and asynchronous surface–bulk evolution. Static ML provides precursor priors, while dynamic ML learns transition variables such as onset, growth, active-phase fraction, propagation and reversibility.

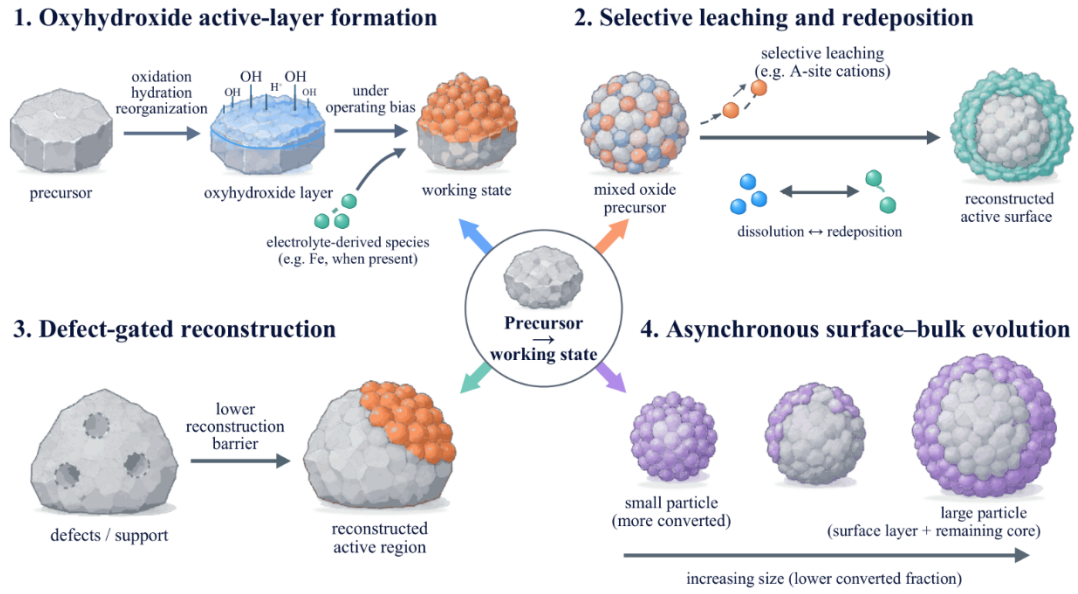


Figure 3. Active-state formation pathways in dynamic OER. The precursor-defined structure can transform into the real working state through oxyhydroxide active-layer formation, selective leaching/redeposition, defect-gated reconstruction, and asynchronous surface–bulk evolution.

2.1.1. Oxyhydroxide Layers as Generated Active Interfaces

Oxyhydroxide formation changes the chemical identity of the current-carrying surface. In many alkaline OER catalysts, the precursor becomes catalytically relevant only after oxidation, hydration and reorganization into a metal-oxygen-hydrogen network. The first rule is therefore straightforward: activity follows the generated coordination environment, not the nominal precursor formula. NiFe catalysts make this rule unavoidable. Trotochaud et al. showed that both intentional Fe addition and incidental Fe uptake from KOH electrolyte strongly reshape the OER behavior of NiOOH-type films (Figure 4a) [51]. In Fe-purified electrolyte, NiOOH remains a

poor OER catalyst, whereas trace Fe can enter the hydrated NiOOH film during cycling, or even during electrolyte exposure without applied potential, and progressively increases OER current. This means that a nominally Fe-free NiOOH precursor can become a NiFeOOH working surface during the test itself. Fe addition also increases film conductivity, but this alone cannot explain the activity enhancement, indicating that Fe must be considered as part of the generated active oxyhydroxide environment rather than as a simple conductivity modifier. Friebel et al. further identified the local active structure by combining operando X-ray absorption spectroscopy, electrochemistry and theory (Figure 4b) [52]. They showed that the highly active sites are Fe centers incorporated into γ-NiOOH, where edge-sharing with surrounding NiO_6 octahedra produces a shortened Fe-O coordination environment and near-optimal adsorption energetics for OER intermediates. Thus, Fe becomes catalytically meaningful only after it enters the NiOOH host and adopts the working-state coordination imposed by anodic bias. The transition record should therefore retain Fe source, Fe-entry time, oxidized NiOOH fraction, local Fe–O coordination and persistence after electrolyte exchange. Final overpotential alone would merge Fe uptake, host oxidation, active-site formation and surface conversion into one endpoint. The learnable object is the sequence linking precursor accessibility to active-layer population.

The second rule is that precursor geometry controls the route into the oxyhydroxide state. Wang et al. identified geometrical-site-dependent activity in spinel Co_3O_4 under operando conditions [53], while Zhou et al. electrochemically accessed ultrathin Co (oxy)hydroxide nanosheets from a $Na_xCoFe(CN)_6$ precursor and identified their working-state phase during OER (Figure 4c) [54]. Under oxidative treatment in alkaline solution, the molecular precursor is degraded by the electric field: Co and Fe dissociate from the cyanide framework, Fe dissolves into the electrolyte, and hydroxyl groups are driven to the anode to reconstruct the remaining Co species into ultrathin CoOOH nanosheets. Operando Co K-edge XAS further showed that this nanosheet surface does not enter OER as a fixed CoOOH phase. Below a critical potential of about 1.40 V, oxygen vacancies are filled by hydroxyl groups and the Co coordination number increases toward a saturated Co–O environment. Above this potential, CoOOH undergoes potential-dependent deprotonation to form a $Co^{3+/4+}OOH_{1-x}$ active phase, accompanied by Co-O bond contraction and oxidized oxygen character. Thus, the important variable is not only the final CoOOH nanosheet morphology, but the route by which precursor degradation, hydroxyl filling and deprotonation generate the active surface.

Kanan and Nocera push the same rule beyond a closed solid: their cobalt-phosphate oxygen-evolving film forms *in situ* from dissolved Co^{2+} and phosphate species under oxidative polarization in neutral water (Figure 4d) [55]. In phosphate buffer containing Co^{2+}, an initially inert ITO electrode develops catalytic current only after anodic polarization, during which a dark amorphous Co-phosphate oxide/hydroxide film gradually deposits on the electrode. The current increases together with film growth, and the deposited material contains Co, phosphate, K and O, showing that phosphate is not only a spectator electrolyte but part of the working catalyst environment. The pH dependence further suggests that hydrogen phosphate participates in proton removal during OER. This case shows that the working surface can be assembled and repaired during electrolysis by potential, solution Co^{2+} reservoir, phosphate participation and local deposition chemistry. A dataset that records only the initially loaded solid would therefore miss the actual formation route, growth history and repair current of the active catalyst.

Taken together, oxyhydroxide formation follows a compact rule: the precursor controls access not only through composition, but also through geometrical-site distribution, exposed coordination motifs and the route by which the surface enters the oxyhydroxide state; the electrolyte can supply or reshape matter; and the operating potential selects the coordination environment that carries current. Dynamic OER datasets therefore need formation onset, active-layer fraction, geometry-dependent conversion sites, electrolyte-derived uptake, local M-OH/M-O coordination, layer connectivity and saturation behavior [56–60]. These variables separate intrinsic precursor quality, geometry-enabled activation and potential-driven working-state selection, thereby preventing slow-forming but promising materials from being discarded as inactive.

2.1.2. Selective Leaching, Redeposition and Surface Selection

After oxyhydroxide formation, a second route to active-state generation is more counterintuitive: the catalyst may become active by losing part of itself. Leaching becomes catalytic only when atom removal selects a current-carrying interface faster than it destroys the supporting framework. Seitz et al. illustrated this productive route in $IrO_x/SrIrO_3$, where Sr depletion under acidic OER generates an IrO_x-rich surface during electrochemical testing (Figure 5a–d) [61]. The starting perovskite matters because $SrIrO_3$ can lose the less stable Sr component while retaining a connected Ir-O framework. During the first stage of testing, the activity increases as Sr is removed: XPS shows a rapid decrease of surface Sr while the Ir signal remains nearly constant, and depth profiling indicates that Sr depletion is concentrated near the catalyst surface. XRD further shows that the bulk $SrIrO_3$ film largely

preserves its crystalline framework after OER, so the process is not complete dissolution but selective surface transformation. DFT calculations support this interpretation by suggesting that Sr-deficient surfaces can form highly active IrO_x motifs, such as anatase-like IrO_2 or IrO_3-like overlayers, that are stabilized by the underlying $SrIrO_3$ lattice. These observations define the useful label: leaching depth, Sr-removal rate, retained Ir-O connectivity, surface IrO_x motif, hydration state and current after shell formation. A record that stores only dissolved Sr or post-test composition would call the process corrosion; a trajectory record recognizes controlled surface selection.

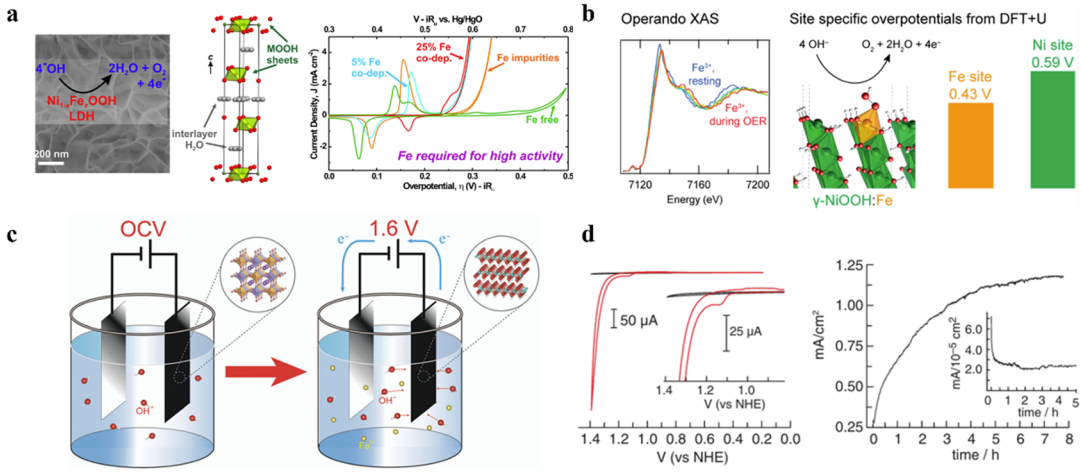


Figure 4. (**a**) Promotional effect of Fe on Ni-based OER electrocatalysts. Adapted with permission from Ref. [51]. Copyright 2014, American Chemical Society. (**b**) Operando HERFD-XANES shows that Fe^{3+} undergoes structural rearrangement during OER, with shortened Fe-O bonds. DFT + U calculations reveal a much lower overpotential at Fe sites (0.43 V) than at Ni sites (0.59 V), identifying Fe as the active center for water oxidation, while Ni is inactive. Adapted with permission from Ref. [52]. Copyright 2015, American Chemical Society. (**c**) The *in situ* electrochemical fabrication of CoOOH-NS. Adapted with permission from Ref. [54]. Copyright 2019, Royal Society of Chemistry. (**d**) Electrochemical characterization of cobalt-based water oxidation in neutral phosphate buffer. Adapted with permission from Ref. [55]. Copyright 2008, The American Association for the Advancement of Science.

Leaching often becomes exchange chemistry rather than simple material loss. Lopes et al. showed this in $La_{1-x}Sr_xCoO_3$ perovskites, where OER cycling does not leave the original perovskite surface intact but converts the near-surface region into a CoO_xH_y-like shell that interacts with trace Fe from the alkaline electrolyte (Figure 5e) [62]. In purified KOH, different Sr contents show little intrinsic activity difference, whereas adding trace Fe and cycling to OER potentials strongly activates the Sr-doped samples, with faster activation at higher Sr content. Identical-location STEM and EELS further show a sequence of ordered oxygen-vacancy formation, surface amorphization and Fe localization near Co-rich reconstructed regions. Meanwhile, *in situ* ICP-MS confirms selective Sr dissolution from the A-site, while Raman identifies the evolved surface as Co hydr(oxy)oxide species. The active interface is therefore assembled by solid–electrolyte exchange: A-site Sr leaves, oxygen defects and hydration reorganize the surface, a CoO_xH_y shell forms, and Fe species are dynamically retained at this shell to promote OER. For learning, this pathway should be encoded by A-site loss, Sr-dissolution rate, oxygen-vacancy formation, foreign-ion uptake, hydration, Co–OH/Fe–O coordination and persistence of the CoO_xH_y-like shell.

Productive leaching also needs a stopping rule. Wu et al. provided this boundary in $CoAl_2O_4$, where Fe facilitates dynamic active-site generation while the spinel architecture limits how far reconstruction proceeds [63]. This case is more precise than a generic Fe-promotion story. Fe helps initiate an active surface, but the residual lattice preserves the framework needed for charge transport. The mechanistic value lies in self-termination, which separates bounded activation from destructive corrosion. The useful descriptors are onset potential, Fe-assisted conversion rate, reconstructed-shell thickness and residual-lattice conductivity.

Taken together, selective leaching should be treated as a surface-selection process rather than as simple corrosion. In $SrIrO_3$-derived $IrO_x/SrIrO_3$, useful atom loss is defined by Sr removal, Ir–O framework retention and formation of an IrO_x-rich active shell. In Sr-substituted cobalt perovskites, leaching becomes solid–electrolyte exchange, where A-site dissolution, oxygen-defect formation, hydration and Fe uptake jointly generate a CoO_xH_y-like working shell. In $CoAl_2O_4$, productive reconstruction further requires a stopping rule, because Fe-assisted active-site generation is useful only when the residual spinel framework limits excessive transformation and

preserves charge transport. Therefore, the path classes for learning are controlled surface selection, electrolyte-assisted exchange/redeposition, self-terminated reconstruction and destructive loss [64–69]. The corresponding trajectory variables are leaching onset, leaching depth, dissolution flux, retained metal–oxygen connectivity, surface-shell composition, foreign-ion uptake, redeposition or retention rate, shell-growth saturation, self-termination depth and current retention after surface selection. Without these distinctions, activity-stability datasets collapse productive leaching, dynamic repair and irreversible corrosion into the same endpoint number.

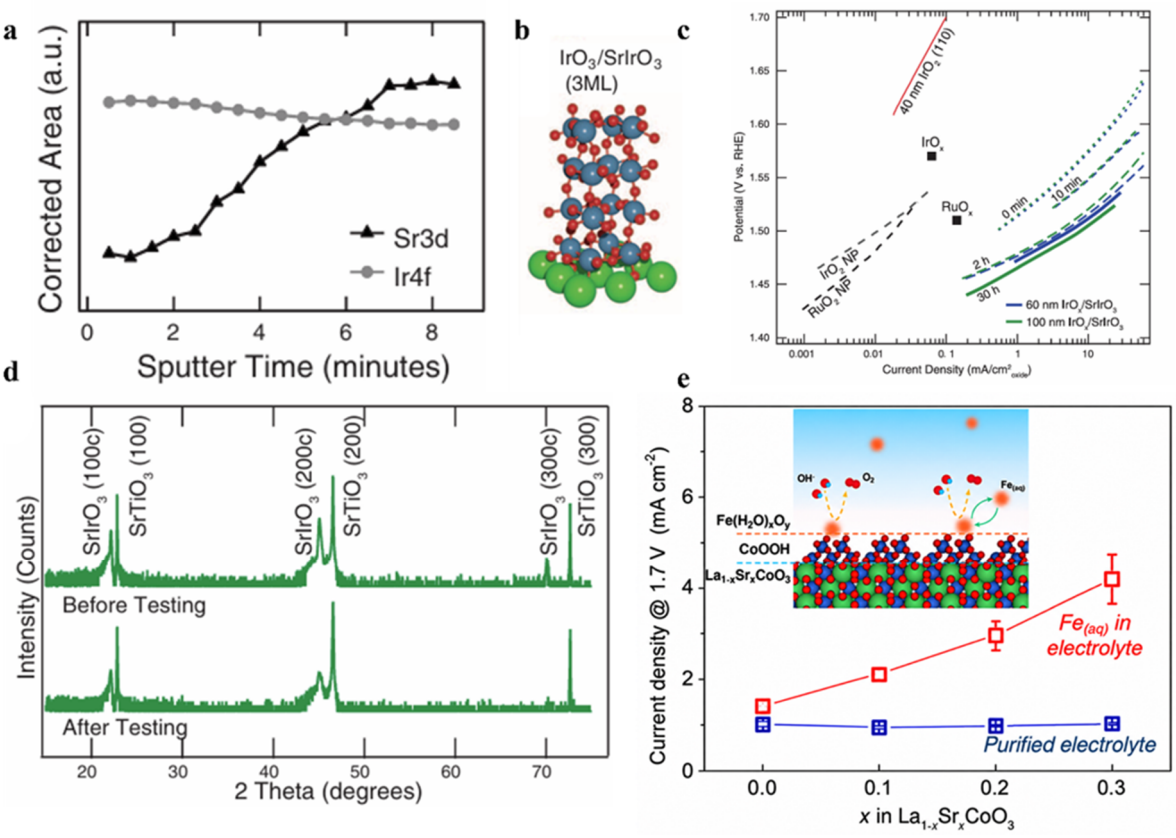


Figure 5. (**a**) XPS depth sputtering elemental distribution profile, quantitatively measuring Sr leaching depth and stable Ir signal across film depth to distinguish controlled surface reconstruction from indiscriminate material corrosion. Adapted with permission from Ref. [61]. Copyright 2016, The American Association for the Advancement of Science. (**b**) DFT structural model of three monolayers Sr-leached IrO_3 overlayer anchored on $SrIrO_3$ perovskite substrate, illustrating retained Ir-O octahedral framework and high-activity hydrated IrO_x surface layer. Adapted with permission from Ref. [61]. Copyright 2016, The American Association for the Advancement of Science. (**c**) Tafel plot comparing intrinsic OER specific activity of $IrO_x/SrIrO_3$ films at different cycling durations against benchmark acidic OER catalysts, demonstrating enhanced catalytic current following Sr surface leaching and IrO_x active shell formation. Adapted with permission from Ref. [61]. Copyright 2016, The American Association for the Advancement of Science. (**d**) XRD patterns of as-prepared and post-OER $SrIrO_3$ thin films, confirming preservation of bulk perovskite $SrIrO_3$ crystalline lattice after electrochemical cycling, verifying intact Ir-containing backbone. Adapted with permission from Ref. [61]. Copyright 2016, The American Association for the Advancement of Science. (**e**) Combined atomic interface schematic and electrochemical plot summarizing the OER activation mechanism of Sr-substituted $LaCoO_3$. Sr dissolution drives CoO_xH_y surface layer generation, and trace Fe in electrolyte drastically elevates catalytic current with increasing Sr doping level. Adapted with permission from Ref. [62]. Copyright 2021, American Chemical Society.

2.1.3. Defect-Gated Access to Reconstructed States

Defects are useful only when they change the path into the working state. Yet a defect is not automatically an active site. It may lower the barrier to reconstruction, provide a temporary charge reservoir, open an ion-transport channel, or mark the beginning of irreversible disorder. The mechanistic question is not whether defects exist, but what they do under potential.

Defect-controlled reconstruction is a transition problem, not a defect-count problem. Song et al. used operando X-ray spectroscopy to follow the self-reconstruction of La_2O_3-anchored CoFe nanoparticles during OER

(Figure 6a) [70]. The initial exsolved nanoparticles were not fixed metallic active sites. Under OER potential, the CoFe species progressively lost their metallic coordination and evolved into an amorphous, coordination-unsaturated (Co/Fe)O(OH) layer, which acted as the real working state. The La_2O_3 support promoted this conversion and helped keep the reconstructed phase at the particle–support interface. Thus, the nanoparticle was a moving object: its coordination, oxidation state and interfacial environment evolved while current was flowing. Kim et al. then showed that anchoring can reduce the barrier for self-reconstruction in cobalt nanoparticles (Figure 6b) [71]. In Co nanoparticles anchored on conductive yttrium ruthenate pyrochlore, the support did more than disperse the metal particles. Redox-active Y and Ru sites provided an electron-transfer pathway during Co oxidation, promoted OH^- adsorption and facilitated the formation of CoOOH-like intermediates. Anchoring therefore acted as a reconstruction gate: it controlled how easily metallic Co entered the oxyhydroxide working state and whether the transformed region remained electrically connected. Together, these studies shift the focus from defective nanoparticles to reconstruction gates. Support-particle contact can decide how easily the active state is reached, where the transformed region is confined and whether the new phase stays electrically connected. Zhang et al. added defect specificity by tracking how different defect types in Co_3O_4 influence structural evolution and active motifs during OER (Figure 6c) [72]. Oxygen vacancies and cobalt vacancies did not simply increase the number of "defective sites"; they changed different elementary steps of reconstruction. Oxygen vacancies strengthened *OH adsorption but weakened deprotonation, accelerating irreversible reconstruction, whereas cobalt vacancies favored dehydrogenation and slowed excessive structural transformation. Both routes generated reconstructed CoO_xH_y-like active motifs, but the Co-vacancy route produced a compressed bridge-Co configuration with a shorter Co-Co distance and higher OER activity. The useful record is therefore defect class, local environment, support contact, transition onset, reconstruction rate, and whether the defect survives, heals or disappears after reconstruction.

Taken together, defects should be treated as reconstruction gates rather than as a simple count of active sites [73–76]. In La_2O_3-anchored CoFe nanoparticles, the support-assisted interface controls the conversion from metallic coordination to a coordination-unsaturated (Co/Fe)O(OH) working layer. In pyrochlore-anchored Co nanoparticles, anchoring lowers the reconstruction barrier and helps maintain electronic connectivity during CoOOH formation. In defective Co_3O_4, oxygen vacancies and cobalt vacancies guide different reconstruction pathways, leading to different degrees of irreversibility and different active motifs. The learnable variables are therefore defect class, local coordination, support contact, reconstruction onset, barrier/cost of conversion, spatial confinement, connectivity of the reconstructed region, and whether the defect survives, heals or disappears after reconstruction. This distinction prevents a common error in data-driven catalyst design: attributing high activity to more defects when the real variable is whether a specific defect population generates a connected and durable working state.

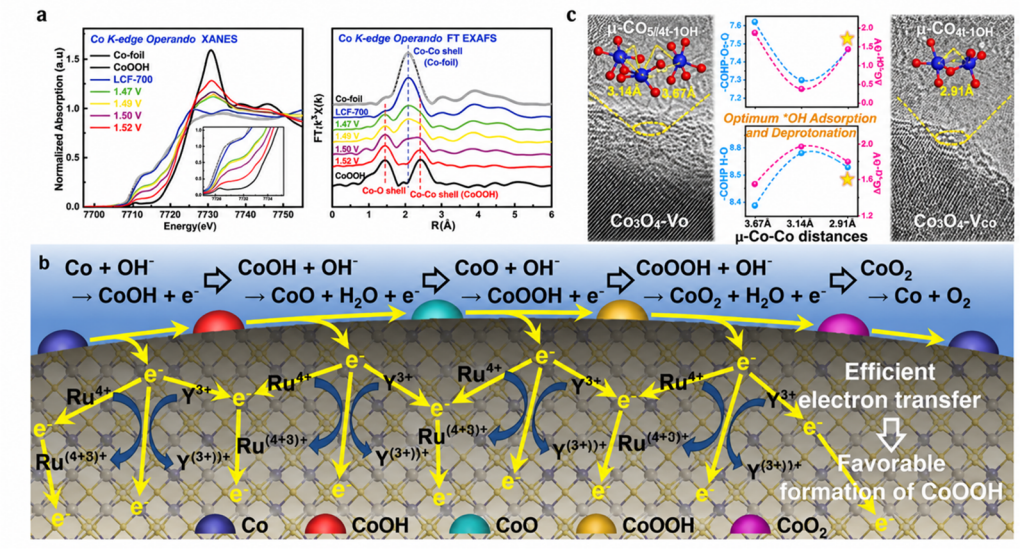


Figure 6. (**a**) Operando X-ray absorption spectroscopy tracking the self-reconstruction of La_2O_3-anchored CoFe nanoparticles into an amorphous, coordination-unsaturated (Co/Fe)O(OH) working layer during OER. Adapted with permission from Ref. [70]. Copyright 2018, Royal Society of Chemistry. (**b**) Schematic depicting the pyrochlore-mediated electron transfer pathway that lowers the self-reconstruction barrier of anchored Co nanoparticles to generate CoOOH active layers during OER. Adapted with permission from Ref. [71]. Copyright 2019, John Wiley and Sons. (**c**) Atomic and theoretical comparison of reconstructed oxygen- and cobalt-vacant Co_3O_4, illustrating how different lattice defects alter Co-Co bridge geometry, *OH binding thermodynamics and

resultant OER activity after surface reconstruction. Adapted with permission from Ref. [72]. Copyright 2023, American Chemical Society.

2.1.4. Spatially Asynchronous Surface–Bulk Evolution

Spatial asynchrony makes the active state a distribution rather than a single phase. Under the same applied current, surface layers, edges, particle interiors and support-contact regions can enter different states at different rates. Therefore, the working catalyst should not be described only by an electrode-average oxidation state or a single reconstructed phase. The key variable is the spatially connected fraction of the active state: how much of the material has reached the OER-adapted structure, where that transformed region is located, and whether it remains connected to electron transport, electrolyte access and gas release. Haase et al. made this problem concrete through size-dependent active-state formation in cobalt oxide nanoparticles (Figure 7a–c) [77]. By using size-selected $CoO_x(OH)_y$ nanoparticles from about 1 to 9 nm and tracking them with operando X-ray absorption spectroscopy, they showed that decreasing particle size increases both mass activity and specific activity, especially in the sub-5 nm regime. This cannot be explained only by a larger surface area. During electrochemical activation, the nanoparticles converged toward a CoOOH-like structure with mainly di-μ-oxo-bridged Co motifs. Under OER conditions, they underwent reversible Co oxidation and Co-O bond contraction, and both effects became stronger as particle size decreased. This size dependence means that smaller particles can reorganize over a larger fraction of their volume, whereas larger particles mainly develop an OER-adapted near-surface region while retaining a less-transformed interior. In an electrode containing a distribution of particle sizes, the measured spectrum therefore averages fully adapted small particles, partially transformed larger particles, residual cores and transient surface domains. A modest average Co oxidation-state shift may still hide a small population of highly connected OER-active domains carrying most of the current. This converts particle size, surface-to-volume ratio, reversible Co–O contraction, oxidized-layer persistence, core–shell contrast and electrically connected reconstructed fraction into the key spatial descriptors.

Taken together, spatially asynchronous surface–bulk evolution should be treated as a connectivity-selection process rather than as a uniform phase transformation. In size-selected $CoO_x(OH)_y$ nanoparticles, small particles can reorganize over a larger volume fraction and approach a CoOOH-like working state, whereas larger particles mainly develop an OER-adapted surface region while retaining a less-transformed core. Therefore, the measured average oxidation state, average Co–O bond contraction or average reconstructed fraction may obscure the minority domains that actually carry most of the current. The learnable variables are particle-size population, surface-to-volume ratio, core–shell contrast, propagation depth, oxidized-layer persistence, electrically connected reconstructed fraction and current contribution from each domain. Activity follows the connected fraction of the working state, not the average extent of reconstruction [78–81]. Without these spatial labels, dynamic OER datasets may incorrectly treat electrode-averaged reconstruction as the active state, while missing the small but connected domains that dominate OER performance.

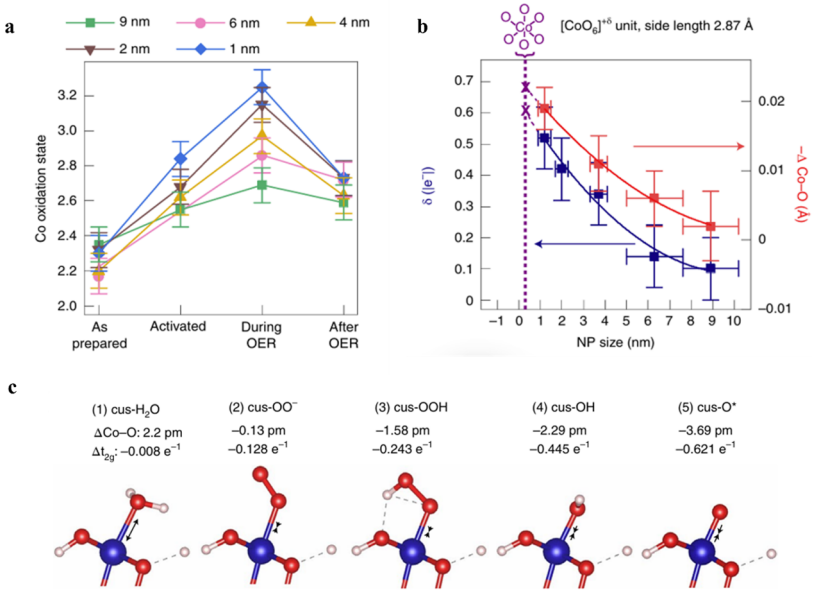


Figure 7. Size-dependent OER-active-state formation in $CoO_x(OH)_y$ nanoparticles. (**a**) Co oxidation-state evolution before, during and after OER. Adapted with permission from Ref. [77]. Copyright 2022, Springer Nature. (**b**) Size-

dependent oxidative charge accumulation and Co–O bond contraction. Adapted with permission from Ref. [77]. Copyright 2022, Springer Nature. (**c**) DFT-calculated CoOOH surface intermediates, supporting an oxyl-like active motif. Adapted with permission from Ref. [77]. Copyright 2022, Springer Nature.

2.2. Static ML as a Precursor-Accessibility Map

Static ML is useful in active-state formation only when its task is defined narrowly. After the four formation routes discussed above, static ML should not be treated as a model that directly observes oxyhydroxide growth, selective leaching, defect-gated reconstruction or spatially asynchronous surface–bulk evolution. Its more appropriate role is to provide precursor priors for these routes. It can estimate whether a precursor is chemically prepared to oxidize and hydrate, whether it contains components vulnerable to selective dissolution, whether it has local motifs that may gate reconstruction, and whether its geometry may support spatially connected active-state formation. It cannot observe the transition itself. The main error in many OER ML studies is the interpretation of static-descriptor outputs as evidence for the working catalyst. Static ML is best read as a precursor-accessibility map: it tells which route may be accessible, not which state actually carries current under potential [82–87].

For oxyhydroxide formation, thermodynamic and electronic descriptors provide the first static prior for judging whether a precursor surface can oxidize, hydrate and bind OER intermediates in a chemically favorable way. Adsorption energies of *OH, *O and *OOH, scaling-relation deviations, e.g., occupancy, metal-oxygen covalency, formation energy and surface stability have provided the first descriptor language for activity screening. Man et al. showed that adsorption-energy scaling can organize oxide OER activity and constrain the accessible overpotential window [88]. Hong et al. further evaluated oxide OER descriptors statistically, showing that chemically plausible descriptors do not contribute equally to activity prediction [89]. These studies turn large chemical spaces into interpretable maps. Their boundary is equally important: adsorption energy describes a site on an assumed structure. It does not say whether that site survives OER, converts into an oxyhydroxide layer or is replaced by an electrolyte-derived working state [90].

Geometric and symbolic descriptors add a structural prior to oxyhydroxide formation because they describe whether the precursor lattice and exposed coordination motifs are accessible to surface transformation. Weng et al. used symbolic regression to derive a compact perovskite descriptor, μ/t, from the octahedral factor μ and tolerance factor t (Figure 8a) [91]. This descriptor is useful because it converts perovskite geometry into a simple screening rule: the B-O octahedral environment and global lattice tolerance jointly influence whether a perovskite composition is structurally suitable for high OER activity. The value of symbolic regression is therefore not only prediction accuracy; it exposes which structural terms may prepare a lattice for surface transformation. However, the target remains a static activity relation. A favorable μ/t value may indicate that the precursor lattice is geometrically accessible to OER-active surface evolution, but it does not prove when reconstruction begins, how thick the transformed layer becomes or whether the reconstructed surface persists under bias.

Large calculated surface libraries extend this precursor prior from simple descriptors to explicit adsorbate, vacancy and surface configurations, but they still describe possible starting landscapes rather than observed state transitions. Back, Tran and Ulissi combined automated DFT calculations with ML to explore OER catalyst design space through computed adsorption energetics [92]. Such workflows are powerful because they enlarge the number of candidate surfaces, adsorbates and terminations that can be evaluated before experiment. The Open Catalyst 2022 dataset further strengthens this direction by providing graph-based oxide electrocatalyst structures, adsorbate configurations, vacancy defects, coverages and total-energy tasks at a scale suitable for learning local oxide environments (Figure 8b) [93]. These resources make static ML much more chemically expressive than simple composition models. Yet their prediction target is still a frozen or relaxed configuration. They do not encode induction time, converted surface fraction, active-layer thickness, reconstructed-layer persistence or potential-dependent connectivity. A static surface calculation can suggest that a site is reactive; it cannot determine whether that site is the one carrying current after reconstruction.

For selective leaching and redeposition, stability-oriented static ML provides a dissolution-risk prior rather than a direct description of the leaching pathway. Dissolution tendency, Pourbaix stability, decomposition energy, vacancy formation energy and site-level electrochemical stability define this descriptor family. Flores et al. used active learning to accelerate the discovery of stable Ir oxide polymorphs for OER [94], Bang et al. mapped electrochemical stability across realistic metallic nanoparticles [95], and Abed et al. developed a Pourbaix ML framework to screen acidic water-oxidation catalysts with suppressed Ru dissolution (Figure 8c,d) [96]. In the Pourbaix framework, a CGCNN-based surrogate model was trained on a large mixed-metal oxide space to predict electrochemical stability and identify Ru-based rutile oxides with lower decomposition risk than RuO_2. The experimentally selected $Ru_{0.6}Cr_{0.2}Ti_{0.2}O_2$ showed improved acidic OER durability, suppressed Ru dissolution and

reduced lattice-oxygen participation compared with RuO_2. This is a strong example of static ML used correctly: it identifies a stability-risk window and nominates compositions less likely to dissolve. But the limitation remains. Instability pressure is not the same as degradation pathway. The same dissolution tendency may lead to productive leaching, passivation, redeposition-assisted activation or irreversible corrosion. A Pourbaix boundary can warn that a component is vulnerable; it cannot decide whether the remaining surface becomes a better active shell.

For defect-gated and spatially heterogeneous reconstruction, local-environment descriptors provide the closest static bridge toward dynamic learning. Oxygen-vacancy formation energy, cation-vacancy tendency, coordination number, strain, neighbouring-cation identity and low-coordination motifs can describe where reconstruction is likely to begin. Wexler et al. showed that oxygen-vacancy formation in oxide perovskites is governed by coupled local chemistry rather than single-element identity [97]. Lunger et al. used atom-level ML to connect local structural motifs in metal oxide OER catalysts with OER-relevant behavior (Figure 8e) [98]. Their graph-based framework learns site-dependent descriptors such as O 2p-band center, metal d-band center, Bader charge, magnetic moment and local vibrational information from the atomic environment, then links these descriptors to OER intermediate binding. This is important because active-state formation is often triggered by specific sites rather than by the average bulk formula. The model can therefore identify labile oxygen sites, unusual coordination environments and neighbor effects that may serve as reconstruction starting points. However, it still describes the starting landscape. A labile site may initiate oxyhydroxide formation, dissolve away, become passivated or remain disconnected from current. Local structure is the right language for precursor priors, but it is not yet a trajectory.

The way forward is to keep static ML inside its evidentiary boundary. For oxyhydroxide formation, static models can provide oxidation, hydration and adsorption priors, but they cannot determine formation onset or active-layer growth. For selective leaching, they can identify dissolution-risk windows, but they cannot distinguish productive surface selection from destructive corrosion. For defect-gated reconstruction, they can locate labile motifs and vacancy-prone environments, but they cannot prove whether these defects generate a connected working state. For spatially asynchronous evolution, they can describe particle size, local coordination and structural heterogeneity, but they cannot identify which reconstructed domains carry current. These precursor priors become useful only when they are tested against transition evidence, including activation charge, first spectroscopic conversion, dissolution flux, active-layer growth rate, converted surface fraction, spatial connectivity and current retention after state formation. This boundary defines where static ML ends and dynamic trajectory learning begins.

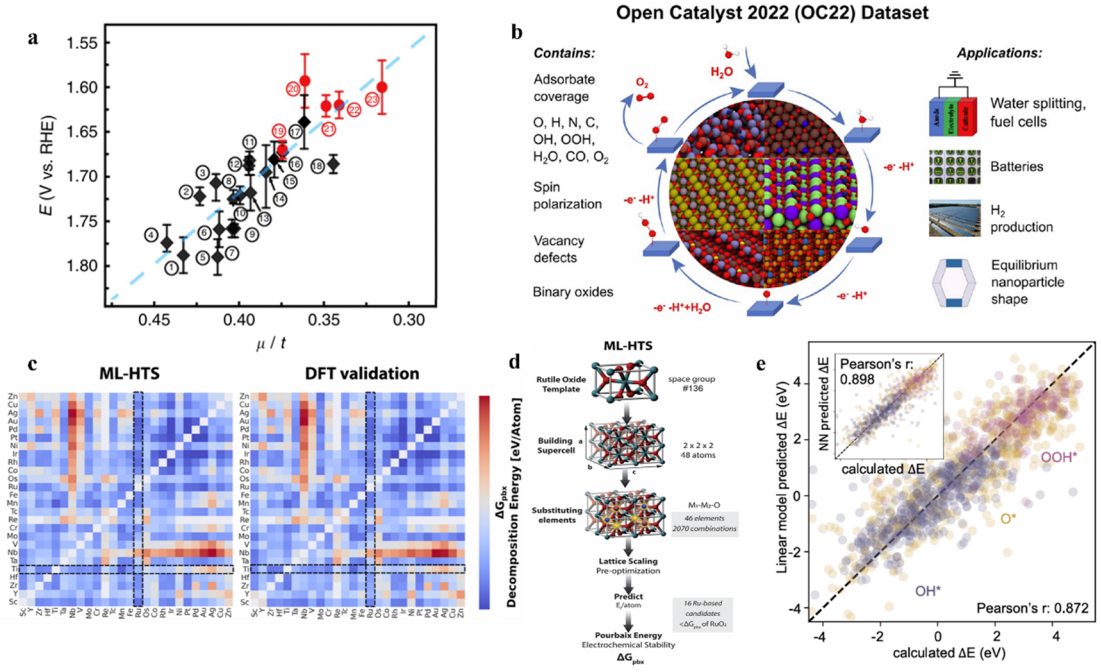


Figure 8. (**a**) Linear correlation plot between symbolic-regression-derived compact μ/t descriptor (octahedral factor μ divided by tolerance factor t) and experimental OER overpotential across perovskite oxide libraries. Adapted with permission from Ref. [91]. Copyright 2020, Springer Nature. (**b**) Overview workflow of the OC22 dataset, illustrating massive oxide electrocatalyst slab/adsorbate structures and unified energy/adsorption prediction benchmarks designed for graph neural networks and local-environment atomistic learning models. Adapted with permission from Ref. [93].

Copyright 2023, American Chemical Society. (**c**,**d**) Workflow of Ulissi's Pourbaix machine learning framework coupling graph neural network surrogate models and Pourbaix stability evaluation for screening acid-stable Ru-based OER catalysts with inhibited Ru dissolution. Side-by-side Pourbaix decomposition energy heatmaps from ML-HTS screening (**left**) and DFT validation (**right**), mapping the stability landscape of Ru-containing multi-metal oxides to identify dopants that mitigate Ru dissolution under acidic OER conditions. Adapted with permission from Ref. [96]. Copyright 2024, American Chemical Society. (**e**) Parity plot comparing linear atom-level ML predicted OER intermediate adsorption energies (ΔE) against DFT reference values for metal oxide catalysts, with inset neural network prediction performance; high Pearson correlation confirms local atomic structural motifs reliably encode oxygen evolution catalytic behavior. Adapted with permission from Ref. [98]. Copyright 2024, Springer Nature.

2.3. Dynamic ML for Formation Pathways: Progress and Limitations

A dynamic workflow is not necessarily dynamic learning. The distinction is whether the model only searches chemical space or predicts one of the state-transition paths by which a precursor becomes a working catalyst. Active learning, transfer learning, Bayesian optimization and automation can efficiently identify high-performing candidates, but they become trajectory learning only when each iteration records whether the selected material forms an oxyhydroxide layer, undergoes selective leaching or redeposition, enters defect-gated reconstruction, or develops a spatially connected working domain. The required labels are therefore not only activity scores, but activation onset, conversion rate, dissolution flux, reconstructed fraction, spatial connectivity and working-state persistence. Moon et al. used active learning to identify a four-metal perovskite oxide for OER [99]. Mints et al. compared experimental and theoretical models across high-entropy oxide composition space (Figure 9a) [100]. In their AuIrOsPdPtReRhRu nanoparticle library, the experimental machine-learned model identified AuIrOsPdRu as an optimal composition, while the DFT model attributed most intrinsic activity to Ru and Ir sites and a positive ligand effect from Pd. The mismatch was equally informative: the beneficial roles of Au and Os were not captured by the static DFT model and were instead assigned to structural effects such as support-like behavior or surface roughening. This case shows why composition optimization is not yet dynamic learning. The model can locate a high-performing region in composition space, but the hidden variable may be surface area change, selective restructuring, oxide formation, or stability during activation. Jiang et al. used transfer learning to discover efficient perovskite oxides for alkaline water oxidation [101]. These workflows answer where to look next. They do not automatically answer what the selected material becomes during OER. Each iteration would need the state evidence behind the score: activation charge, time to stable current, spectroscopic conversion, dissolution flux and whether final activity comes from a self-limited shell or continued material loss. The champion composition is then not only a point in composition space, but also a formation path with a cost: oxidation and hydration cost for oxyhydroxide growth, dissolution cost for surface selection, reconstruction cost for defect-gated activation, or connectivity cost for spatially heterogeneous working-state formation.

Activity-stability optimization is most closely connected to selective leaching, redeposition and self-terminated reconstruction, but it still does not automatically make the model mechanistic. Jenewein et al. used multiobjective Bayesian optimization to balance activity and stability in non-noble acidic OER catalysts (Figure 9b) [102], while Zhang et al. showed that NiFe-based electrocatalysts can maintain OER activity through self-repair driven by dynamic Fe exchange between the catalyst and electrolyte [103]. During alkaline OER, Fe species leach from NiFe-based catalysts, while at a moderate dissolved Fe concentration, part of the Fe can be readsorbed onto the reconstructed NiFe oxyhydroxide surface, establishing a dynamic balance between Fe loss and repair. *In Situ* Raman spectroscopy further showed that Fe incorporation suppresses excessive Ni oxidation and that surface-adsorbed Fe species can be strongly retained on the formed NiOOH layer, thereby stabilizing catalytic activity. This case explains why activity and stability cannot be judged only from endpoint current retention. A catalyst may look stable because the initial solid is preserved, because a reconstructed shell self-terminates, or because active species continuously dissolve and redeposit while the current remains steady. These cases can occupy similar positions in an activity-stability plot, but they imply different design rules. The missing labels are not more refined endpoint scores. They are the trajectory variables that distinguish productive surface selection from corrosion: leaching onset, dissolution flux, redeposition rate, electrolyte-derived active-site replenishment, self-termination depth, converted fraction and irreversible metal loss.

Automation can provide the experimental volume needed to learn oxyhydroxide growth and defect-gated reconstruction, but only if the experiment is designed around state variables rather than endpoint activity alone. Xu et al., Kodera and Sayama, and Tabor et al. showed how high-throughput synthesis, robotic testing and smart automation can vary composition, protocol and synthesis route at scale (Figure 9c) [104–106]. Xu et al., for example, combined high-throughput aerogel synthesis with AI modeling to predict OER performance in

multielement non-noble catalysts. Their workflow used systematic experimental data, 909 inorganic-material descriptors and a hierarchical neural-network strategy to predict Tafel slopes and onset overpotentials, with experimental validation improving predictive accuracy. This type of platform is valuable because active-state formation depends on variables that are difficult to explore one at a time by hand, including defect density, activation duration, electrolyte history and support contact. The risk is that automated datasets may multiply hidden differences while still reporting only overpotential, Tafel slope or current. In that case, the model learns synthesis fingerprints rather than reconstruction rules. A more useful dynamic workflow would deliberately hold some variables fixed and perturb one state-forming factor at a time, then record oxyhydroxide conversion onset, growth rate, active-layer fraction, defect-triggered activation probability and post-formation stability.

Spatial reconstruction corresponds to the fourth formation problem: the working state may be controlled by a connected minority domain rather than by the electrode-average phase. Haase et al. showed that nanoscale inhomogeneities in Co_2FeO_4 shape OER behavior (Figure 9d) [107]. Two nominally identical Co_2FeO_4 spinels showed very different activities because the more active sample contained sub-10 nm Co-rich amorphous minority domains linking the crystalline spinel host. These Co^{2+}/hydroxide-rich regions were oxidized during OER into Co^{3+}-rich $CoO_x(OH)_y$-like domains and supplied more redox-active Co sites, whereas the average Co:Fe ratio remained close to the nominal value. This means that the active label of the electrode may be governed by a minority local phase rather than by the bulk-average composition. Ding et al. used data mining, active learning and domain adaptation to address dataset mismatch in OER discovery [108]. These studies point to a weakly supervised learning problem. Domains, particles or image regions are local instances, while electrode current is only a global label. The model must infer which local converted regions actually carry current and which are spectators or failure precursors. This requires labels such as converted fraction, local connectivity, domain persistence, particle-to-particle variance, current contribution from minority domains and local failure probability.

The unresolved gap is therefore output definition. Candidate-search models become chemically dynamic only when the optimization target is aligned with the active-state formation routes. For oxyhydroxide formation, the output should include activation charge, first spectroscopic conversion, active-layer growth rate and saturation. For selective leaching and redeposition, it should include dissolution flux, foreign-ion uptake, redeposition rate and self-termination depth. For defect-gated reconstruction, it should include defect class, reconstruction onset, conversion cost and defect fate after OER. For spatially asynchronous evolution, it should include converted fraction, local connectivity, domain persistence and current contribution from the connected working-state region. Without these outputs, dynamic workflows remain efficient candidate-search tools rather than models of active-state formation.

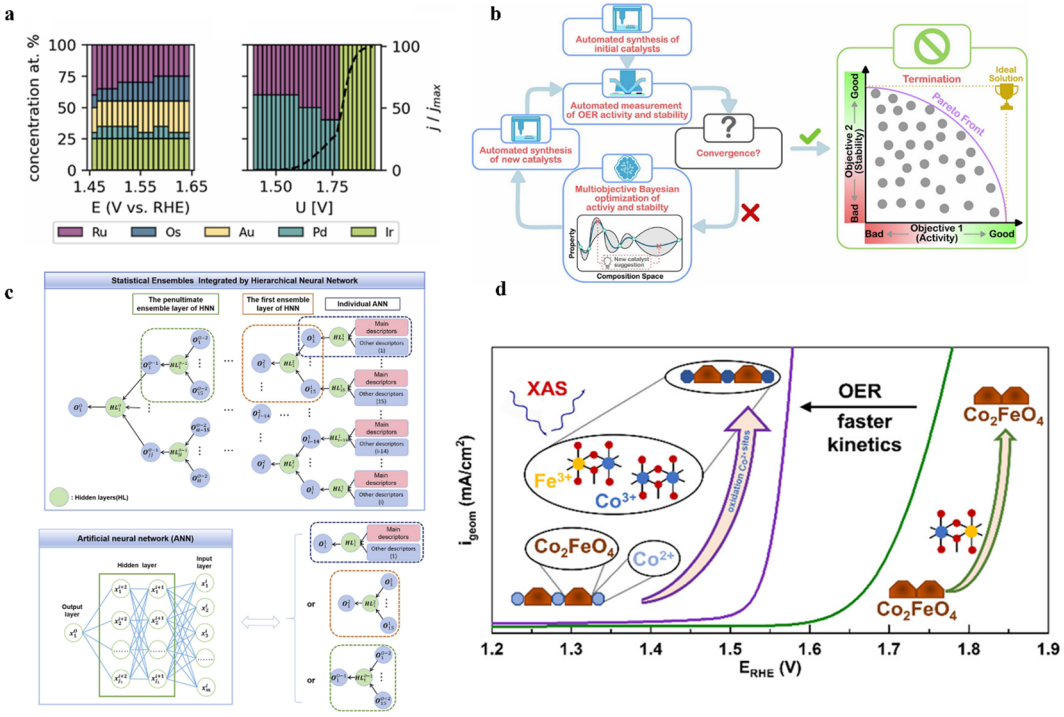


Figure 9. (**a**) Side-by-side comparison of experimental and DFT-predicted compositional distributions of Ru-Os-Au-Pd-Ir high-entropy catalysts as a function of applied potential, mapping composition-activity trends across the full multi-metal composition space. Adapted with permission from Ref. [100]. Copyright 2024, American Chemical

Society. (**b**) Schematic workflow of multiobjective Bayesian optimization (MOBO) coupled with high-throughput electrochemistry for simultaneous optimization of activity and stability of non-noble Co–Mn–Sb–Sn–Ti acidic OER catalysts. Adapted with permission from Ref. [102]. Copyright 2024, Royal Society of Chemistry. (**c**) Schematic architecture of the Hierarchical Neural Network (HNN) ensemble AI model developed by Xu's group, which processes high-throughput experimental datasets to predict Tafel slopes and onset overpotentials of multi-element OER electrocatalysts. Adapted with permission from Ref. [104]. Copyright 2024, Springer Nature. (**d**) Comparative OER polarization curves and corresponding nanoscale structural schematic diagrams for two Co_2FeO_4 spinel catalysts with distinct local Co/Fe compositional inhomogeneities, illustrating how nanoscale chemical heterogeneity dictates oxygen evolution reaction kinetics. Adapted with permission from Ref. [107]. Copyright 2022, American Chemical Society.

2.4. Toward Learnable Active-State Transition Records

The four active-state phenomena defined in Section 2.1 are converted here into learnable event records: oxyhydroxide formation, material exchange, defect- or proton-gated reconstruction, and spatially asynchronous conversion. Charge partition is added as a chemistry constraint because a reconstructed surface is meaningful only when stored redox charge can be separated from catalytic O_2 evolution. Each sample starts from the precursor state x_0, follows the potential-electrolyte protocol $u(t)$, stores only observations available before a fixed horizon $m(t \leq \tau)$, and predicts the later working-state response $y(t > \tau)$. This design keeps the learning problem close to the chemistry described above: the model should learn which precursor features open a productive active-state route, which route drains material, and which local domains actually carry current.

Task 1 is oxyhydroxide active-layer learning. The model must identify when the working layer first appears, how much of it becomes electrochemically addressable and whether the converted layer remains active after the initial current rise. Qian et al. provide a useful benchmark by quantifying active Fe-site density, Fe-site turnover frequency and stability of NiFe (oxy)hydroxides *in situ* (Figure 10a) [109]. The important point is the separation of three quantities that endpoint overpotential merges. A catalyst can improve because more Fe sites become accessible, because each accessible Fe site turns over faster, or because the Fe population survives the anodic protocol instead of being exchanged or lost. The input record should therefore include precursor composition, Fe source, activation history, redox charge, electrolyte exposure and early current response. The outputs are formation onset, active-site population, site-specific TOF, active-layer fraction, Fe uptake or loss rate and persistence of the operating interface. These labels test the first rule: activity follows the generated coordination environment, not the nominal precursor formula.

Task 2 is defect- or proton-gated temporal-state learning. Active-state formation can be gated by redox, deprotonation, hydration, defect evolution and partial material loss, but these signals do not appear in the same channel or at the same time. Diklić et al. show why this matters through operando XAS pitfalls for OER electrocatalysts (Figure 10b) [110]. In IrO_2 electrodes, a decrease in white-line intensity at high potential can look like a chemical reduction event unless the simultaneous loss of absorbing material is included in the interpretation. Wu et al. give the complementary positive case by resolving deprotonation-induced reconstruction in NiFe-based (oxy)hydroxides with time-resolved spectroscopy [111]. Together, the two studies make the same methodological demand: a transition label must contain the order and lag between proton removal, local coordination change, signal attenuation and current response. The inputs are synchronized current, XAS or Raman features, dissolution evidence, loading, film thickness, gas-removal condition and measurement window. The outputs are latent state path, induction time, channel-to-channel lag, artefact probability and uncertainty in assigning a spectral change to catalyst chemistry. This task prevents the model from confusing a true defect- or proton-gated transition with a measurement artefact or simple loss of material.

Task 3 is material-exchange and spatial-responsibility learning, connecting selective leaching/redeposition with spatially asynchronous conversion. Selective leaching, redeposition and electrolyte-derived incorporation should be treated as directed material flows, whereas spatial responsibility identifies which local domains participate in the useful trajectory. Yang et al. visualized Fe incorporation into NiO octahedra during OER with spatial and chemical resolution (Figure 10c) [112]. Starting from defined NiO octahedra, Fe^{3+} from the electrolyte enters the near-surface Ni-O framework under anodic operation and can form NiFe-LDH-like regions associated with improved OER onset. Further operation can also generate FeO_x-rich aggregates that no longer play the same productive role and may accompany activity loss. This case verifies the second and fourth phenomena in Section 2.1 at once: external matter can build the working state, and only part of the particle may enter the useful trajectory. The inputs are image regions, local Fe intensity, local Ni-O environment, potential history, electrolyte Fe reservoir and global current. The outputs are local state class, Fe-incorporation rate, NiFe-LDH-like converted fraction,

FeO_x spectator or failure probability, responsibility weight $w_i(t)$, connectivity c_i and local failure probability. A model that sees only final Fe content would miss the difference between productive incorporation, spectator deposition and spatially isolated reconstruction.

Task 4 is charge-partition learning as a chemistry constraint. This task does not define another formation route; it tests whether the reconstructed or exchanged surface is truly a working interface. Görlin et al. combined operando DEMS and XAS to measure OER dynamics, Faradaic charge efficiency and active metal redox states in NiFe oxide catalysts (Figure 10d) [113]. Their result makes a sharp distinction that current alone cannot make. Anodic charge can oxidize Ni, fill redox reservoirs in the catalyst or produce molecular O_2, and these processes do not have identical time constants. In Fe-rich NiFe oxides, O_2 Faradaic efficiency increases strongly while Fe remains largely Fe^{3+} and Ni does not simply accumulate as a static high-valence pool. The inputs are current, O_2 signal, redox-state trajectory, charge passed, activation protocol and electrolyte condition. The outputs are q_{redox}/q_{OER}, Faradaic efficiency, metal oxidation window, active-layer saturation and the transition point at which stored charge becomes catalytic turnover. Charge balance, mass conservation and Faradaic consistency should be built into the evaluation, because otherwise a model can mistake redox capacitance for active-state formation.

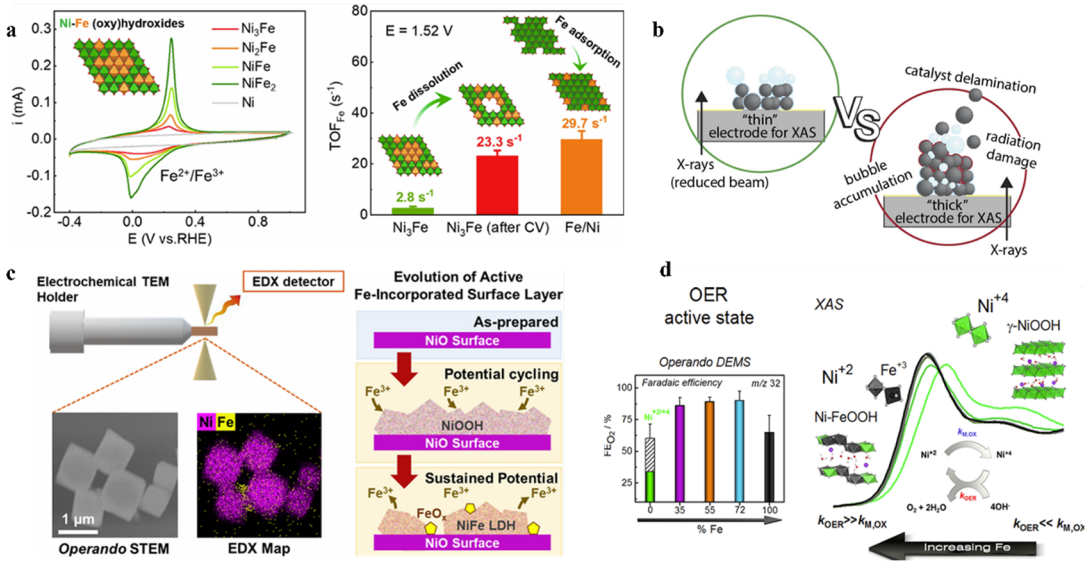


Figure 10. (**a**) *In Situ* electrochemical quantification of active Fe site density and Fe turnover frequency, tracking dynamic Fe leaching/redeposition to evaluate the operational stability of NiFe (oxy)hydroxide OER catalysts. Adapted with permission from Ref. [109]. Copyright 2022, American Chemical Society. (**b**) Schematic comparison of thin low-flux and thick catalyst electrodes for operando XAS OER measurement, visualizing radiation damage, bubble accumulation and catalyst delamination artefacts that distort the apparent active state of electrocatalysts. Adapted with permission from Ref. [110]. Copyright 2022, American Chemical Society. (**c**) Operando electrochemical STEM-EDX setup, elemental mapping and schematic evolution pathway visualizing graded Fe incorporation into NiO octahedra during OER. Spatially resolved Fe signals deliver detailed chemical distribution information far beyond binary Fe presence/absence labels. Adapted with permission from Ref. [112]. Copyright 2023, American Chemical Society. (**d**) Combined operando DEMS and XAS characterization of NiFe oxyhydroxides, quantifying OER faradaic efficiency, competing metal redox/OER kinetics, and potential-dependent Ni oxidation states highlighting the need for multimodal measurement constraints. Adapted with permission from Ref. [113]. Copyright 2016, American Chemical Society.

These tasks define a Section 2 solution that is specific to active-state formation. Oxyhydroxide formation is learned as an onset-and-population problem, leaching and redeposition as directed material-flow problems, defect- or proton-gated reconstruction as a temporally ordered hidden-state problem, and surface–bulk asynchrony as a spatial-responsibility problem. Charge partition then provides the chemistry constraint that separates catalytic turnover from redox storage or parasitic change. The cases are therefore not illustrations placed after a method. They specify what has to be labelled before dynamic ML can distinguish productive activation from corrosion, spectator deposition, disconnected reconstruction, redox storage or parasitic charge consumption. For implementation, each formation study should first define the state-transition event to be predicted before selecting the model. The sample unit is an electrode, particle ensemble or image-defined domain under one defined protocol, and the prediction horizon is fixed before baseline correction, denoising, scaling, peak fitting and descriptor

generation. Observation masks are kept because current, spectra, dissolution, gas evolution and microscopy are rarely collected at every time point; an unmeasured channel is marked as unobserved rather than imputed as experimental evidence. The model family is chosen according to the phenomenon being tested. Local-environment encoders such as NequIP can represent coordination and defect motifs, sequence or state-space models can follow dense current and spectral traces, and continuous-time models can handle irregular XAS, Raman and ICP-MS streams [114]. These models are therefore used to estimate the active-state event made observable by the experiment, rather than to repeat endpoint activity regression.

Validation closes the record by testing transfer at the level of the transition, not at the level of neighboring time points. Early-to-late tests ask whether the first activation window predicts later oxyhydroxide growth, Fe uptake, material loss or active-layer saturation; out-of-protocol and out-of-family tests change waveform, electrolyte, impurity level, activation duration or precursor family. Intervention tests change one causal handle, such as defect density, support contact, activation potential or electrolyte-derived metal availability, and ask whether the measured event sequence shifts in the predicted direction. Active learning is most useful when it selects experiments that separate active-state routes rather than electrodes expected only to maximize current [115,116]. Leakage control follows the same principle: the split unit should be electrode, synthesis batch, catalyst family, electrolyte reservoir or protocol, while final active-layer thickness, post-OER composition, late-time spectra and post-test microscopy are forbidden for early prediction [117–121]. With these controls, the next problem is how that interface distributes current among reaction paths and what stability cost follows from each path.

A dynamic label is reproducible only when its extraction rule is declared together with the raw evidence and its uncertainty. We therefore distinguish directly observed labels (for example calibrated dissolution flux), derived labels (for example growth rate calculated from an experimentally estimated active fraction), and latent labels (for example mechanism weights inferred from multiple indirect channels). Table 1 gives minimum operational definitions for the labels used throughout this Review. Thresholds, change-point rules, spectral components and calibration curves should be fixed without access to the held-out test trajectories, and uncertainty from calibration or fitting should be propagated to the final label rather than discarded.

For latent labels, activity alone is not accepted as ground truth. For example, an increase in current cannot by itself raise a LOM weight because the same rate change may arise from active-site density, adsorption energetics, solvation or transport. A defensible latent label therefore retains the evidence channels that constrain it and an explicit residual or out-of-library term when the candidate state or mechanism set is incomplete.

Table 1. Operational extraction of representative dynamic OER learning labels from raw evidence.

Dynamic Label	Primary Raw Evidence	Quantitative Extraction Rule	Reported Quantity	Uncertainty/Quality Check
Formation onset	XAS, Raman, current/redox transient	Predefined change point or threshold above baseline/noise	t_{onset} (s, min, or potential)	Bootstrap/change-point interval; sensitivity to threshold
Active fraction and growth	Spectral component intensity, spatial maps	Calibrated component fraction $f_{active}(t)$; growth = df_{active}/dt	fraction (0–1); time^{-1}	Spectral-fit confidence; spatial sampling variance
Dissolution flux	Online ICP-MS + electrolyte flow	Calibrated concentration × flow rate, aligned to electrochemical time	mol s^{-1} or mass s^{-1}	Calibration error; transport lag; blank correction
Pathway weights/switching	Isotope DEMS, ATR-FTIR/Raman/XAS, dissolution evidence	Constrained multimodal mixture inference with weights summing to unity; switch at predefined crossing/threshold	$w_{AEM}(t)$, $w_{LOM}(t)$, $w_{OPM}(t)$; t_{switch}	Posterior/fit interval; residual out-of-library weight
Failure onset/useful lifetime	ICP-MS, voltage drift, structure, microscopy	First predefined failure event; censored if the event is not observed	t_failure, cycles, remaining useful life	Event-definition sensitivity; censoring status
Transfer trajectory score	Predicted and observed trajectories under held-out condition/device	Normalized trajectory error/similarity over a fixed horizon	dimensionless score plus component errors	Confidence interval across independent runs/devices

3. Mechanism–Degradation Coupling in Evolving OER Interfaces

Once the working interface has become accessible, the next question is not only how fast it produces O_2. The harder question is how the current is distributed among elementary routes, which intermediate populations accumulate, and what stability cost each route imposes. A catalyst may increase rate by creating more oxidized sites, by changing adsorbate residence time, by allowing lattice oxygen to participate, or by opening an oxygen-oxygen coupling route that was inaccessible in the precursor. The same change can also raise vacancy

accumulation, dissolution, passivation or poisoning risk. This section separates mechanism-stability coupling into four connected variables: intermediate coverage trajectory, pathway weight redistribution, lattice-oxygen safety window and degradation-path probability. Static descriptors can locate plausible mechanism tendencies; dynamic ML needs to learn how those tendencies become weighted, costly trajectories under bias (Figure 11).

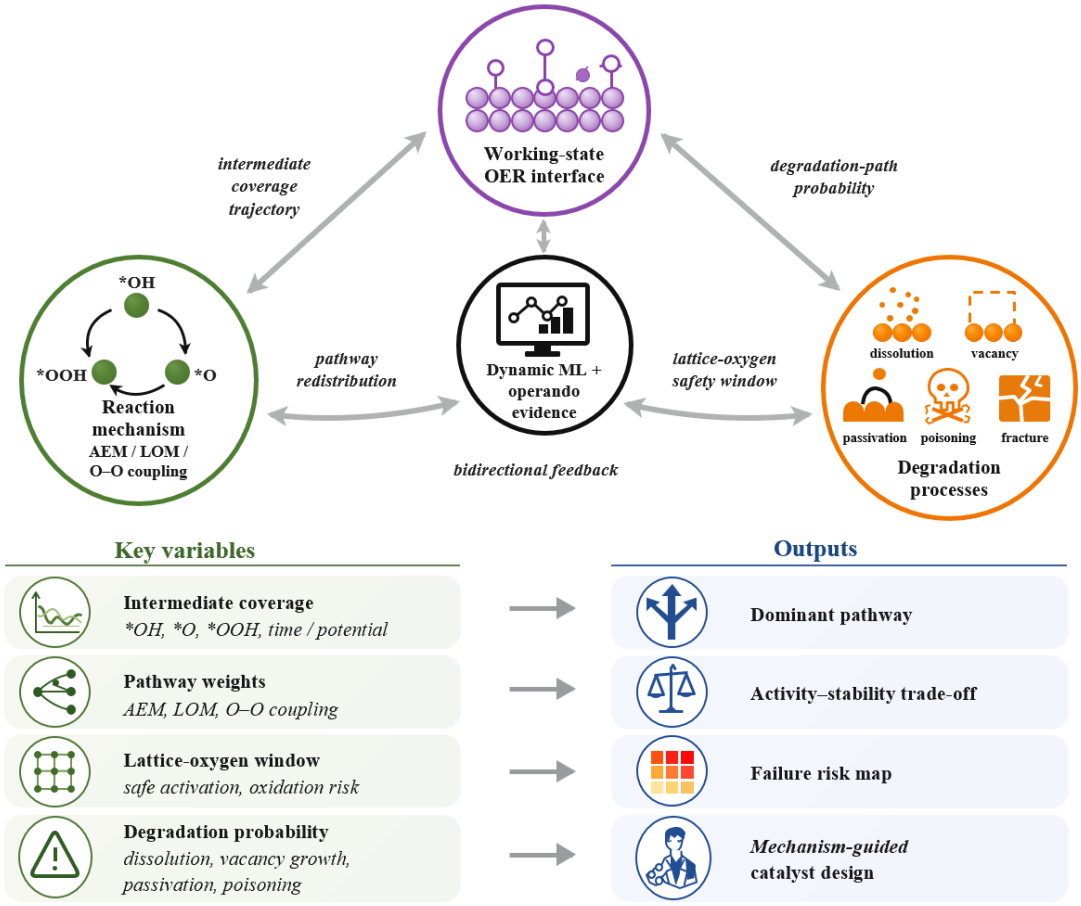


Figure 11. Mechanism–degradation coupling in evolving OER interfaces. OER performance is governed by the coupled evolution of intermediate coverage, pathway weights, lattice-oxygen participation, and degradation probability. Increasing bias can redistribute contributions from AEM, LOM, and O–O coupling, while excessive lattice-oxygen activity may promote vacancy formation, dissolution, passivation, poisoning, and mechanical failure. Dynamic ML therefore aims to learn coupled mechanism–degradation trajectories rather than endpoint activity alone.

3.1. Pathway Redistribution Controls Both Activity and Failure

Mechanism–degradation coupling should be learned as a trajectory of intermediate population, pathway redistribution and failure-node activation rather than as a fixed mechanism label or an endpoint stability value. Intermediate coverage is a dynamic state variable that controls both rate and instability [122]. Adsorption energy describes a possible binding strength on an assumed structure, whereas the operating surface decides how many *OH, *O, *OOH or M=O-like states are populated, how long they persist and whether they turn over or accumulate. Liang et al. quantified redox-active centers and binding strength in iridium oxides with operando time-resolved optical spectroscopy (Figure 12a) [123]. Their key result is that higher geometric activity in amorphous IrO_x does not simply mean that each Ir site is intrinsically more active. Amorphous IrO_x contains a larger population of potential-accessible redox-active states, aided by deeper proton penetration and a more flexible short-range structure, whereas rutile IrO_2 contains fewer accessible redox centers under the same potential window. When the current is normalized to the density of active states, the intrinsic turnover rates of IrO_x and IrO_2 become much closer. More importantly, the accumulated *O-like states interact repulsively: as *O coverage increases, O binding weakens, which promotes the subsequent O–O bond-forming step. Thus, activity is controlled by two coupled variables rather than one descriptor: active-state population and coverage-dependent binding strength. The ML target is therefore not only ΔGO or current density, but the time-dependent population of oxidized states, their interaction strength and the coverage level at which accumulation turns into turnover.

Jia et al. reached the same issue from an electrolyte-dependent direction in CoOOH catalysts (Figure 12b) [124]. Operando XRD and HRTEM showed that electrolyte cations can intercalate into the CoOOH layers during OER, with larger cations producing greater interlayer expansion and higher catalytic activity in the order $Cs^+ > K^+ > Na^+ > Li^+$. XAS, *in situ* Raman, UV–vis spectroscopy, electrochemistry and theoretical calculations further showed that cation intercalation modifies the Co–O coordination environment, shifts the Co electronic structure, optimizes oxygen-intermediate adsorption and facilitates the formation of OER-active Co(IV) species. This case shows that the population of high-valent active states is not determined solely by the precursor structure, but can be dynamically selected by the electrolyte environment. For dynamic ML, the relevant outputs should therefore include cation identity, interlayer spacing, Co–O bond length, Co oxidation-state trajectory, Co(IV) fraction and oxygen-intermediate coverage. Together, the IrO_x and cobalt hydroxide cases show that intermediate coverage should be learned as a time-dependent population variable rather than inferred from adsorption energy alone. The outputs should include redox-active site density, high-valent-state fraction, *O/M=O-like coverage, residence time, active-state persistence and coverage-dependent Tafel response [125,126].

AEM, LOM and oxide-path mechanism (OPM) are better treated as pathway weights than fixed names attached to a catalyst [127]. Co–Zn oxyhydroxides demonstrate that these weights are selected by both oxygen-hole energetics and local atomic configuration. Huang et al. showed that redox-inactive Zn^{2+} does not act as a conventional catalytic center; instead, its filled $3d^{10}$ configuration weakens Zn–O orbital overlap and introduces high-energy oxygen non-bonding states near the Fermi level (Figure 12c) [73]. Electron removal from these states generates oxygen holes while preserving Co–O bond order, but oxygen oxidation alone is insufficient to establish a productive LOM. Direct O–O coupling becomes favorable only when two neighboring oxidized oxygens can rotate and hybridize their holes without substantially disrupting directional Co–O covalency. This requirement makes the pathway strongly dependent on the Zn content and the resulting local connectivity. CoOOH and $Zn_{0.1}Co_{0.9}OOH$ remain AEM-dominated, whereas the Zn–O–Co–O–Zn configuration in $Zn_{0.2}Co_{0.8}OOH$ stabilizes the lattice-coupled intermediate, lowers its formation barrier and switches the preferred route toward LOM. Importantly, further increasing Zn does not continuously improve the pathway: in $Zn_{0.5}Co_{0.5}OOH$, facile lattice-oxygen release is followed by energetically difficult vacancy refilling, promoting oxygen loss, reconstruction and activity decay. $Zn_{0.2}Co_{0.8}OOH$ therefore occupies a mechanistic window in which direct O–O coupling is accessible while oxygen vacancies remain refillable. The proposed switch was supported experimentally by the appearance of peroxo-like oxygen species, inhibition of activity by a tetramethylammonium probe, a kinetic isotope response and pronounced pH dependence, linking the calculated local configuration to an operating-state pathway rather than to a static compositional label [128]. Wang et al.'s grand-canonical microkinetic network then provides the general rule: AEM, intramolecular oxygen coupling and LOM-type routes can exchange dominance as potential, coverage and surface state change [129]. The label should therefore be a set of potential-dependent pathway weights, not a single mechanism name: local oxygen-hole configuration, asymmetric M–O–M connectivity, switching potential, hysteresis and uncertainty in $w_{AEM}(t)$, $w_{LOM}(t)$ and $w_{OPM}(t)$ [130].

Mechanism weights also need a conservation test. If a model assigns a larger LOM weight, the claim has to close with isotope-resolved O_2, Faradaic efficiency, charge passed and the amount of oxygen or metal lost from the lattice. If the inferred pathway creates more oxygen vacancies than can be healed under the measured current, the label is chemically inconsistent. This mass-and-charge closure is how trajectory learning separates a real mechanism switch from spectral drift, transport artefacts or overfitted activity trends.

Lattice oxygen activation is valuable only inside a safety window where oxygen participation improves OER before vacancy accumulation and metal dissolution dominate [131]. Mo-doped NiFe (oxy)hydroxide illustrates the benefit side of this window [132]. He et al. used a sacrificial-template route in which MoS_2 helps form ultrathin NiFe (oxy)hydroxide and leaves trace Mo after leaching (Figure 12d) [133]. The resulting MoNiFe (oxy)hydroxide shows much higher mass activity than the undoped NiFe analogue. Spectroscopy and DFT link this enhancement to an upshifted O 2p band, weakened metal–oxygen bonding and easier oxygen-vacancy formation. This is not merely a "more defective is better" case. Mo tunes the oxygen activity so that lattice oxygen can participate more readily in the OER pathway. However, the same electronic change also lowers the barrier to oxygen removal, so the useful descriptor is not LOM accessibility alone, but the balance between oxygen activation, vacancy formation and structural retention [134].

Kasian et al. defined the cost side in Ir oxides by combining isotope labelling, atom probe tomography, online ICP-MS and electrochemistry to connect lattice-oxygen participation in hydrous Ir oxide with faster Ir dissolution than in rutile IrO_2 [135]. Xu et al. further reported lattice-water-assisted oxygen exchange in hydrous $IrO_x \cdot nH_2O$ [136]. Hydrous IrO_x exchanges oxygen with the electrolyte more deeply than rutile IrO_2, whereas oxygen exchange in rutile IrO_2 is much more surface-confined. This higher oxygen mobility helps explain the high activity of hydrous IrO_x, but it also correlates with faster Ir dissolution and lower durability. The same structural openness that allows more

lattice oxygen participation therefore increases the probability that oxygen loss and metal loss become coupled. Qu et al. added a protocol dimension by using operando differential electrochemical mass spectrometry to show temperature-dependent mechanism evolution on $RhRu_3O_x$, where hotter acidic OER makes lattice oxygen more accessible and shifts the durability regime (Figure 12e) [137]. At room temperature, $RhRu_3O_x$ follows a relatively stable AEM-dominated route and can operate for over 1000 h in a PEM water electrolyzer at 200 mA cm^{-2}. At elevated temperature, operando isotope DEMS reveals the emergence of a LOM contribution, accompanied by reduced stability. Thus, the mechanism is not an intrinsic identity of $RhRu_3O_x$; it is selected by temperature. The label cannot be LOM-positive or LOM-negative; it should be defined as the operating range where oxygen participation, vacancy healing, metal retention and protocol conditions remain compatible [138].

Degradation is therefore a competing pathway triggered by specific mechanism states rather than a stability value measured after the test. Endpoint current retention hides whether the material first dissolved, passivated, changed phase, accumulated spectator oxygen species or suffered impurity poisoning. Two electrodes can end with the same retained current while requiring opposite remedies: stronger metal–oxygen bonding, less aggressive oxygen redox, a different potential waveform, cleaner electrolyte or improved mass transport. The first degradation node is therefore more informative than the final retention value because it identifies which mechanistic state opened the failure route [139]. Dynamic ML should therefore predict the probability of dissolution, phase change, passivation, poisoning, repair or mixed loss from the pre-failure mechanism trajectory, together with remaining useful lifetime and uncertainty. This keeps the stability label attached to the mechanism that produced it, rather than treating stability as an endpoint number detached from pathway history.

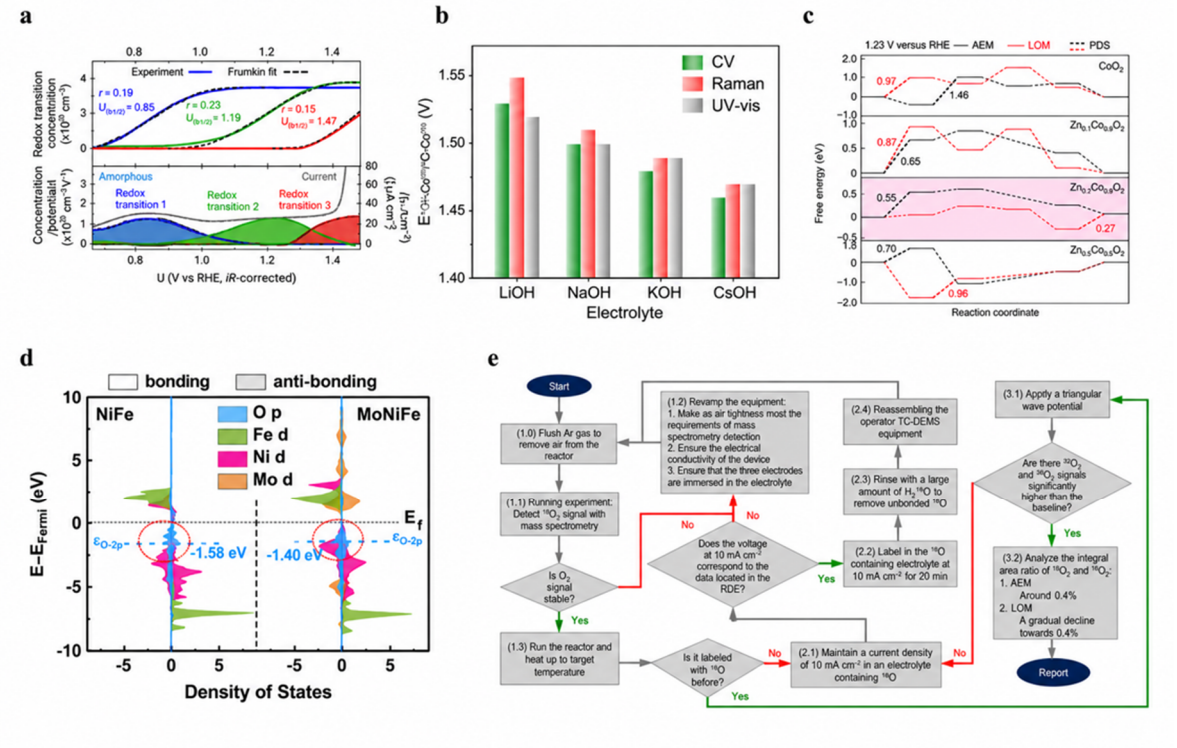


Figure 12. (**a**) Redox-active centers and binding energetics on amorphous IrO_x quantified by operando time-resolved optical spectroscopy. **Top**: areal density of redox transitions (solid: experiment; dashed: Frumkin isotherm fits). **Bottom**: redox transition waves overlaid with voltammetric current. Adapted with permission from Ref. [123]. Copyright 2024, Springer Nature. (**b**) Electrolyte-cation-dependent formation potentials of OER-active O–Co(IV) species in CoOOH, integrating CV, *in situ* Raman, and *in situ* UV–vis results in LiOH, NaOH, KOH, and CsOH electrolytes. Adapted with permission from Ref. [124]. Copyright 2023, Wiley-VCH GmbH. (**c**) Local-configuration-dependent competition between AEM and LOM in Zn-substituted CoOOH. Calculated free-energy profiles show that CoO_2 and $Zn_{0.1}Co_{0.9}O_2$ favor AEM, whereas the Zn–O–Co–O–Zn configuration in $Zn_{0.2}Co_{0.8}O_2$ stabilizes the lattice-oxygen pathway. Excessive Zn substitution makes oxygen-vacancy refilling energetically limiting. Adapted with permission from Ref. [73]. Copyright 2019, Springer Nature. (**d**) Projected density of states of NiFe and MoNiFe (oxy)hydroxides, showing upshifted O 2p band and weakened metal-oxygen bonding induced by Mo doping. Adapted with permission from Ref. [133]. Copyright 2022, Springer Nature. (**e**) Operando TC-DEMS experimental protocol for temperature-dependent OER mechanism identification, distinguishing AEM and LOM pathways via the $^{34}O_2/^{32}O_2$ ratio evolution. Adapted with permission from Ref. [137]. Copyright 2025, Springer Nature.

3.2. Static ML as a Mechanistic Plausibility Prior

After Section 3.1 defines mechanism–degradation coupling as a trajectory of intermediate population, pathway redistribution, charge/mass closure and failure-node activation, static ML should be positioned as a mechanism prior. It can identify compositions, sites and lattices that make AEM-like adsorption, lattice-oxygen participation, oxide-path behavior or degradation resistance plausible before the experiment, but it cannot assign the route taken by the working catalyst during OER. This distinction matters because static descriptors are often given more mechanistic authority than their evidence supports. A calculated adsorption energy, vacancy formation energy or Pourbaix stability score is valuable when it is read as a prior that guides operando testing. It becomes misleading when it is treated as a measured pathway [140].

Adsorption-energy and activity-stability maps provide the most established AEM prior. Liang et al. constructed activity-stability maps for $SrBO_3$ perovskite oxides across 3d, 4d and 5d transition metals, making the trade-off between favorable OER energetics and stability risk visible before exhaustive testing (Figure 13a) [141]. Their $SrTi_xRu_yIr_zO_3$ library is useful because it does not rank activity alone. Initial activity, short-term stability, extended stability and steady-state activity are mapped separately across the Ti–Ru–Ir composition triangle, so the model-like map already distinguishes an active but unstable region from a practically useful region. The deeper descriptor is the hybridization between mixed 3d/4d/5d metal states and O 2p orbitals. Increasing hybridization improves initial OER activity, but once it passes a threshold, stability retention drops and lattice oxygen becomes involved in the catalytic cycle. This is precisely why the map should be read as a mechanistic prior rather than a mechanism label. It identifies a composition window where AEM-like energetics, lattice-oxygen activation risk and acidic stability are balanced, but it does not prove which oxygen source or pathway dominates during operation. Such maps are powerful triage tools because *OH, *O and *OOH adsorption energies and scaling-relation deviations organize large composition spaces [142]. Their boundary is mechanism assignment. A map does not say whether the operating surface later follows AEM, shifts into LOM, opens an oxide-path route or mixes several routes.

Kim et al. used an equivariant transformer-based interatomic potential to screen thousands of single-atom-incorporated metal oxyhydroxide configurations and nominated W_1-NiFeOOH for noble-metal-free water electrolysis (Figure 13b) [143]. This case is a useful example of static ML used with the right evidentiary boundary. The pretrained EquiformerV2 model rapidly evaluated adsorption energetics across 3976 single-atom-incorporated metal oxyhydroxide configurations and more than 15,000 adsorbate structures, allowing W_1-NiFeOOH to emerge as a promising candidate from an otherwise inaccessible configurational space. However, the mechanistic claim was not made from the volcano plot alone. It became credible only after cyclic electrodeposition, atomic-scale characterization, *in situ* spectroscopy and DFT showed that subsurface W does not simply behave as an isolated active site. Instead, W redistributes charge around neighboring Ni–O–Fe edge motifs, lowers the proton-coupled deprotonation barrier and facilitates transformation toward the active γ-phase. Static ML therefore located a chemically plausible motif; dynamic and operando evidence supplied the operating mechanism by resolving charge redistribution, phase transformation and the active high-valent/intermediate state under bias.

Oxygen-vacancy and lattice-oxygen descriptors provide a LOM prior with an unusually sharp ambiguity. Wan et al. trained ML models for oxygen-vacancy formation energies across 1750 metal oxides, and Park et al. extended vacancy prediction into broader binary-to-quinary oxide spaces (Figure 13c,d) [144,145]. These studies are valuable because vacancy energetics are expensive to compute directly across large oxide libraries. Wan et al. showed that physically interpretable descriptors can support rapid prediction of oxygen-vacancy formation energy across structurally diverse oxides, while Park et al. used an ensemble of graph-based models to explore latent chemical space and reduce uncertainty by comparing model agreement. Together, they make oxygen-release tendency a scalable descriptor. The mechanistic meaning, however, remains conditional. Low vacancy formation energy can indicate useful lattice-oxygen participation, destructive oxygen loss, or a surface that reconstructs before either state is reached. High vacancy cost can suppress degradation while locking the catalyst into a scaling-limited AEM regime. The dynamic question is whether the predicted vacancy tendency becomes reversible oxygen participation within a safe LOM window, vacancy healing, a self-limited reconstructed surface, or an irreversible defect cascade.

Static stability descriptors are useful filters, not failure-path labels. Formation energy, decomposition energy, Pourbaix stability, dissolution tendency and endpoint retention can remove materials with no plausible pH-potential window. Li et al. showed this logic through lanthanide-regulated Ru–O covalency in acidic OER catalysts (Figure 13e) [146]. Their descriptor is not a simple dopant identity but the continuously tuned Ru–O covalency generated by Ru–O–Ln orbital coupling. DFT showed that both lattice-oxygen vacancy formation and Ru-vacancy formation depend on this covalency, producing a volcano-like stability trend rather than a monotonic rule. Er-RuO_x sits near the optimum: Ru–O bonding is weakened enough to improve activity but not so much that Ru

becomes easily leached or lattice oxygen becomes excessively labile. This is a strong static-stability prior because it links orbital coupling, vacancy energetics and acidic durability before extensive operation. Yet it still does not identify the first failure node during OER. Operando validation is needed to determine whether degradation begins from oxygen loss, Ru overoxidation, dopant loss, surface reconstruction or another coupled pathway. Static ML can narrow the chemical search space, but it cannot assign mechanism during operation. Its outputs feed dynamic experiments and trajectory models as priors for mechanism tendency, safety-window selection and first-failure-node risk.

A static descriptor becomes more useful when it is written with a falsification route. If adsorption energy predicts an AEM-favorable surface, the next experiment tests whether the expected intermediate population actually appears under bias. If vacancy formation energy predicts LOM accessibility, the experiment tests vacancy generation, oxygen exchange and refilling, not only higher current. If Ru–O covalency or Pourbaix stability predicts a narrow safe window, the model is challenged by a protocol that pushes the boundary while tracking dissolution, oxygen exchange and structural persistence. This counterfactual use of static ML gives each descriptor a job it can fail: adsorption descriptors must predict intermediate population, vacancy descriptors must predict oxygen exchange and healing, and stability descriptors must predict the first failure boundary. This is more valuable than treating static descriptors as vague explanations after the activity is known.

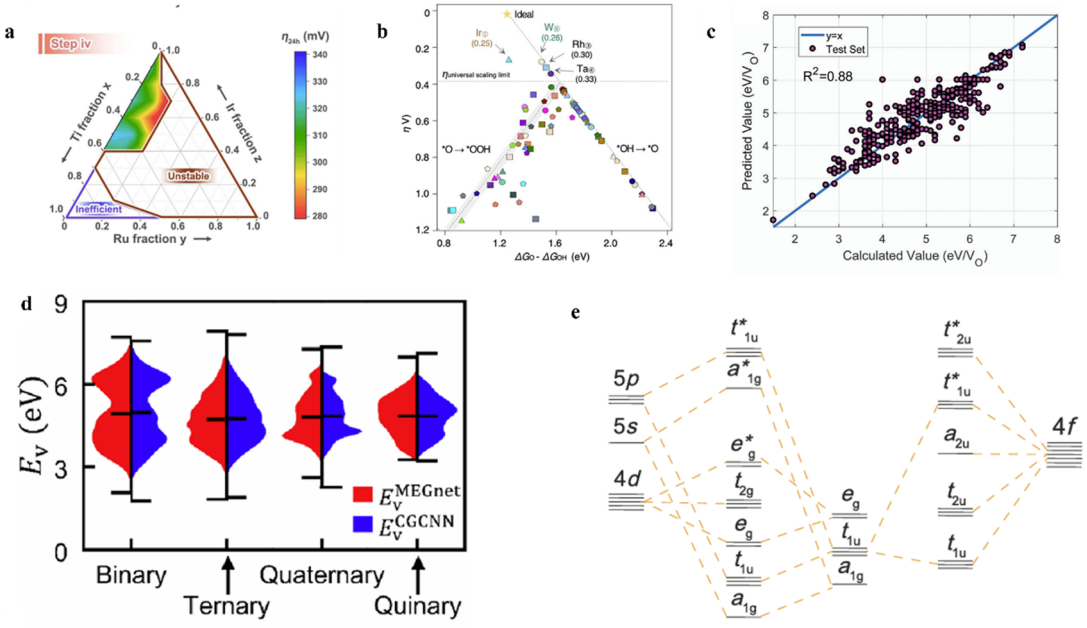


Figure 13. (**a**) Steady-state activity map of $SrTi_xRu_yIr_zO_3$ perovskite oxides after acidic OER stability screening, showing the composition window that avoids inefficient and unstable regimes. Adapted with permission from Ref. [141]. Copyright 2023, John Wiley and Sons. (**b**) ML-predicted OER volcano plot identifying W_1–NiFeOOH as a promising noble-metal-free oxyhydroxide catalyst. Adapted with permission from Ref. [143]. Copyright 2026, Springer Nature. (**c**) LS-SVM prediction of oxygen-vacancy formation energies in metal oxides, showing the agreement between calculated and ML-predicted E_{OV} values. Adapted with permission from Ref. [144]. Copyright 2021, Royal Society of Chemistry. (**d**) ML-ensemble prediction of oxygen-vacancy formation-energy distributions across binary, ternary, quaternary, and quinary oxide composition spaces. Adapted with permission from Ref. [145]. Copyright 2023, American Chemical Society. (**e**) Qualitative molecular orbital diagram showing Ru–O–Ln orbital coupling as a descriptor for tuning Ru–O covalency in acidic OER catalysts. Adapted with permission from Ref. [146]. Copyright 2024, Springer Nature.

3.3. Dynamic ML for Pathway Assignment: Progress and Limitations

Current dynamic ML for mechanism–degradation coupling is limited less by model availability than by mechanism-sensitive labels. After static ML has provided priors for AEM-like adsorption, lattice-oxygen participation, oxide-path behavior and degradation risk, the dynamic task is to calibrate these priors into time-resolved pathway weights, safe-window boundaries and first-failure-node labels. Operando Raman, FTIR, XAS, DEMS, isotope labelling and ICP-MS each observe a different part of OER, while long stability tests are rarely synchronized with these probes. A temporal model can fit current or voltage with impressive accuracy and still

miss the pathway that produced the signal. The central gap is calibration: the field has many time series, but few records that convert them into pathway weights, safe windows and first-failure labels.

Mechanism-sensitive labels are sparse and indirect. Pandya et al. used high-speed compressive Raman imaging to reveal concurrent OER pathways in alpha-Li_2IrO_3 (Figure 14a) [147]. This study is a strong template because it does not compress the catalyst into one averaged spectrum or one global mechanism. By spatially and temporally tracking Raman stretching modes in individual particles, the authors followed how charge compensation changes with potential, electrolyte and cycling history. At low overpotentials, water oxidation is coupled to bulk ion exchange: charge generated at the surface can be compensated by cation movement into the crystalline particle, so the reaction history extends beyond the outermost surface. At higher overpotentials, charge compensation shifts toward surface redox-active sites, resembling a more conventional crystalline-oxide OER response. The important ML lesson is that the same catalyst can occupy different mechanism regimes within one experiment. A Raman band is therefore not a universal concentration label. It is a local, potential-dependent state marker whose meaning depends on catalyst family, electrolyte, optical penetration depth, particle geometry and cycling history. A defensible dynamic record should keep the spectral feature, potential, electrolyte, particle region, spatial sampling depth, gas-evolution context and band-assignment uncertainty linked in the same entry.

If the first calibration problem is that the same catalyst can move between mechanism regimes, the second is that the candidate mechanism library itself may be incomplete. Mechanism-weight learning needs multimodal calibration. Activity alone cannot raise w_{LOM}, because rate can also increase through active-site density, adsorption energetics, solvation or transport. Isotope-labelled DEMS, oxygen-exchange evidence, vacancy signatures, spectral redox features and dissolution flux need to constrain the same latent pathway weights. Usama et al. re-examined $IrO_2(110)$ and showed that Walden-type routes, where O_2 formation and water adsorption occur concurrently, can outperform traditional mononuclear, bifunctional and oxide descriptions depending on surface configuration (Figure 14b) [148]. The significance of this work is not only that a new pathway is proposed. It shows that even a model surface such as $IrO_2(110)$ does not have a single mechanism when surface hydroxylation, oxygen coverage and OOH-covered states are allowed to vary. Different surface configurations favor different limiting spans, and mechanisms that are absent from the candidate library cannot be recovered by fitting current. For dynamic ML, this is a direct warning: if the mechanism library contains only AEM and LOM, unexplained current will be forced into the wrong channel. Mechanism-weight models therefore need an explicit residual or out-of-library head. When this residual grows, the correct response is not to over-interpret the existing labels, but to trigger targeted experiments or calculations that test missing routes such as Walden-type O_2 release, intramolecular O–O coupling or surface-configuration-dependent pathways.

Degradation learning needs first-failure-node labels. Van der Merwe et al. linked OER and Ir dissolution in amorphous hydrous iridium oxides to electronic and structural transformations under PEM-relevant conditions (Figure 14c) [149]. Their work is important because it separates two processes that are often merged into one activity–stability narrative. Using *in situ* and operando Ir L_3-edge XAS together with DFT, they proposed a hydrous, H-terminated nanosheet-like model for amorphous IrO_x rather than interpreting the catalyst through crystalline rutile IrO_2 alone. Under anodic operation, this structure evolves from H-terminated motifs toward shorter Ir–O environments with multiple Ir vacancies. Crucially, Ir dissolution can begin below the apparent OER activation region, meaning that metal loss is not simply a late consequence of high current. It can be a parallel thermodynamic pathway that is already available before strong O_2 evolution. This changes the ML target: degradation should not be learned only from final current decay or post-test Ir loss. The record needs the first Ir-defect formation signal, the potential window where dissolution begins, the evolving Ir–O coordination, and whether the OER-active state and dissolution-active state are the same or only coupled.

Wang et al. showed a different stabilizing logic in crystalline RuO_2, where atomic Ga creates adaptable oxygen-radical donor sites that support O-O coupling while retaining acidic durability (Figure 14d) [150]. In Ga-doped interconnected RuO_2 nanocrystals, Ga sites are not treated as conventional high-activity metal centers. Instead, atomically dispersed Ga–O motifs act as oxygen-radical donors whose flexible Ga–O bonding helps synchronize oxygen radicals on neighboring Ru sites. This spatiotemporal coordination promotes direct O–O radical coupling through an oxide-path-type mechanism, avoiding the full coordination-number collapse and vacancy penalty typically associated with destructive LOM. The optimized catalyst maintains strong acidic OER activity and long stability, including PEMWE-relevant operation. This case is useful because it shows that mechanism cost is not determined by oxygen participation alone. Oxygen radicals can be destabilizing when they create unrepaired vacancies, but they can also be stabilized when neighboring sites coordinate their timing and spatial arrangement. Together, the IrO_x and Ga–RuO_2 cases show why mechanism cost cannot be learned from current decay alone. Beneficial oxygen participation, radical stabilization and destructive oxygen loss can share

partial spectral signatures until dissolution, vacancy or structural evidence separates them. The missing output is the first detectable loss node, its path probability and the pre-failure mechanism window that caused it.

Label confidence belongs with the target rather than hidden in the prose. A direct label may come from isotope-resolved O_2, online dissolution or spatially resolved operando spectroscopy. A constrained label may come from synchronized spectra, current, redox charge and DFT-supported assignment. A weak label may come from activity trends alone. These ranks tell the model whether it is learning mechanism evidence or only a proxy. Without this distinction, abundant low-information measurements can dominate the training set and make a mechanism model look more certain than the experiment allows.

The time axis also needs calibration. Spectral redox changes, isotope oxygen release, current response and metal dissolution rarely peak at the same moment. A label assigned to the wrong time window can convert a cause into a consequence: ion exchange may compensate early OER charge, dissolution may precede strong O_2 evolution, and oxygen-radical coordination may stabilize an otherwise risky pathway before current decay appears. A dynamic record therefore stores lag windows between signals and allows delayed coupling between mechanism and cost. A model that assumes all channels are synchronous will miss precisely the history that makes OER difficult to learn. Therefore, dynamic ML for mechanism–degradation coupling should output more than a fitted current trace. The required targets are pathway weights with confidence levels, out-of-library probability, safe-window boundaries, first-failure-node probability and lag-aware coupling between redox, oxygen evolution and dissolution signals. With these labels, the model can test whether a catalyst is truly switching mechanism, entering a stabilized oxygen-participation regime, or approaching an irreversible degradation path.

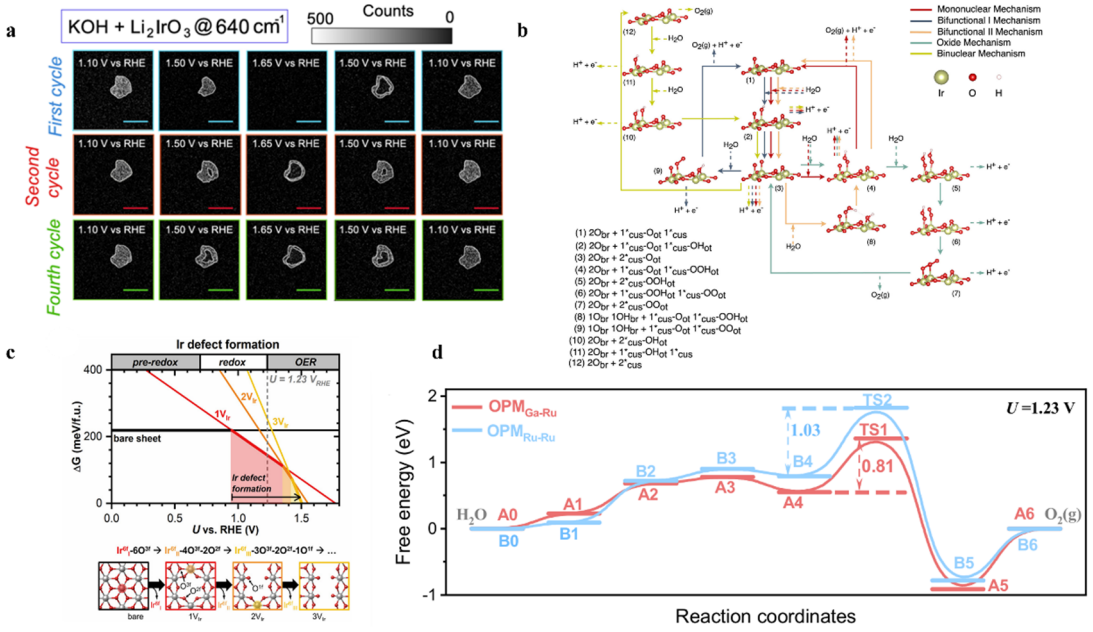


Figure 14. (**a**) Compressive Raman imaging of α-Li_2IrO_3 revealing concurrent OER charge-compensation pathways. Adapted with permission from Ref. [147]. Copyright 2024, Springer Nature. (**b**) Candidate OER mechanism network on IrO_2(110). The reaction network includes mononuclear, bifunctional, oxide, and binuclear pathways on a fully oxygen-covered IrO_2(110) surface, illustrating the diversity of mechanisms that must be considered when defining a candidate pathway library. Adapted with permission from Ref. [148]. Copyright 2025, Springer Nature. (**c**) DFT-predicted Ir defect formation in amorphous hydrous IrO_x, showing potential-driven Ir dissolution through progressive Ir vacancy generation under OER-relevant conditions. Adapted with permission from Ref. [149]. Copyright 2025, Royal Society of Chemistry. (**d**) Ga–Ru dual-site OPM pathway enabling direct oxygen-radical coupling on crystalline RuO_2. Adapted with permission from Ref. [150]. Copyright 2025, Springer Nature.

3.4. Learning Pathway Weights, Coverages and Stability Costs

Mechanism–degradation learning is written as four supervised tasks: mechanism-weight learning, coverage-trajectory learning, safe-window prediction and degradation-path probability. Each record starts with the working-state descriptors defined in Section 2, adds potential, pH, electrolyte and mechanism-sensitive measurements before a fixed prediction horizon, and predicts later pathway weights, coverage trajectories, lattice-oxygen safety and degradation paths. Model choice should follow the label structure rather than the popularity of an algorithm: mixture-of-experts models are suited to pathway weights, latent-state models to incomplete coverage evidence,

constrained multitask heads to safe-window prediction, and survival or competing-risk heads to failure routes. The relevant criterion is whether the model output matches the mechanistic claim. A task-first model choice prevents model capacity from substituting for mechanistic definition: the pathway, coverage, safe-window or failure label should be fixed before model selection.

A practical training sample contains observation masks as well as values. Most OER experiments will not measure Raman, isotope oxygen, ICP-MS, microscopy and device signals at every time point. Missing channels should therefore be marked as unobserved, not filled by interpolation that silently implies a measurement was made. The prediction horizon must be fixed before smoothing, baseline correction, peak fitting and feature selection, and every derived feature should retain the time window from which it was computed. This record design blocks post-event information from entering an early-state prediction under the disguise of a pre-event descriptor.

Benchmark tasks work best when they are event-centred rather than curve-fitting-centred. One task can ask whether the first activation window predicts the later mechanism switch. A second can ask whether early isotope or spectral evidence predicts the first dissolution node. A third can ask whether a model trained under smooth operation detects failure under intermittent operation before voltage drift becomes large. These tasks are harder than endpoint regression, but they test the questions that matter for catalyst design: when the state changes, what it changes into, and whether the change is useful or damaging.

Task 1 is mechanism-weight learning. Fe-S-modulated NiFe oxyhydroxide provides a concrete evidence structure: Luo et al. combined *in situ* ATR-FTIR, isotope-labelled DEMS, chemical probes and calculations to argue that Fe and S co-modulation creates compatible AEM and LOM pathways (Figure 15a) [151]. This case is useful because the two mechanism channels are not inferred from activity alone. During reconstruction, $NiMoO_4 \cdot xH_2O$@Fe,S is converted into R-NiFeOOH@SO_4, with Mo leaching and oxyhydroxide formation producing a working interface rather than preserving the precursor. Fe mainly optimizes metal-site adsorbate evolution by improving intermediate adsorption and OER kinetics, whereas S raises the O 2p-band center, weakens metal–oxygen bonding and activates lattice oxygen. ATR-FTIR constrains adsorbate evolution, isotope DEMS constrains lattice-oxygen contribution, and chemical probes separate metal-site and oxygen-site roles. The input record should therefore include precursor reconstruction history, Fe/S content, potential waveform, pH, electrolyte, isotope condition, FTIR/Raman/XAS features, DEMS signal and dissolution flux when available. The output is not a single "AEM" or "LOM" class, but $w_{AEM}(t)$, $w_{LOM}(t)$, possible $w_{OPM}(t)$, switching threshold, hysteresis and uncertainty. A mixture-of-experts model is appropriate here because mixed mechanisms are a feature of the chemistry, not a classification error.

Task 2 is coverage-trajectory learning. The IrO_x and cobalt hydroxide cases discussed above provide the corresponding evidence structure: redox-active state density, high-valent-state fraction and *O/M=O-like population must be tracked as time-dependent variables rather than inferred from adsorption energies alone. The model needs to infer generation, accumulation, conversion and removal of intermediates from current, spectra, adsorbate-sensitive signals and computed adsorption priors. The outputs are coverage proxies, residence time, O–O coupling probability and coverage-dependent kinetics. Computed adsorption energies enter as priors because they describe plausible site energetics; they are not ground-truth operating coverage. Post-test characterization belongs in plausibility auditing or late-state prediction, not in early-time coverage labels. This design prevents the common leakage in which a descriptor calculated or measured after reconstruction is used to predict the reconstruction itself.

Task 3 is safe-window prediction. The model should learn the operating range in which lattice-oxygen participation, vacancy formation, oxygen replenishment and metal retention remain compatible. TiO_x-supported Ir nanoparticles illustrate why this window is not an intrinsic property of one element, but a result of the working-state trajectory. Zhang et al. showed that acidic OER can reconstruct metallic Ir into rutile IrO_2, shifting the mechanism away from persistent LOM participation and improving durability (Figure 15b) [152]. Conventional Ir nanoparticles usually form a disordered hydrous IrO_x shell, which is active but prone to LOM-related oxygen-vacancy accumulation and Ir dissolution. In contrast, the TiO_x@Ti substrate drives a bulk transformation from metallic Ir to crystalline rutile IrO_2. This support-guided phase trajectory suppresses persistent lattice-oxygen participation and shifts the reaction toward a more complete AEM route while retaining activity and durability. The safe window is therefore created by the transition from metallic Ir to crystalline IrO_2, rather than by Ir composition alone. The dynamic label should include reconstruction route, crystalline-phase fraction, LOM suppression, Ir dissolution onset and stability after phase formation.

Liu et al. reported a NiFe LDH/FeMoO heterostructure that represents the opposite side of the same safe-window problem: lattice oxygen is deliberately activated rather than suppressed (Figure 15c) [153]. The NiFe LDH/FeMoO interface redistributes charge between NiFe LDH and FeMoO, creates oxygen vacancies and forms an internal electric field that enables lattice oxygen to participate directly in OER. However, the electrode remains

stable at 2 A cm^{-2} for 3000 h, indicating that LOM can be productive when vacancy formation, oxygen replenishment and Fe stability are kept within a controlled regime. Zheng et al. further designed Ta/B co-doped nanoporous RuO_2, in which Ru–O–Ta frameworks stabilize Ru sites and help replenish oxygen vacancies [142]. Together, these cases show that lattice-oxygen participation and lattice-oxygen loss must be separated [154]. The required outputs are not simply "LOM active" or "LOM suppressed", but the safe-window boundary, vacancy accumulation rate, vacancy healing or refilling probability, dissolution onset, interfacial charge redistribution and voltage drift under the stated protocol [155].

Task 4 is degradation-path probability. The input is the pre-failure history: mechanism weights, coverage features, lattice-oxygen evidence, dissolution flux, impurity exposure and potential program. The outputs are $P_{dissolution}(t)$, $P_{phase\text{-}change}(t)$, $P_{passivation}(t)$, $P_{poisoning}(t)$, $P_{repair}(t)$ and remaining useful lifetime. Zhou et al. used ML screening and steam-assisted synthesis to build an integrated Ru/$TiMnO_x$ electrode with intrinsic metal-support interactions and self-healing behavior during long OER operation [156]. This example matters because repair and degradation can occur together. A catalyst may lose active metal, reconstruct the support interface, replenish oxygen vacancies or re-stabilize the active phase within the same test. A monotonic decay curve would miss this competition. Survival and competing-risk formulations are therefore useful, but only if the first loss node is measured rather than guessed. The model should learn whether failure begins from metal dissolution, phase drift, passivation, support corrosion, vacancy accumulation or unsuccessful repair.

Trajectory learning is credible only under leakage-safe validation. Kaufman et al. defined leakage as target information unavailable at prediction time, and Roberts et al. showed how weak splitting, incomplete documentation and biased preprocessing can make ML models appear useful while failing under real validation (Figure 15d) [157,158]. For OER, the equivalent leakage is straightforward: future spectra cannot predict earlier mechanism weights, post-test composition cannot enter an early failure forecast, and random time windows from the same electrode, isotope experiment or stability run cannot be split across train and test sets. Baseline correction, peak fitting, denoising and feature selection must be learned only from the training set. Strong validation should hold out mechanism class, pH, protocol, electrolyte, current range, catalyst family or device format. Only then can a model claim that it has learned mechanism cost rather than memorized one experiment.

Quantitative assessment must match the object being predicted. A model that predicts the approximate shape of a trajectory but misses the transition time, or predicts the correct event time but with poor calibration, should not be judged by a single generic R^2 value. Table 2 defines a minimum reporting set for dynamic OER ML. Each dynamic model should also be compared with simple baselines so that gains from temporal information are separated from gains caused only by model capacity.

Table 2. Minimum evaluation metrics, baselines and leakage-safe validation rules for dynamic OER ML.

Prediction Type	Core Metrics	Minimum Baselines	Preferred Split Unit	Leakage Inspection
Continuous trajectory	MAE/RMSE or NRMSE + DTW distance; trajectory correlation	Static endpoint model; persistence/last observation; simple linear temporal model	electrode/run, batch, catalyst family, protocol	No overlapping windows across splits; scaling/smoothing fitted on training data only
Event time (onset/switch/failure)	absolute/median event-time error; tolerance-window accuracy	constant-event-time; last-state; simple hazard/change-point baseline	independent run/protocol/family	No future spectra or post-event features in early prediction
State/pathway classification	balanced accuracy; macro-F1; AUROC/AUPRC when appropriate	majority/prior classifier; static-descriptor classifier	electrode/run and catalyst family	Repeated measurements and particles from one physical sample remain in one split
Survival/degradation	C-index; time-dependent AUC; integrated Brier score; calibration	Kaplan-Meier/group baseline; simple Cox or parametric survival model	run, protocol, electrolyte, device	Post-test composition/microscopy excluded; censoring handled explicitly
Cross-protocol/device transfer	NRMSE/DTW + event errors + calibration under held-out boundary	within-domain model; metadata-only correction; no-history ablation	held-out pH/electrolyte/waveform/current range/device	Same reservoir, stack run or duplicated protocol cannot appear in both train and test

Leakage checklist. Before reporting transfer performance, the authors should verify that: (i) electrode/run and synthesis replicates are group-split; (ii) overlapping time windows do not cross train/test boundaries; (iii) post-test characterization and future-time signals are excluded from early predictions; (iv) normalization, denoising,

baseline correction, peak fitting and feature selection are fitted on training data only; (v) repeated measurements from the same physical sample and shared electrolyte reservoirs remain within one split; and (vi) uncertainty and censoring are reported rather than converted silently into exact labels.

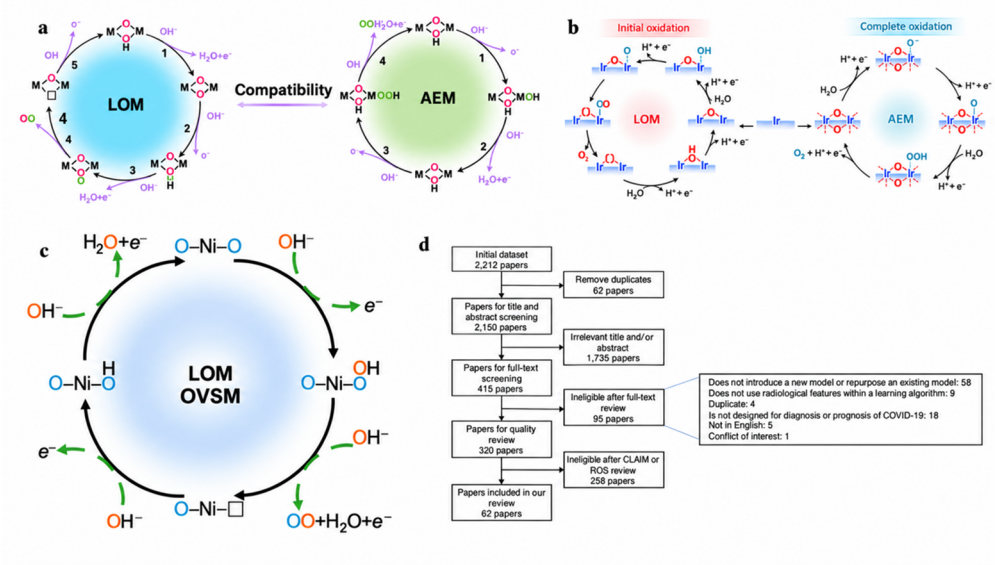


Figure 15. (**a**) Compatible AEM–LOM pathway on Fe,S co-modulated NiFeOOH@SO_4 for alkaline OER. Adapted with permission from Ref. [151]. Copyright 2024, Springer Nature. (**b**) Metallic Ir-to-rutile IrO_2 reconstruction enabling an LOM-to-AEM mechanistic shift during acidic OER. Adapted with permission from Ref. [152]. Copyright 2025, Springer Nature. (**c**) Oxygen-vacancy-assisted LOM-OVSM pathway on NiFe LDH/FeMoO. Adapted with permission from Ref. [153]. Copyright 2026, Springer Nature. (**d**) Quality screening of machine-learning studies, highlighting the need for rigorous preprocessing, data partitioning and validation. Adapted with permission from Ref. [158]. Copyright 2021, Springer Nature.

4. Operating-Boundary Control of Catalyst Trajectories

Operating conditions are trajectory selectors rather than background metadata. After active-state accessibility and mechanism cost have been defined, the next question is why the same material follows different histories in different tests. pH, electrolyte, waveform, transport, temperature and device architecture determine which interfacial states are accessible, which pathway weights dominate and which degradation route appears first. Metadata correction improves comparison, but protocol-aware learning must encode the actual history of pH, electrolyte, waveform, transport and device boundary (Figure 16).

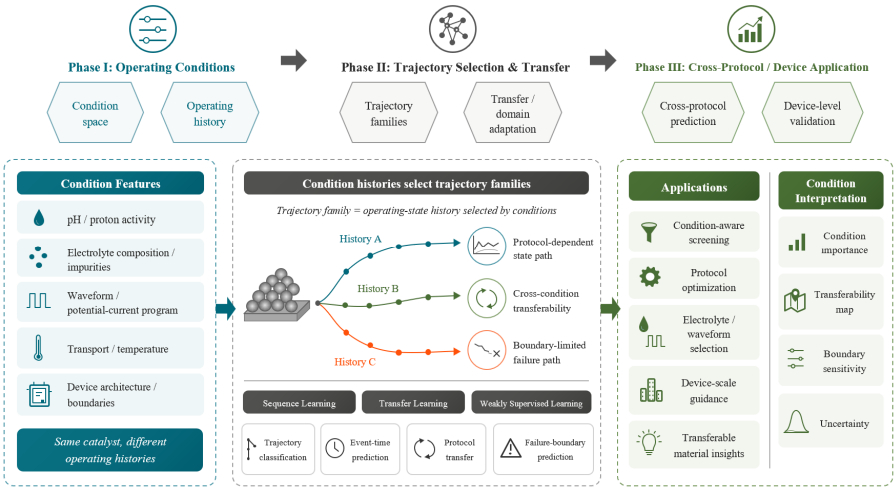


Figure 16. Condition-selected trajectory learning for OER catalysts. Operating conditions determine how the same catalyst follows different state histories. Dynamic ML links condition features to trajectory families, cross-protocol transfer and device-relevant validation, enabling condition-aware screening, protocol optimization and failure-boundary prediction.

4.1. pH, Waveform, Transport and Device Architecture Select State Histories

This section treats operating boundaries as trajectory selectors rather than background testing conditions. Four experimentally visible variables are separated: pH/electrolyte access, waveform memory, transport-shaped apparent kinetics and device architecture. Each variable changes the state history before it changes the endpoint number. The ML consequence is a condition record that stores what the catalyst experienced, not only the nominal cell setup. In this framework, pH, electrolyte identity, waveform, flow field and device format are not secondary metadata. They decide which redox states, hydration states, ion-exchange processes, transport gradients and degradation routes become accessible during OER.

pH and electrolyte identity select which interfacial redox, hydration and ion-exchange states are accessible before and during OER. Huang et al. showed that pH-dependent cobalt oxidation controls OER at cobalt-based interfaces (Figure 17a) [159]. This case is important because pH is not treated as a simple thermodynamic correction. Operando Co K-edge XAS tracks the shift of the Co absorption edge during OER, allowing Co oxidation-state changes to be followed as a function of potential and current. In alkaline electrolyte, the lower flat-band potential and earlier Co redox transformation favor surface reconstruction and charge accumulation at lower overpotential. In neutral and acidic media, the Co redox transition shifts anodically; in neutral electrolyte, slow Co oxidation and poor interfacial polarizability give the largest additional kinetic penalty. Thus, the relevant label is not only bulk pH, but the potential at which Co oxidation begins, the rate of Co oxidation-state change, the redox charge stored before OER and the reversibility of the reconstructed interface.

Liang et al. found that pH-dependent water oxidation on iridium oxides cannot be reduced to a universal Nernst correction because different IrO_x structures carry different balances of surface charge, proton transfer and hydration [160]. Electrolyte ions add another layer [161]. van der Heijden et al. showed Li^+ activation of NiFeOOH in NaOH and KOH, while Chen et al. showed that ions change IrO_x activity and stability in interface-specific ways [162,163]. Zhu et al. further showed that reconstructing a connected hydrogen-bond network at the catalyst–electrolyte interface can enrich interfacial water and facilitate proton-transfer and dehydrogenation processes during acidic OER, demonstrating that interfacial water organization can directly reshape the reaction environment [164]. For ML, pH and salt name are therefore too thin. Useful condition labels include pH history, buffer capacity, cation and anion identity, electrolyte exchange sequence, redox charge, hydration or solvation probes, interfacial water orientation, activation time and whether electrolyte exposure occurs before or only during OER.

The same potential can correspond to different catalyst states after different waveform histories. Linear sweep, potential hold, activation cycling and start–stop operation reach the same voltage through different routes, leaving different valence distributions, hydration states, defect populations and dissolved-metal histories (Figure 17b) [165]. Dynamic PEM operation makes this point at the system level: renewable coupling can impose current, pressure, temperature and reaction-rate changes on the electrolyzer, while start–stop cycles may accelerate component erosion [166,167]. Li et al. treated voltage fluctuation tolerance as a distinct OER property in manganese oxides [168]. These cases make memory experimentally observable. The same voltage carries both the instantaneous driving force and the history by which the catalyst arrived there. A trajectory dataset therefore needs waveform amplitude, ramp direction, dwell time, rest time, cycle count, off-state exposure, recovery current and post-cycle redox charge. Hysteresis should be treated as an output because it tests whether two routes to the same potential have produced the same working state.

At high current density, measured activity often reflects a coupled kinetic-transport trajectory. Veroneau et al. modelled local pH gradients during OER and showed that the interfacial pH can deviate from the bulk solution (Figure 17c) [169]. This is especially important because OER generates protons at the anode. Even when the bulk electrolyte is buffered or alkaline, high current density can shift the interfacial pH away from the nominal bulk value and create a locally less alkaline, or more acidic, reaction environment near the catalyst surface. The model links local pH to bulk pH, buffer composition, pKa, current density and mass transport, showing that the catalyst may experience a reaction environment different from the one written in the experimental section. Kim et al. improved OER by using three-dimensionally stack-printed catalysts that facilitate bubble removal, while Dastafkan et al. monitored bubble evolution through high-frequency impedance [170,171]. Geuß et al. quantified Ir dissolution in a gas-diffusion-electrode half-cell under electrolysis-relevant conditions [172]. Together, these cases show that local pH, bubble coverage, impedance, pressure, heat and mass transport can change both apparent kinetics and degradation path. A useful model separates intrinsic state variables from transport variables by measuring at least one local pH, bubble, impedance, pressure or temperature proxy [173,174]. Otherwise voltage drift becomes an ambiguous mixture of catalyst evolution and environment evolution.

Device architecture changes the catalyst from a uniform half-cell object into a spatially distributed operating system. Knöppel et al. showed that aqueous model cells can misrepresent OER stability under practical constraints (Figure 17d–f) [175]. Their comparison between aqueous model systems and membrane electrode assemblies is

especially instructive. In aqueous flow-cell measurements, dissolved Ir species are transported directly into the electrolyte and detected by ICP-MS. In MEA operation, the catalyst layer is coupled to a polymer electrolyte, water transport, gas transport, membrane uptake, local acidity and possible redeposition or retention pathways. As a result, dissolution stability measured in aqueous systems can differ from MEA-relevant stability by orders of magnitude. The key lesson is that the device boundary changes the degradation trajectory, not merely the measured lifetime.

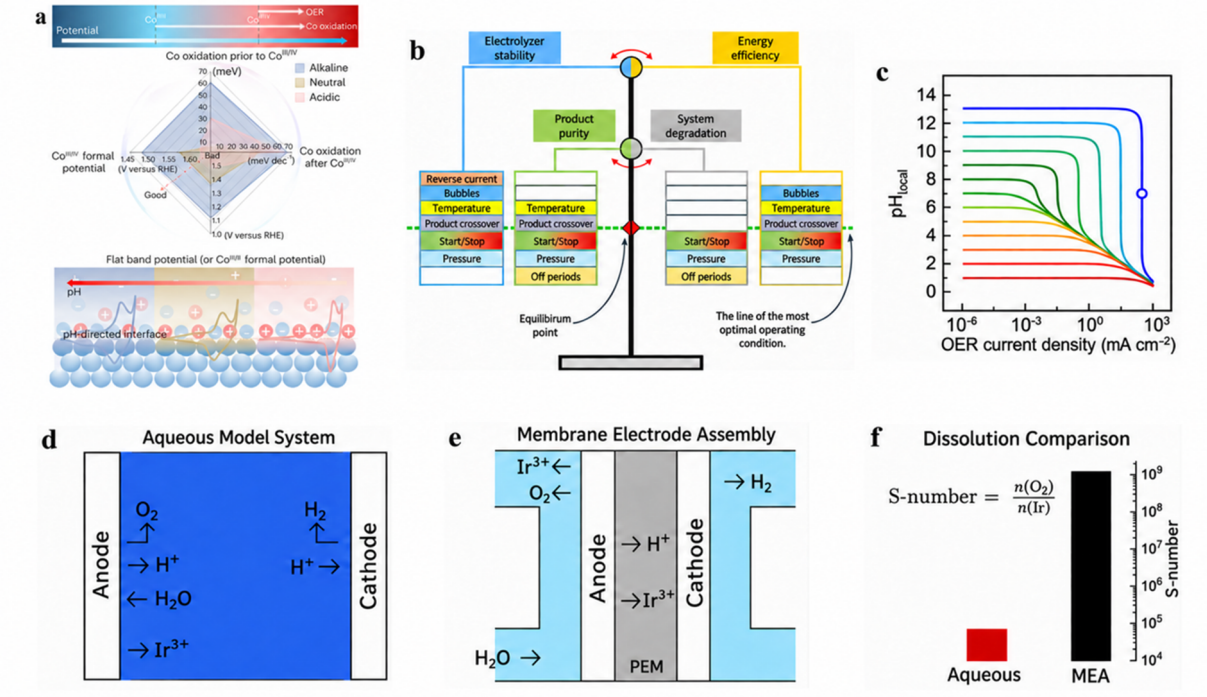


Figure 17. (**a**) pH-dependent Co oxidation states governing OER activity at cobalt oxide interfaces. Adapted with permission from Ref. [159]. Copyright 2025, Springer Nature. (**b**) Dynamic PEMWE operation pathways linking start–stop history, transport changes and degradation risks. Adapted with permission from Ref. [165]. Copyright 2025, MDPI. (**c**) Local pH deviation from bulk solution during high-current-density OER. Adapted with permission from Ref. [169]. Copyright 2024, American Chemical Society. (**d**–**f**) Aqueous model cell versus MEA testing of IrO_x OER stability, showing architecture-dependent transport environments and large differences in apparent dissolution stability. Adapted with permission from Ref. [175]. Copyright 2021, Springer Nature.

Tran et al. linked reactivity and stability in reduced-Ir TiO_2-supported anodes, Lee et al. altered the catalyst-layer environment through an ionomer-free porous-transport electrode, and Zhang et al. improved PEM water electrolysis with tunnel-structured IrO_x [176–178]. Weber et al. further showed that the porous-transport-layer interface controls catalyst utilization and performance [179]. These examples modify different parts of the device boundary: support interaction, ionomer contact, water access, gas pathway, electronic continuity, compression and local catalyst utilization. A device-aware label is therefore not MEA activity alone. It includes utilization fraction, local water access, ionomer or membrane contact, PTL interface condition, gas-removal efficiency, dissolution retention pathway, device-transfer score and the probability that a half-cell active state survives the device boundary [180].

The broader implication is that condition transfer cannot be learned from endpoint normalization alone. A model trained only on half-cell overpotential, nominal pH and catalyst composition may appear predictive while missing the actual selector of the trajectory. Dynamic ML should encode operating boundaries as histories: electrolyte exposure before activation, waveform route to the working state, local transport environment and device architecture. The corresponding outputs are not only activity and stability, but redox-accessibility shifts, hydration or ion-exchange state, hysteresis, local transport penalty, degradation-route change and device-transfer probability. Only with these labels can the model distinguish a catalyst that is intrinsically active from one that only appears active under favorable transport, or a material that is stable in a half-cell from one whose working state survives a practical device boundary.

4.2. Static ML for Protocol Correction and Metadata Normalization

Static ML can reduce false comparisons between operating boundaries, but it cannot recover the history through which a measured state was produced. After pH/electrolyte access, waveform memory, transport-shaped kinetics and device architecture have been defined as trajectory selectors, static ML should be used mainly as a normalization and provenance tool. Metadata such as pH, electrolyte, loading, substrate, current density, reference electrode, resistance correction and stability protocol are necessary correction variables. They improve bookkeeping, reduce scatter and prevent obviously unfair comparisons. However, they remain static labels unless the model also sees how these quantities changed during activation, operation and recovery. In this section, static ML is therefore treated as a normalization tool rather than a trajectory-learning method.

Metadata correction is the first useful role of static ML. Mahajan et al. built a research database for experimental electrocatalysis that records contextual variables often missing from performance tables, including material properties, characterization data, electrochemical testing conditions and performance metrics (Figure 18a) [181]. The value of this database is not only that it stores more data, but that it makes experimental provenance explicit. Synthesis, characterization, catalyst testing and post-test information are separated as different parts of the workflow, allowing users to compare measurements with clearer knowledge of how they were produced. Jiang et al. used ML to predict OER activity for transition-metal hydroxide electrocatalysts, showing how composition, morphology, phase, electrolyte pH and working-electrode type can support rapid overpotential prediction and candidate ranking. (Figure 18b) [182]. These efforts improve comparability, yet they cannot decide why pH, electrolyte, morphology or loading changed the measured activity. A static correction may capture that one electrolyte, support or electrode type gives lower overpotential; it does not reveal whether the cause was redox access, hydration, impurity blocking, local alkalization, bubble removal or transport relief.

Protocol labels prevent unfair stability comparisons but are still too coarse to encode memory. Zlatar et al. proposed benchmarking guidelines for OER in aqueous electrolytes, including accelerated stress tests and backing-electrode effects (Figure 18c) [183]. This study is useful because it shows that stability is not only a property of the catalyst powder. The lower potential limit in an accelerated stress test and the backing electrode can change the apparent activity–stability relationship by introducing substrate passivation, redeposition, background OER contribution or altered dissolution behavior. Thus, a gentle galvanostatic hold, a square-wave AST and an aggressive potential-cycling protocol cannot be treated as equivalent "stability tests." The boundary is that protocol names compress waveform history. Two accelerated tests can share the same label but differ in potential window, dwell time, scan rate, rest interval, electrolyte replacement, backing-electrode chemistry and recovery time. Static ML can use these fields to avoid false comparisons, but it cannot reconstruct the valence, defect, bubble and dissolution histories generated during the test.

Correction parameters are valuable when they are interpreted as measurement conditions, not as chemical causes. Sauvé et al. used open-circuit-potential decay transients to quantify interfacial pH swings during high-current-density electrocatalysis [184]. The lesson is transferable to OER: bulk pH, nominal current density and geometric area do not define the interfacial state. A static correction can include pH, uncompensated resistance, current density, rotation rate, flow rate, loading, roughness factor and buffer identity, but it cannot recover the time-resolved local environment that produced the measured current. At high current density, the catalyst may experience interfacial pH shifts, locally less alkaline or more acidic conditions, bubble shielding, reactant depletion, heat accumulation or altered ion activity even when the bulk electrolyte remains unchanged. A model trained on corrected activity may therefore learn mass-transfer relief or local pH gradients as if they were intrinsic kinetics. Static correction improves bookkeeping; it does not separate intrinsic activity from apparent activity.

Device and cell labels improve cross-system comparison but do not describe local operating fields. Zhao et al. compared metal-doped IrO_2/TiO_2 catalysts in rotating-disk-electrode and membrane-electrode-assembly configurations, illustrating how the same catalyst family can behave differently when the architecture changes (Figure 18d) [185]. In their comparison, Ni-doped IrO_2/TiO_2 showed the best RDE activity and was also validated in MEA with the lowest cell potential, suggesting useful cross-configuration consistency. Yet the same work also shows why an RDE label and an MEA label are not enough. MEA performance depends on catalyst-layer structure, ionomer contact, water supply, porous transport layer, gas removal, membrane interface and local ohmic/transport fields, none of which are fully described by the catalyst composition alone. A static label can separate RDE, GDE, MEA and electrolyzer data, which already avoids severe extrapolation. It cannot recover local dry-out, ionomer blockage, oxygen-removal efficiency, compression effects or current hot spots. Static condition labels are correction variables. Dynamic ML replaces them with condition histories, local operating states and transfer tests, including electrolyte-exposure sequence, waveform-derived memory, interfacial pH or transport proxies, catalyst-layer utilization, dissolution-retention pathway and the probability that a half-cell working state survives the device boundary.

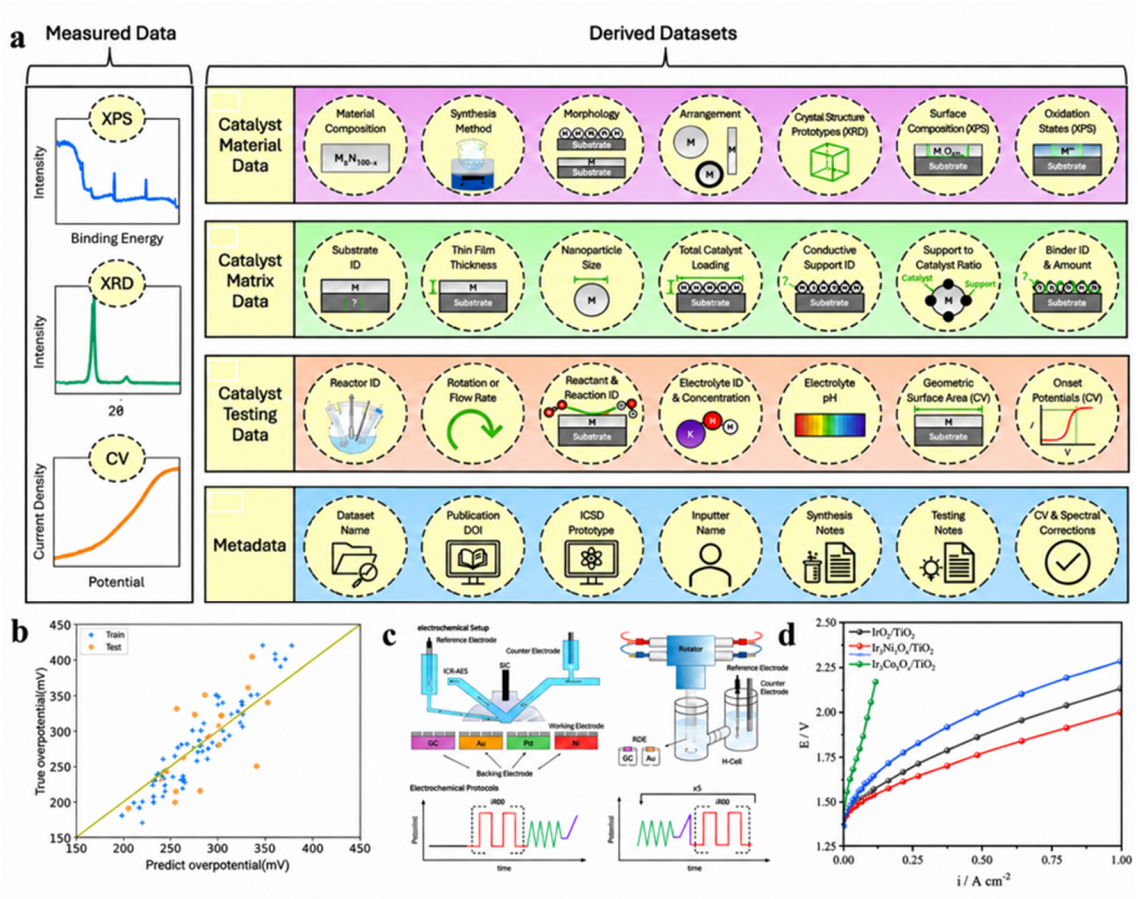


Figure 18. (**a**) Structured electrocatalysis metadata workflow for converting raw measurements into ML-ready experimental datasets. Adapted with permission from Ref. [181]. Copyright 2025, AIP Publishing. (**b**) ML prediction of OER overpotential for transition-metal hydroxide catalysts using composition and basic experimental descriptors. Adapted with permission from Ref. [182]. Copyright 2022, American Chemical Society. (**c**) OER benchmarking workflow combining AST protocols with backing-electrode selection in aqueous model cells. Adapted with permission from Ref. [183]. Copyright 2023, American Chemical Society. (**d**) MEA performance and durability of metal-doped IrO_2/TiO_2 catalysts under acidic OER conditions. Adapted with permission from Ref. [185]. Copyright 2024, American Chemical Society.

4.3. Dynamic ML for Condition-Dependent Trajectories: Progress and Limitations

Dynamic ML becomes essential for boundary selection because the relevant variables are histories rather than fixed experimental labels. pH, electrolyte, potential, current, temperature, gas coverage and device state should be treated as time-dependent signals that select the working-state trajectory. The unresolved problem is not model availability, but synchronization: OER datasets rarely measure condition history, interfacial state and device response on the same clock. Without this synchronization, a model can reproduce a voltage trace while still missing why the catalyst entered a different active state, pathway distribution or failure route.

Condition features are often static while the interface is not. Wu et al. showed that the interfacial-water structure on RuO_2-based acidic OER catalysts evolves dynamically with the catalyst–electrolyte environment (Figure 19a) [186]. Using p-block-metal-doped RuO_2 catalysts together with operando ATR-SEIRAS and theoretical calculations, they showed that Ga–RuO_2 promotes the evolution of interfacial water from four-coordinated and two-coordinated hydrogen-bonded configurations toward a free-H_2O-enriched local environment. This redistribution reorganizes the interfacial hydrogen-bond network, facilitates proton-coupled electron transfer and lowers the energetic barrier for subsequent water dissociation, thereby enhancing acidic OER kinetics. For dynamic ML, electrolyte and potential should therefore not be stored only as scalar inputs. The record should include the interfacial-water-state distribution, hydrogen-bond-network organization, solvent-reorganization trajectory, proton-transfer environment and water-dissociation kinetics.

Tao et al. used multimodal operando characterization to resolve cation effects at the IrO_x-electrolyte interface during alkaline water oxidation (Figure 19b,c) [187]. This case is useful because it separates electrolyte effects on redox population from electrolyte effects on turnover. In 0.1 M MOH, the OER activity follows the cation trend

TMAOH > KOH > NaOH > LiOH. Operando optical spectroscopy shows that the energetics and population of IrO_x redox-active species are largely independent of the cation, whereas the intrinsic turnover frequency changes strongly. LICT, SEIRAS and QM/MM simulations then assign this difference to the interfacial solvent structure: larger cations generate a more disordered water network, more isolated or cation-coordinated water, and faster solvent reorganization during O–O bond formation. Thus, "KOH" or "LiOH" is not a complete condition label. The useful input is cation identity together with water-network order, potential of maximum entropy, isolated-water fraction, cation-coordinated-water fraction and uncertainty in the local interfacial state. Without these labels, a model may appear to learn a cation trend while actually absorbing unmeasured solvation structure, contamination, ageing or local pH history into a nominal electrolyte label.

Waveform memory cannot be learned from optimization reward alone when the state variables behind the optimized protocol are unmeasured. Spitzenpfeil et al. used AI-assisted experimental optimization for water oxidation catalysts, showing that iterative experimentation can tune the startup phase of nickel electrodes (Figure 19d) [188]. Their workflow is a useful example of closed-loop experimental search: potential profiles are generated, tested and updated through active-learning or reinforcement-learning logic. The later move from a flow cell to a scanning droplet cell also shows why experimental history matters, because reproducibility depends on starting each trial from a fresh and comparable electrode region. However, optimization alone does not automatically provide a transferable state law. A loop may discover a good activation waveform without measuring the active-layer growth, Ni oxidation-state access, hydration state, bubble coverage or dissolution onset that made the waveform successful. Protocol transfer therefore requires held-out waveforms, activation cycles, rest periods and current ranges, together with evidence that the predicted state history changed as expected.

Device-level signals are still underused as catalyst-state evidence. Gong and Na analyzed localized oxygen evolution and transport in PEM water electrolysis as functions of pressure, temperature and current density (Figure 19e) [189]. Their work shows that local static pressure and temperature can reveal oxygen transport regimes that are invisible in a current–voltage curve alone. At low voltage, the anode environment is close to a liquid-dominated state; at intermediate voltages, oxygen generation produces pressure fluctuations linked to bubble residence and detachment; at very high voltage, rapid oxygen removal can shift the signal toward a gas-dominated regime. This means that stack voltage is not only a catalyst signal. It also contains gas coverage, water transport, PTL/channel removal and local pressure history. Mohamed et al. developed ML-based simulation for PEM electrolyzer cells, and Sayed-Ahmed et al. analyzed PEM stack degradation under dynamic load operation with data-driven methods [190,191]. These studies show that stack voltage, impedance, temperature, pressure, gas crossover and water-balance signals can be learned when device histories are available. The missing bridge is alignment with catalyst-state labels. Device models reproduce operation; catalyst models explain local chemistry. Dynamic OER ML therefore requires catalyst-state measurements and device-response signals to be aligned on the same time base.

The unresolved gap is condition-to-trajectory learning. The model has to predict how a change in pH, electrolyte, waveform, transport or device boundary shifts the active state, pathway weight and degradation path. A dense voltage trace is not enough. The record needs at least one state-sensitive or environment-sensitive signal that can tell whether the same catalyst entered a different history. The required outputs include redox-accessibility shift, hydration or solvation state, waveform memory, transport penalty, device-state redistribution, pathway-weight change and degradation-route transition. In practice, this means combining condition histories with operando state probes, local environment proxies and device response. Only then can dynamic ML distinguish a genuine catalyst-state transition from solvation reorganization, transport relief, bubble removal or device-level redistribution.

4.4. Predicting Material–Protocol Trajectories across Protocols and Devices

The supervised object is the material-protocol-device trajectory. Schematically, the task is (material descriptors, x_0; protocol history, $u(0{:}\tau)$; device boundary, d) -> $y(\tau{:}T)$, where y contains the later working-state, intrinsic-activity, transport-loss and degradation trajectories. This formulation is deliberately stronger than material -> activity ranking. The same composition may follow a productive trajectory under one activation waveform and a destructive trajectory under another, or retain its working state in a half-cell but lose it after transfer to an MEA. Dynamic learning should therefore recommend material-protocol pairs rather than materials alone and should predict not only the expected endpoint but the path and uncertainty by which that endpoint is reached.

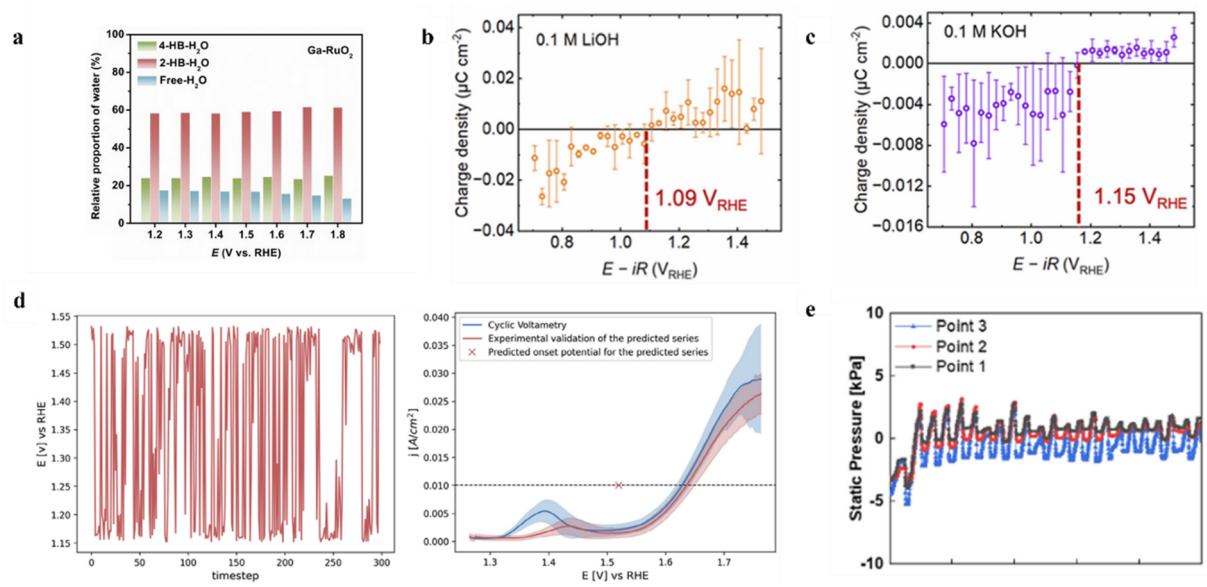


Figure 19. (**a**) Potential-dependent redistribution of interfacial water on Ga–RuO_2, showing the relative fractions of four-coordinated hydrogen-bonded water (4-HB H_2O), two-coordinated hydrogen-bonded water (2-HB H_2O), and free H_2O derived from operando ATR-SEIRAS. Adapted with permission from Ref. [186]. Copyright 2024, Wiley-VCH GmbH. (**b**,**c**) Cation-dependent LICT response at IrO_x/electrolyte interfaces in LiOH and KOH, showing different potentials of maximum entropy and interfacial water ordering. Adapted with permission from Ref. [187]. Copyright 2026, American Chemical Society. (**d**) ANN-guided startup-potential profile and experimental validation for nickel OER electrode conditioning. Adapted with permission from Ref. [188]. Copyright 2025, John Wiley and Sons. (**e**) Local static-pressure fluctuation in PEM water electrolysis, revealing oxygen bubble growth, detachment and transport dynamics. Adapted with permission from Ref. [189]. Copyright 2024, Elsevier.

Task 1 is protocol-history encoding. Sayed-Ahmed et al. reviewed dynamic PEM electrolyzer operation and emphasized that intermittent renewable power changes the stress experienced by electrolyzer systems (Figure 20a) [192]. The value of this case is that dynamic operation is not a single variable. Load flexibility, start-up/shut-down behavior, ripple current, pressure, temperature, gas crossover, water management and component degradation are coupled during operation. A PEM electrolyzer may respond quickly to renewable fluctuations, but the catalyst layer, membrane, PTL and balance-of-plant do not experience those fluctuations in the same way. Thus, the input cannot be reduced to "dynamic" or "steady". It should include E(t), j(t), ripple factor, scan rate, hold time, rest time, start–stop cycle, activation history, pressure history, temperature history and recovery period. The outputs are state memory, hysteresis, recovery probability and degradation sensitivity under the imposed waveform.

Task 2 is electrolyte and pH trajectory learning. This task follows the pH, electrolyte and interfacial-solvation effects discussed above, but writes them as time-dependent condition records rather than scalar metadata. The inputs include bulk pH, local pH estimate, cation and anion identity, buffer capacity, electrolyte replacement, impurity level, ionic strength, solvation evidence and electrolyte-exposure sequence when available. The outputs are redox-state access, ion-exchange probability, hydration state, interfacial-solvation regime, redeposition risk and poisoning risk.

Task 3 is transport and device-state learning. High-current PEM OER cannot be interpreted through catalyst energetics alone, as Zhong et al. discussed, and porous-transport-layer effects can control overpotentials at low anode catalyst loading, as Hasa et al. showed (Figure 20b) [193,194]. Hasa et al. made this device boundary explicit by varying PTL structure, porosity, thickness and microporous-layer design in PEM water electrolysis. Their key result is that adding a microporous layer improves PTL–catalyst-layer contact, promotes more uniform in-plane electronic conduction and facilitates oxygen removal, with the benefit becoming especially important at low Ir loading. This means that the same catalyst loading can produce different apparent activity depending on whether the PTL enables utilization or leaves parts of the catalyst electronically or transport-wise underused. Inputs should therefore include impedance, bubble signal, temperature, pressure, water activity, PTL porosity, PTL thickness, MPL presence, membrane or ionomer environment, catalyst-layer thickness and compression. Outputs include utilization map, apparent kinetic loss, local transport penalty, local degradation risk and device-readiness score.

Task 4 is transferred validation under held-out operating boundaries. Milosevic et al. combined experiment and modeling to reveal Ir degradation pathways during intermittent PEM water electrolysis, showing that

degradation can be sequence-triggered rather than simply time- or charge-triggered (Figure 20c) [195]. Their work separates Ir dissolution, transport and deposition inside a zero-gap electrolyzer. Under intermittent protocols, dissolved Ir species do not merely leave the catalyst layer and disappear into the water line. Cationic Ir species can precipitate near the anode–membrane interface to form an Ir band, while potential cycling can promote back-transport of anionic Ir species toward the anode. Idle potential therefore changes the fate of dissolved Ir: it can alter whether Ir is lost to water, trapped in the membrane, deposited near the cathode, or returned toward the anode region. This is exactly the kind of history dependence that endpoint retention cannot encode. Validation must therefore hold out pH, electrolyte, waveform, current range, idle potential, cell type, membrane or ionomer environment and device format [196]. Random time-window splits from the same cell or electrode are not evidence of transfer because they share the same hidden transport and deposition history.

Beyond held-out protocols, the strongest validation of transferability is prospective device prediction, which tests whether a model can anticipate device-level behavior before experimental confirmation. Wang et al. identified predictors of MEA activity for Ir oxide catalysts, treating device activity as its own target rather than a half-cell ranking carried forward (Figure 20d) [197]. This is important because conventional descriptors did not transfer equally: BET surface area was essentially non-predictive, RDE activity translated only weakly to MEA activity, whereas composition and coordination-based descriptors such as bulk oxygen content, μ1/μ2 oxygen ratio and Ir^{3+}/Ir^{4+} ratio correlated strongly with MEA activity. The implication is not that half-cell testing is useless, but that MEA activity has its own descriptors because the catalyst operates inside a catalyst-layer/PTL/membrane environment. A transfer model should therefore combine material descriptors, condition histories and device geometry. The strongest test is to let the model choose a material–protocol pair, predict its trajectory under a defined MEA condition, and then check voltage, dissolution and post-test state under that same condition. Failure patterns are informative: transfer across pH but failure across waveform points to missing memory; transfer across half-cell protocols but failure in MEA points to unlabelled water, gas, ionomer, PTL, pressure or utilization fields [198]. Protocol optimization without state-sensitive measurements can identify a successful waveform but cannot reveal why it transfers. A transferable claim therefore requires the predicted transition, its uncertainty and its response to an independent intervention to be tested under a held-out material–protocol–device boundary.

Across the three learning problems, the practical workflow is therefore distributed across the corresponding physical tasks rather than treated as an algorithm-first recipe. Active-state formation fixes event definitions, labels, sample units and state-sensitive evidence (Section 2 and Table 1); mechanism–degradation coupling fixes target-matched model families, metrics and leakage controls (Section 3 and Table 2); and operating-boundary control fixes transfer and prospective tests across protocols and devices (Section 4). Table 3 consolidates this mapping from learning target to dynamic label, evidence channel, model family and validation test.

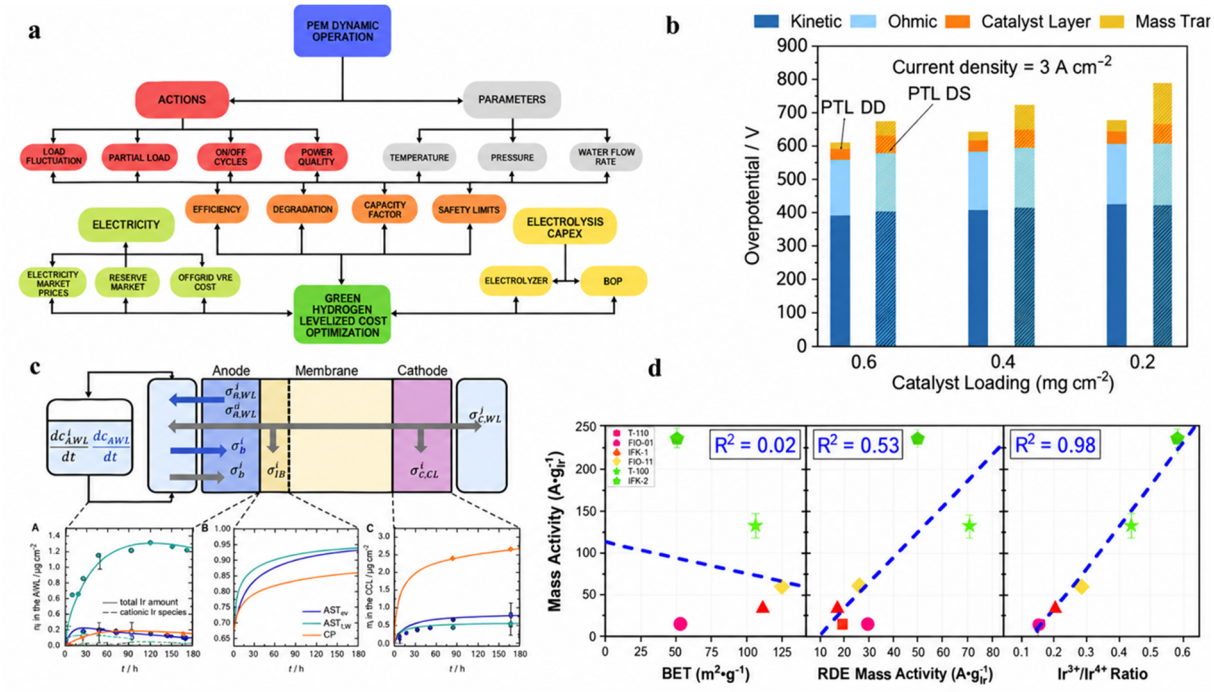


Figure 20. (**a**) Dynamic PEM electrolyzer operation couples renewable-power fluctuations with degradation, efficiency and safety constraints. Adapted with permission from Ref. [192]. Copyright 2024, Elsevier. (**b**) PTL-dependent overpotential breakdown at different anode catalyst loadings, showing that transport-layer architecture

strongly affects losses under low-Ir and high-current operation. Adapted with permission from Ref. [194]. Copyright 2025, Elsevier. (**c**) Experimental–modeling framework for Ir degradation during intermittent PEMWE operation. The internal subplots show (**A**) the time-dependent Ir amount in the anode water line (AWL), including the total Ir amount and the contribution of cationic Ir species; (**B**) the modeled probability of Ir deposition at the anode catalyst layer (ACL)–membrane interface; and (**C**) the time-dependent Ir amount deposited in the cathode catalyst layer (CCL). Adapted with permission from Ref. [195]. Copyright 2025, Elsevier. (**d**) MEA-targeted descriptor analysis for IrO_x catalysts, showing that device activity is predicted more reliably by coordination and oxidation-state descriptors than by BET surface area or RDE ranking. Adapted with permission from Ref. [197]. Copyright 2026, American Chemical Society.

Table 3. Whole-review supervised learning targets for dynamic OER ML.

learning Target	Dynamic Labels	Evidence Channels	Suitable Models	Validation
Active-state formation	onset, growth rate, active fraction, reversibility	XAS, Raman, ICP-MS, current transient	latent-state model, temporal GNN	early-to-late, out-of-protocol
Pathway redistribution	AEM/LOM/OPM weights, switching threshold	isotope DEMS, ATR-FTIR, Raman, XAS	mixture-of-experts, multitask learning	mechanism holdout
Degradation pathway	first failure node, dissolution flux, passivation probability	ICP-MS, microscopy, voltage drift	survival model, competing-risk model	pH/electrolyte/protocol holdout
Device transfer	MEA trajectory, utilization fraction, transfer score	MEA, impedance, pressure, PTL metadata	domain adaptation, physics-informed ML	RDE-to-MEA prospective test

5. Conclusions and Outlook

Looking forward, the main challenge is not simply to collect more time-resolved OER data, but to make catalyst trajectories comparable, reusable and transferable across laboratories and operating environments. Future datasets should therefore preserve the relation between precursor state, operating history, synchronized electrochemical and operando observations, and the subsequent working-state response. Failed activation, early dissolution, pathway instability and unsuccessful device transfer should be retained together with successful trajectories, because these negative histories define the boundaries within which a learned rule remains valid. Uncertainty, missing observations and calibration information should likewise be treated as part of the trajectory record rather than as secondary reporting details. Such datasets would provide a common basis for learning not only which catalysts perform well, but why nominally similar materials diverge under different operating histories.

A second priority is to move dynamic OER ML from retrospective correlation toward experimentally testable state laws. The useful prediction is not merely a fitted current or spectrum, but a forecast of when a working state will form, when a mechanism will redistribute, when a stability boundary will be crossed, and how these events respond to a controlled perturbation. This requires closer integration between ML and experiment: models should motivate measurements or perturbations that discriminate competing state trajectories, while operando measurements should determine whether the predicted transition actually occurs. In this sense, prospective experiments on unseen materials or operating histories are more informative than increasingly complex models evaluated only within previously sampled conditions. The long-term goal is a closed learning loop in which early and incomplete observations are sufficient to predict later catalyst behavior and to identify which intervention can redirect an unfavorable trajectory.

This perspective also changes the design objective of OER catalyst discovery. Rather than ranking materials independently of how they are activated and operated, future models should increasingly co-design the material, activation protocol and operating window. A catalyst that is optimal under steady half-cell testing may not remain optimal under intermittent load, different electrolyte reservoirs, high-current transport constraints or MEA integration. Dynamic ML should therefore learn which combinations of precursor chemistry and operating history preserve a productive working state, which conditions push the catalyst outside its mechanistic or stability window, and which device boundaries require adaptation of the learned rule. This creates a natural bridge from catalyst-level trajectory learning to protocol optimization and device-level control.

Ultimately, progress in dynamic OER ML should be judged by transfer rather than by the number of time-series models applied to operando data. A mature framework should be able to use an early observation of a previously unseen material–protocol pair to forecast its later working-state trajectory with calibrated uncertainty, identify the most probable failure or transition route, and predict whether a defined intervention will move the system toward a more durable operating state. Achieving this level of prospective and transferable prediction would transform operando measurements from isolated mechanistic demonstrations into reusable state knowledge for the joint optimization of catalysts, operating protocols and water-electrolysis devices (Figure 21).

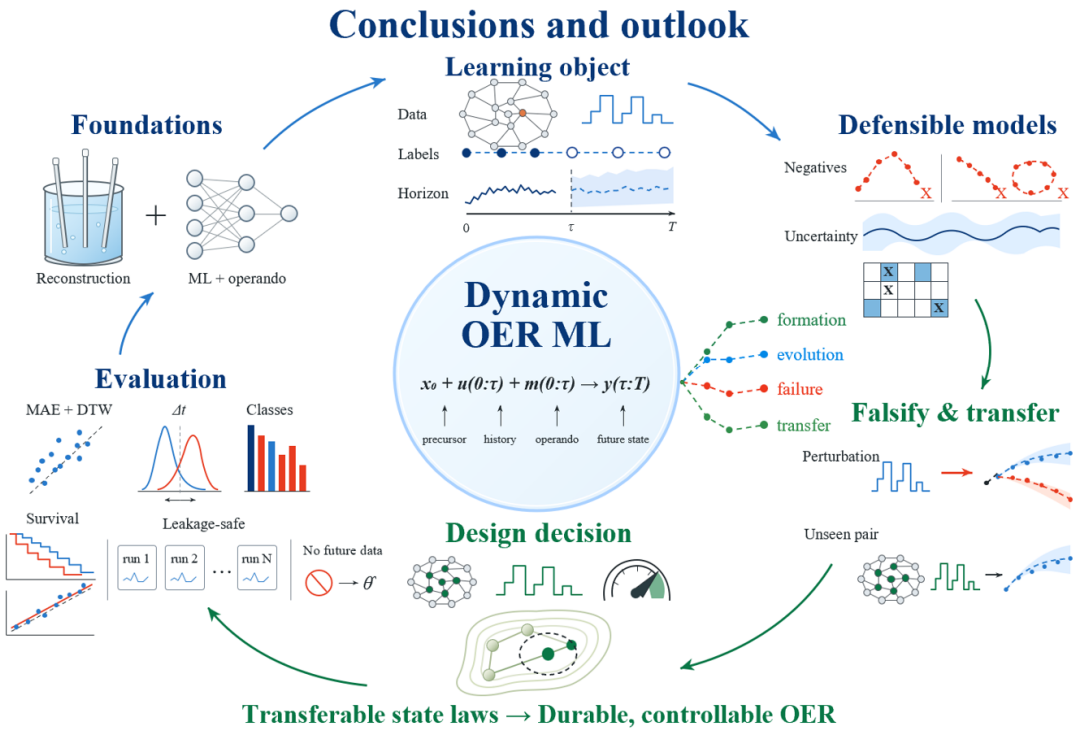


Figure 21. Conclusions and outlook for dynamic ML in OER catalysis. Precursor state, operating history and operando measurements are integrated to predict working-state formation, evolution, failure and transfer. The closed loop connects trajectory learning, leakage-safe evaluation, prospective testing and joint optimization of materials, protocols and operating windows.

Author Contributions

Z.Z. prepared the original draft. K.X. contributed to the literature collection. C.Z. and J.H. supervised the work and contributed to manuscript review and editing. All authors have read and agreed to the published version of the manuscript.

Funding

This work was supported by the National Natural Science Foundation of China (Grant No: 52364041), Natural Science Foundation of Yunnan Province (Grant No: 202401AV070011) and the Yunnan Talent Support Plan (Grant No: XDYC-YLXZ-2024-0003).

Institutional Review Board Statement

Not applicable.

Informed Consent Statement

Not applicable.

Data Availability Statement

Data availability is not applicable to this article as no new datasets were generated or analyzed during the current study.

Conflicts of Interest

The authors declare no conflict of interest.

Use of AI and AI-Assisted Technologies

During the preparation of this work, the authors used ChatGPT (OpenAI) to assist with figure modification. The scientific content, mechanistic interpretation, conceptual design, and annotations of these figures were

determined by the authors. After using the AI-assisted tool, the authors carefully reviewed, corrected, and verified all relevant content and take full responsibility for the published article.

References

1. Yang, X.; Nielsen, C.P.; Song, S.; et al. Breaking the hard-to-abate bottleneck in China's path to carbon neutrality with clean hydrogen. *Nat. Energy* **2022**, *7*, 955–965. https://doi.org/10.1038/s41560-022-01114-6.
2. Terlouw, T.; Moretti, C.; Harpprecht, C.; et al. Global greenhouse gas emissions mitigation potential of existing and planned hydrogen projects. *Nat. Energy* **2025**, *10*, 1503–1515. https://doi.org/10.1038/s41560-025-01892-9.
3. Algers, J.; Åhman, M.; Nilsson, L.J. Steel decarbonization—From optimization to transformation. *Annu. Rev. Environ. Resour.* **2025**, *50*, 433–454. https://doi.org/10.1146/annurev-environ-111523-101851.
4. Canat, A.N.; Özkan, C. Supplying hydrogen for green steel through renewable energy sources: A case study of Türkiye. *J. Clean. Prod.* **2024**, *450*, 141961. https://doi.org/10.1016/j.jclepro.2024.141961.
5. Ye, D.; Tsang, S.C.E. Prospects and challenges of green ammonia synthesis. *Nat. Synth.* **2023**, *2*, 612–623. https://doi.org/10.1038/s44160-023-00321-7.
6. Ren, J.T.; Chen, L.; Wang, H.Y.; et al. Water electrolysis for hydrogen production: From hybrid systems to self-powered/catalyzed devices. *Energy Environ. Sci.* **2024**, *17*, 49–113. https://doi.org/10.1039/d3ee02467a.
7. Shih, A.J.; Monteiro, M.C.O.; Dattila, F.; et al. Water electrolysis. *Nat. Rev. Methods Primers* **2022**, *2*, 84. https://doi.org/10.1038/s43586-022-00164-0.
8. Gao, X.; Chen, Y.; Wang, Y.; et al. Next-generation green hydrogen: Progress and perspective from electricity, catalyst to electrolyte in electrocatalytic water splitting. *Nano-Micro Lett.* **2024**, *16*, 237. https://doi.org/10.1007/s40820-024-01424-2.
9. Seh, Z.W.; Kibsgaard, J.; Dickens, C.F.; et al. Combining theory and experiment in electrocatalysis: Insights into materials design. *Science* **2017**, *355*, eaad4998. https://doi.org/10.1126/science.aad4998.
10. Suntivich, J.; May, K.J.; Gasteiger, H.A.; et al. A perovskite oxide optimized for oxygen evolution catalysis from molecular orbital principles. *Science* **2011**, *334*, 1383–1385. https://doi.org/10.1126/science.1212858.
11. Wu, L.; Guo, T.; Li, T. Machine learning-accelerated prediction of overpotential of oxygen evolution reaction of single-atom catalysts. *iScience* **2021**, *24*, 102398. https://doi.org/10.1016/j.isci.2021.102398.
12. Li, Z.; Achenie, L.E.K.; Xin, H. An adaptive machine learning strategy for accelerating discovery of perovskite electrocatalysts. *ACS Catal.* **2020**, *10*, 4377–4384. https://doi.org/10.1021/acscatal.9b05248.
13. Mao, X.; Wang, L.; Li, Y. Machine-learning-assisted discovery of high-efficient oxygen evolution electrocatalysts. *J. Phys. Chem. Lett.* **2023**, *14*, 170–177. https://doi.org/10.1021/acs.jpclett.2c02873.
14. Esterhuizen, J.A.; Goldsmith, B.R.; Linic, S. Interpretable machine learning for knowledge generation in heterogeneous catalysis. *Nat. Catal.* **2022**, *5*, 175–184. https://doi.org/10.1038/s41929-022-00744-z.
15. Mai, H.; Le, T.C.; Chen, D.; et al. Machine learning for electrocatalyst and photocatalyst design and discovery. *Chem. Rev.* **2022**, *122*, 13478–13515. https://doi.org/10.1021/acs.chemrev.2c00061.
16. Bergmann, A.; Martinez-Moreno, E.; Teschner, D.; et al. Reversible amorphization and the catalytically active state of crystalline Co_3O_4 during oxygen evolution. *Nat. Commun.* **2015**, *6*, 8625. https://doi.org/10.1038/ncomms9625.
17. Fabbri, E.; Nachtegaal, M.; Binninger, T.; et al. Dynamic surface self-reconstruction is the key of highly active perovskite nano-electrocatalysts for water splitting. *Nat. Mater.* **2017**, *16*, 925–931. https://doi.org/10.1038/nmat4938.
18. Dionigi, F.; Zeng, Z.; Sinev, I.; et al. In-situ structure and catalytic mechanism of NiFe and CoFe layered double hydroxides during oxygen evolution. *Nat. Commun.* **2020**, *11*, 2522. https://doi.org/10.1038/s41467-020-16237-1.
19. Mefford, J.T.; Akbashev, A.R.; Kang, M.; et al. Correlative operando microscopy of oxygen evolution electrocatalysts. *Nature* **2021**, *593*, 67–73. https://doi.org/10.1038/s41586-021-03454-x.
20. Mefford, J.T.; Rong, X.; Abakumov, A.M.; et al. Water electrolysis on $La_{1-x}Sr_xCoO_{3-\delta}$ perovskite electrocatalysts. *Nat. Commun.* **2016**, *7*, 11053. https://doi.org/10.1038/ncomms11053.
21. Geiger, S.; Kasian, O.; Ledendecker, M.; et al. The stability number as a metric for electrocatalyst stability benchmarking. *Nat. Catal.* **2018**, *1*, 508–515. https://doi.org/10.1038/s41929-018-0085-6.
22. Su, H.; Zhou, W.; Zhou, W.; et al. *In Situ* spectroscopic observation of dynamic-coupling oxygen on atomically dispersed iridium electrocatalyst for acidic water oxidation. *Nat. Commun.* **2021**, *12*, 6118. https://doi.org/10.1038/s41467-021-26416-3.
23. Jin, X.; Lee, T.; Park, J.; et al. pH-dependent mechanism of oxygen evolution in highly disordered RuO2 nanosheets. *Nat. Commun.* **2026**, *17*, 672. https://doi.org/10.1038/s41467-025-67318-y.
24. Gao, L.; Cui, X.; Sewell, C.D.; et al. Recent advances in activating surface reconstruction for the high-efficiency oxygen evolution reaction. *Chem. Soc. Rev.* **2021**, *50*, 8428–8469. https://doi.org/10.1039/d0cs00962h.

25. Zhao, Y.; Adiyeri Saseendran, D.P.; Huang, C.; et al. Oxygen Evolution/Reduction Reaction Catalysts: From *In Situ* Monitoring and Reaction Mechanisms to Rational Design. *Chem. Rev.* **2023**, *123*, 6257–6358. https://doi.org/10.1021/acs.chemrev.2c00515.
26. Benavides-Hernández, J.; Dumeignil, F. From characterization to discovery: Artificial intelligence, machine learning and high-throughput experiments for heterogeneous catalyst design. *ACS Catal.* **2024**, *14*, 11749–11779. https://doi.org/10.1021/acscatal.3c06293.
27. Ding, R.; Chen, J.; Chen, Y.; et al. Unlocking the potential: Machine learning applications in electrocatalyst design for electrochemical hydrogen energy transformation. *Chem. Soc. Rev.* **2024**, *53*, 11390–11461. https://doi.org/10.1039/d4cs00844h.
28. Hu, J.; Guo, T.; Zhong, X.; et al. In Situ Reconstruction of High-Entropy Heterostructure Catalysts for Stable Oxygen Evolution Electrocatalysis under Industrial Conditions. *Adv. Mater.* **2024**, *36*, 2310918. https://doi.org/10.1002/adma.202310918.
29. Mei, Y.; Feng, Y.; Zhang, C.; et al. High-entropy alloy with Mo-coordination as efficient electrocatalyst for oxygen evolution reaction. *ACS Catal.* **2022**, *12*, 10808–10817. https://doi.org/10.1021/acscatal.2c02604.
30. Zhang, C.; Qi, Q.; Mei, Y.; et al. Rationally reconstructed metal–organic frameworks as robust oxygen evolution electrocatalysts. *Adv. Mater.* **2023**, *35*, 2208904. https://doi.org/10.1002/adma.202208904.
31. Wang, Y.; Tao, S.; Lin, H.; et al. Atomically targeting NiFe LDH to create multivacancies for OER catalysis with a small organic anchor. *Nano Energy* **2021**, *81*, 105606. https://doi.org/10.1016/j.nanoen.2020.105606.
32. Qi, Q.; Zhang, C.; Hu, J. Triggered factors and structure-activity relationship in the dynamic reconstruction processing of MOF for the alkaline oxygen evolution reaction. *Coord. Chem. Rev.* **2025**, *522*, 216235. https://doi.org/10.1016/j.ccr.2024.216235.
33. Qi, Q.; Zhang, Y.; Zhang, C.; et al. Halogen-modified iron-based metal–organic frameworks for remarkably improved electrocatalytic oxygen evolution. *J. Phys. Chem. C* **2024**, *128*, 1936–1945. https://doi.org/10.1021/acs.jpcc.3c06800.
34. Gong, M.; Dai, H. A mini review of NiFe-based materials as highly active oxygen evolution reaction electrocatalysts. *Nano Res.* **2015**, *8*, 23–39. https://doi.org/10.1007/s12274-014-0591-z.
35. McCrory, C.C.L.; Jung, S.; Ferrer, I.M.; et al. Benchmarking hydrogen evolving reaction and oxygen evolving reaction electrocatalysts for solar water splitting devices. *J. Am. Chem. Soc.* **2015**, *137*, 4347–4357. https://doi.org/10.1021/ja510442p.
36. Anantharaj, S.; Ede, S.R.; Sakthikumar, K.; et al. Recent trends and perspectives in electrochemical water splitting with an emphasis on sulfide, selenide, and phosphide catalysts of Fe, Co, and Ni: A review. *ACS Catal.* **2016**, *6*, 8069–8097. https://doi.org/10.1021/acscatal.6b02479.
37. Over, H. Surface chemistry of ruthenium dioxide in heterogeneous catalysis and electrocatalysis: From fundamental to applied research. *Chem. Rev.* **2012**, *112*, 3356–3426. https://doi.org/10.1021/cr200247n.
38. Yu, S.; Zhang, Y.; Zhang, C.; et al. Stability regulation of metal–organic framework materials for electrocatalysis. *J. Mater. Chem. A* **2025**, *13*, 4814–4837. https://doi.org/10.1039/d4ta08090d.
39. Yuan, J.; Qi, Q.; Wan, Q.; et al. Tungsten regulated medium-entropy heterostructure as a highly efficient electrocatalyst for oxygen evolution reaction. *Dalton Trans.* **2025**, *54*, 5293–5300. https://doi.org/10.1039/d5dt00258c.
40. Yeo, B.S.; Bell, A.T. Enhanced activity of gold-supported cobalt oxide for the electrochemical evolution of oxygen. *J. Am. Chem. Soc.* **2011**, *133*, 5587–5593. https://doi.org/10.1021/ja200559j.
41. Louie, M.W.; Bell, A.T. An investigation of thin-film Ni–Fe oxide catalysts for the electrochemical evolution of oxygen. *J. Am. Chem. Soc.* **2013**, *135*, 12329–12337. https://doi.org/10.1021/ja405351s.
42. Han, F.; Andrejevic, N.; Li, M. A hidden dimension to explore new thermoelectrics. *Joule* **2018**, *2*, 16–18. https://doi.org/10.1016/j.joule.2017.12.014.
43. Giordano, L.; Han, B.; Risch, M.; et al. pH dependence of OER activity of oxides: Current and future perspectives. *Catal. Today* **2016**, *262*, 2–10. https://doi.org/10.1016/j.cattod.2015.10.006.
44. Wang, Z.; Zhang, C.; Zhang, Y.; et al. Ultrasound-assisted synthesis of high-entropy materials for enhanced oxygen evolution electrocatalysis. *Metals* **2024**, *14*, 384. https://doi.org/10.3390/met14040384.
45. Zhu, Y.; Zhou, W.; Shao, Z. Perovskite/carbon composites: Applications in oxygen electrocatalysis. *Small* **2017**, *13*, 1603793. https://doi.org/10.1002/smll.201603793.
46. Jain, A.; Ong, S.P.; Hautier, G.; et al. Commentary: The materials project: A materials genome approach to accelerating materials innovation. *APL Mater.* **2013**, *1*, 011002. https://doi.org/10.1063/1.4812323.
47. Butler, K.T.; Davies, D.W.; Cartwright, H.; et al. Machine learning for molecular and materials science. *Nature* **2018**, *559*, 547–555. https://doi.org/10.1038/s41586-018-0337-2.
48. Ward, L.; Agrawal, A.; Choudhary, A.; et al. A general-purpose machine learning framework for predicting properties of inorganic materials. *npj Comput. Mater.* **2016**, *2*, 16028. https://doi.org/10.1038/npjcompumats.2016.28.
49. Chen, C.; Ye, W.; Zuo, Y.; et al. Graph networks as a universal machine learning framework for molecules and crystals. *Chem. Mater.* **2019**, *31*, 3564–3572. https://doi.org/10.1021/acs.chemmater.9b01294.
50. Schmidt, J.; Marques, M.R.G.; Botti, S.; et al. Recent advances and applications of machine learning in solid-state materials science. *npj Comput. Mater.* **2019**, *5*, 83. https://doi.org/10.1038/s41524-019-0221-0.
51. Trotochaud, L.; Young, S.L.; Ranney, J.K.; et al. Nickel–iron oxyhydroxide oxygen-evolution electrocatalysts: The role of intentional and incidental iron incorporation. *J. Am. Chem. Soc.* **2014**, *136*, 6744–6753. https://doi.org/10.1021/ja502379c.

52. Friebel, D.; Louie, M.W.; Bajdich, M.; et al. Identification of highly active Fe sites in (Ni,Fe)OOH for electrocatalytic water splitting. *J. Am. Chem. Soc.* **2015**, *137*, 1305–1313. https://doi.org/10.1021/ja511559d.
53. Wang, H.Y.; Hung, S.F.; Chen, H.Y.; et al. In Operando Identification of Geometrical-Site-Dependent Water Oxidation Activity of Spinel Co_3O_4. *J. Am. Chem. Soc.* **2016**, *138*, 36–39. https://doi.org/10.1021/jacs.5b10525.
54. Zhou, J.; Wang, Y.; Su, X.; et al. Electrochemically accessing ultrathin Co (oxy)hydroxide nanosheets and operando identifying their active phase for the oxygen evolution reaction. *Energy Environ. Sci.* **2019**, *12*, 739–746. https://doi.org/10.1039/c8ee03208d.
55. Kanan, M.W.; Nocera, D.G. In Situ Formation of an Oxygen-Evolving Catalyst in Neutral Water Containing Phosphate and Co^{2+}. *Science* **2008**, *321*, 1072–1075. https://doi.org/10.1126/science.1162018.
56. Chen, D.; Zhang, Y.; Feng, Y.; et al. Investigation into the stability of monometallic metal oxide electrocatalysts for hydrogen peroxide synthesis through the oxygen reduction reaction. *J. Mater. Chem. A* **2025**, *13*, 19105–19131. https://doi.org/10.1039/d5ta02600h.
57. Qin, M.; Chen, J.; Zheng, X.; et al. Operando deciphering the activity origins for potential-induced reconstructed oxygen-evolving catalysts. *Appl. Catal. B Environ.* **2022**, *316*, 121602. https://doi.org/10.1016/j.apcatb.2022.121602.
58. Choudhary, K.; Garrity, K.F.; Reid, A.C.E.; et al. The joint automated repository for various integrated simulations (JARVIS) for data-driven materials design. *npj Comput. Mater.* **2020**, *6*, 173. https://doi.org/10.1038/s41524-020-00440-1.
59. Behler, J.; Parrinello, M. Generalized neural-network representation of high-dimensional potential-energy surfaces. *Phys. Rev. Lett.* **2007**, *98*, 146401. https://doi.org/10.1103/physrevlett.98.146401.
60. Schütt, K.T.; Sauceda, H.E.; Kindermans, P.J.; et al. SchNet—A deep learning architecture for molecules and materials. *J. Chem. Phys.* **2018**, *148*, 241722. https://doi.org/10.1063/1.5019779.
61. Seitz, L.C.; Dickens, C.F.; Nishio, K.; et al. A highly active and stable $IrO_x/SrIrO_3$ catalyst for the oxygen evolution reaction. *Science* **2016**, *353*, 1011–1014. https://doi.org/10.1126/science.aaf5050.
62. Lopes, P.P.; Chung, D.Y.; Rui, X.; et al. Dynamically stable active sites from surface evolution of perovskite materials during the oxygen evolution reaction. *J. Am. Chem. Soc.* **2021**, *143*, 2741–2750. https://doi.org/10.1021/jacs.0c08959.
63. Wu, T.; Sun, S.; Song, J.; et al. Iron-facilitated dynamic active-site generation on spinel $CoAl_2O_4$ with self-termination of surface reconstruction for water oxidation. *Nat. Catal.* **2019**, *2*, 763–772. https://doi.org/10.1038/s41929-019-0325-4.
64. Qi, Q.; Tai, J.; Hu, J.; et al. Ligand Functionalized Iron-Based Metal-Organic Frameworks for Efficient Electrocatalytic Oxygen Evolution. *ChemCatChem* **2021**, *13*, 4976–4984. https://doi.org/10.1002/cctc.202101242.
65. Gong, J.; Qi, Q.; Wang, Z.; et al. Controlled reconstruction of metal–organic frameworks *via* coordination environment tuning as oxygen evolution electrocatalysts. *Dalton Trans.* **2025**, *54*, 2991–2999. https://doi.org/10.1039/d4dt03348e.
66. Nørskov, J.K.; Bligaard, T.; Rossmeisl, J.; et al. Towards the computational design of solid catalysts. *Nat. Chem.* **2009**, *1*, 37–46. https://doi.org/10.1038/nchem.121.
67. Ulissi, Z.W.; Tang, M.T.; Xiao, J.; et al. Machine-Learning Methods Enable Exhaustive Searches for Active Bimetallic Facets and Reveal Active Site Motifs for CO_2 Reduction. *ACS Catal.* **2017**, *7*, 6600–6608. https://doi.org/10.1021/acscatal.7b01648.
68. Toyao, T.; Maeno, Z.; Takakusagi, S.; et al. Machine learning for catalysis informatics: Recent applications and prospects. *ACS Catal.* **2020**, *10*, 2260–2297. https://doi.org/10.1021/acscatal.9b04186.
69. Liu, J.; Hu, Q.; Wang, Y.; et al. Achieving delafossite analog by *in situ* electrochemical self-reconstruction as an oxygen-evolving catalyst. *Proc. Natl. Acad. Sci. USA* **2020**, *117*, 21906–21913. https://doi.org/10.1073/pnas.2009180117.
70. Song, S.; Zhou, J.; Su, X.; et al. *Operando* X-ray spectroscopic tracking of self-reconstruction for anchored nanoparticles as high-performance electrocatalysts towards oxygen evolution. *Energy Environ. Sci.* **2018**, *11*, 2945–2953. https://doi.org/10.1039/c8ee00773j.
71. Kim, M.; Lee, B.; Ju, H.; et al. Reducing the Barrier Energy of Self-Reconstruction for Anchored Cobalt Nanoparticles as Highly Active Oxygen Evolution Electrocatalyst. *Adv. Mater.* **2019**, *31*, 1901977. https://doi.org/10.1002/adma.201901977.
72. Zhang, R.; Pan, L.; Guo, B.; et al. Tracking the Role of Defect Types in Co_3O_4 Structural Evolution and Active Motifs during Oxygen Evolution Reaction. *J. Am. Chem. Soc.* **2023**, *145*, 2271–2281. https://doi.org/10.1021/jacs.2c10515.
73. Huang, Z.F.; Song, J.; Du, Y.; et al. Chemical and structural origin of lattice oxygen oxidation in Co–Zn oxyhydroxide oxygen evolution electrocatalysts. *Nat. Energy* **2019**, *4*, 329–338. https://doi.org/10.1038/s41560-019-0355-9.
74. Kim, J.; Yin, X.; Tsao, K.C.; et al. $Ca_2Mn_2O_5$ as Oxygen-Deficient Perovskite Electrocatalyst for Oxygen Evolution Reaction. *J. Am. Chem. Soc.* **2014**, *136*, 14646–14649. https://doi.org/10.1021/ja506254g.
75. Lee, Y.; Suntivich, J.; May, K.J.; et al. Synthesis and Activities of Rutile IrO_2 and RuO_2 Nanoparticles for Oxygen Evolution in Acid and Alkaline Solutions. *J. Phys. Chem. Lett.* **2012**, *3*, 399–404. https://doi.org/10.1021/jz2016507.
76. Hansen, H.A.; Viswanathan, V.; Nørskov, J.K. Unifying kinetic and thermodynamic analysis of 2 e– and 4 e– reduction of oxygen on metal surfaces. *J. Phys. Chem. C* **2014**, *118*, 6706–6718. https://doi.org/10.1021/jp4100608.
77. Haase, F.T.; Bergmann, A.; Jones, T.E.; et al. Size effects and active state formation of cobalt oxide nanoparticles during the oxygen evolution reaction. *Nat. Energy* **2022**, *7*, 765–773. https://doi.org/10.1038/s41560-022-01083-w.

78. Ledezma-Yanez, I.; Wallace, W.D.Z.; Sebastián-Pascual, P.; et al. Interfacial water reorganization as a pH-dependent descriptor of the hydrogen evolution rate on platinum electrodes. *Nat. Energy* **2017**, *2*, 17031. https://doi.org/10.1038/nenergy.2017.31.
79. Willets, K.A. Probing nanoscale interfaces with electrochemical surface-enhanced Raman scattering. *Curr. Opin. Electrochem.* **2019**, *13*, 18–24. https://doi.org/10.1016/j.coelec.2018.10.005.
80. Koper, M.T.M. Thermodynamic theory of multi-electron transfer reactions: Implications for electrocatalysis. *J. Electroanal. Chem.* **2011**, *660*, 254–260. https://doi.org/10.1016/j.jelechem.2010.10.004.
81. Timoshenko, J.; Roldan Cuenya, B. *In Situ*/*Operando* Electrocatalyst Characterization by X-ray Absorption Spectroscopy. *Chem. Rev.* **2021**, *121*, 882–961. https://doi.org/10.1021/acs.chemrev.0c00396.
82. Zagalskaya, A.; Alexandrov, V. Role of Defects in the Interplay between Adsorbate Evolving and Lattice Oxygen Mechanisms of the Oxygen Evolution Reaction in RuO_2 and IrO_2. *ACS Catal.* **2020**, *10*, 3650–3657. https://doi.org/10.1021/acscatal.9b05544.
83. Roy, C.; Sebok, B.; Scott, S.B.; et al. Impact of nanoparticle size and lattice oxygen on water oxidation on $NiFeO_xH_y$. *Nat. Catal.* **2018**, *1*, 820–829. https://doi.org/10.1038/s41929-018-0162-x.
84. Beall, C.E.; Fabbri, E.; Schmidt, T.J. Perovskite oxide based electrodes for the oxygen reduction and evolution reactions: The underlying mechanism. *ACS Catal.* **2021**, *11*, 3094–3114. https://doi.org/10.1021/acscatal.0c04473.
85. Carmo, M.; Fritz, D.L.; Mergel, J.; et al. A comprehensive review on PEM water electrolysis. *Int. J. Hydrogen Energy* **2013**, *38*, 4901–4934. https://doi.org/10.1016/j.ijhydene.2013.01.151.
86. Weiß, A.; Siebel, A.; Bernt, M.; et al. Impact of intermittent operation on lifetime and performance of a PEM water electrolyzer. *J. Electrochem. Soc.* **2019**, *166*, F487–F497. https://doi.org/10.1149/2.0421908jes.
87. Schuler, T.; Schmidt, T.J.; Büchi, F.N. Polymer electrolyte water electrolysis: Correlating performance and porous transport layer structure: Part II. Electrochemical performance analysis. *J. Electrochem. Soc.* **2019**, *166*, F555–F565. https://doi.org/10.1149/2.1241908jes.
88. Man, I.C.; Su, H.Y.; Calle-Vallejo, F.; et al. Universality in oxygen evolution electrocatalysis on oxide surfaces. *ChemCatChem* **2011**, *3*, 1159–1165. https://doi.org/10.1002/cctc.201000397.
89. Hong, W.T.; Welsch, R.E.; Shao-Horn, Y. Descriptors of Oxygen-Evolution Activity for Oxides: A Statistical Evaluation. *J. Phys. Chem. C* **2016**, *120*, 78–86. https://doi.org/10.1021/acs.jpcc.5b10071.
90. Burke, M.S.; Zou, S.; Enman, L.J.; et al. Revised oxygen evolution reaction activity trends for first-row transition-metal (oxy)hydroxides in alkaline media. *J. Phys. Chem. Lett.* **2015**, *6*, 3737–3742. https://doi.org/10.1021/acs.jpclett.5b01650.
91. Weng, B.; Song, Z.; Zhu, R.; et al. Simple descriptor derived from symbolic regression accelerating the discovery of new perovskite catalysts. *Nat. Commun.* **2020**, *11*, 3513. https://doi.org/10.1038/s41467-020-17263-9.
92. Back, S.; Tran, K.; Ulissi, Z.W. Toward a design of active oxygen evolution catalysts: Insights from automated density functional theory calculations and machine learning. *ACS Catal.* **2019**, *9*, 7651–7659. https://doi.org/10.1021/acscatal.9b02416.
93. Tran, R.; Lan, J.; Shuaibi, M.; et al. The Open Catalyst 2022 (OC22) dataset and challenges for oxide electrocatalysts. *ACS Catal.* **2023**, *13*, 3066–3084. https://doi.org/10.1021/acscatal.2c05426.
94. Flores, R.A.; Paolucci, C.; Winther, K.T.; et al. Active learning accelerated discovery of stable iridium oxide polymorphs for the oxygen evolution reaction. *Chem. Mater.* **2020**, *32*, 5854–5863. https://doi.org/10.1021/acs.chemmater.0c01894.
95. Bang, K.; Hong, D.; Park, Y.; et al. Machine learning-enabled exploration of the electrochemical stability of real-scale metallic nanoparticles. *Nat. Commun.* **2023**, *14*, 3004. https://doi.org/10.1038/s41467-023-38758-1.
96. Abed, J.; Heras-Domingo, J.; Sanspeur, R.Y.; et al. Pourbaix machine learning framework identifies acidic water oxidation catalysts exhibiting suppressed ruthenium dissolution. *J. Am. Chem. Soc.* **2024**, *146*, 15740–15750. https://doi.org/10.1021/jacs.4c01353.
97. Wexler, R.B.; Gautam, G.S.; Stechel, E.B.; et al. Factors governing oxygen vacancy formation in oxide perovskites. *J. Am. Chem. Soc.* **2021**, *143*, 13212–13227. https://doi.org/10.1021/jacs.1c05570.
98. Lunger, J.R.; Karaguesian, J.; Chun, H.; et al. Towards atom-level understanding of metal oxide catalysts for the oxygen evolution reaction with machine learning. *npj Comput. Mater.* **2024**, *10*, 80. https://doi.org/10.1038/s41524-024-01273-y.
99. Moon, J.; Beker, W.; Siek, M.; et al. Active learning guides discovery of a champion four-metal perovskite oxide for oxygen evolution electrocatalysis. *Nat. Mater.* **2024**, *23*, 108–115. https://doi.org/10.1038/s41563-023-01707-w.
100. Mints, V.A.; Svane, K.L.; Rossmeisl, J.; et al. Exploring the high-entropy oxide composition space: Insights through comparing experimental with theoretical models for the oxygen evolution reaction. *ACS Catal.* **2024**, *14*, 6936–6944. https://doi.org/10.1021/acscatal.3c05915.
101. Jiang, C.; He, H.; Guo, H.; et al. Transfer learning guided discovery of efficient perovskite oxide for alkaline water oxidation. *Nat. Commun.* **2024**, *15*, 6301. https://doi.org/10.1038/s41467-024-50605-5.
102. Jenewein, K.J.; Torresi, L.; Haghmoradi, N.; et al. Navigating the unknown with AI: Multiobjective Bayesian optimization of non-noble acidic OER catalysts. *J. Mater. Chem. A* **2024**, *12*, 3072–3083. https://doi.org/10.1039/d3ta06651g.

103. Zhang, Q.; Xiao, W.; Fu, H.C.; et al. Unraveling the mechanism of self-repair of NiFe-based electrocatalysts by dynamic exchange of iron during the oxygen evolution reaction. *ACS Catal.* **2023**, *13*, 14975–14986. https://doi.org/10.1021/acscatal.3c03804.
104. Xu, S.; Chen, Z.; Qin, M.; et al. Developing new electrocatalysts for oxygen evolution reaction via high throughput experiments and artificial intelligence. *npj Comput. Mater.* **2024**, *10*, 194. https://doi.org/10.1038/s41524-024-01386-4.
105. Kodera, M.; Sayama, K. An automatic robot system for machine learning–assisted high-throughput screening of composite electrocatalysts. *Digit. Discov.* **2023**, *2*, 1683–1687. https://doi.org/10.1039/d3dd00116d.
106. Tabor, D.P.; Roch, L.M.; Saikin, S.K.; et al. Accelerating the discovery of materials for clean energy in the era of smart automation. *Nat. Rev. Mater.* **2018**, *3*, 5–20. https://doi.org/10.1038/s41578-018-0005-z.
107. Haase, F.T.; Rabe, A.; Schmidt, F.P.; et al. Role of Nanoscale Inhomogeneities in Co_2FeO_4 Catalysts during the Oxygen Evolution Reaction. *J. Am. Chem. Soc.* **2022**, *144*, 12007–12019. https://doi.org/10.1021/jacs.2c00850.
108. Ding, R.; Liu, J.; Hua, K.; et al. Leveraging data mining, active learning, and domain adaptation for efficient discovery of advanced oxygen evolution electrocatalysts. *Sci. Adv.* **2025**, *11*, eadr9038. https://doi.org/10.1126/sciadv.adr9038.
109. Qian, H.; Wei, J.; Yu, C.; et al. *In Situ* quantification of the active sites, turnover frequency, and stability of Ni–Fe (oxy)hydroxides for the oxygen evolution reaction. *ACS Catal.* **2022**, *12*, 14280–14289. https://doi.org/10.1021/acscatal.2c03898.
110. Diklić, N.; Clark, A.H.; Herranz, J.; et al. Potential Pitfalls in the *Operando* XAS Study of Oxygen Evolution Electrocatalysts. *ACS Energy Lett.* **2022**, *7*, 1735–1740. https://doi.org/10.1021/acsenergylett.2c00727.
111. Wu, D.; Hu, L.; Liu, X.; et al. Time-resolved spectroscopy uncovers deprotonation-induced reconstruction in oxygen-evolution NiFe-based (oxy)hydroxides. *Nat. Commun.* **2025**, *16*, 726. https://doi.org/10.1038/s41467-025-56070-y.
112. Yang, F.; Lopez Luna, M.; Haase, F.T.; et al. Spatially and chemically resolved visualization of Fe incorporation into NiO octahedra during the oxygen evolution reaction. *J. Am. Chem. Soc.* **2023**, *145*, 21465–21474. https://doi.org/10.1021/jacs.3c07158.
113. Görlin, M.; Chernev, P.; Ferreira de Araújo, J.; et al. Oxygen evolution reaction dynamics, faradaic charge efficiency, and the active metal redox states of Ni–Fe oxide water splitting electrocatalysts. *J. Am. Chem. Soc.* **2016**, *138*, 5603–5614. https://doi.org/10.1021/jacs.6b00332.
114. Batzner, S.; Musaelian, A.; Sun, L.; et al. E(3)-equivariant graph neural networks for data-efficient and accurate interatomic potentials. *Nat. Commun.* **2022**, *13*, 2453. https://doi.org/10.1038/s41467-022-29939-5.
115. Lookman, T.; Balachandran, P.V.; Xue, D.; et al. Active learning in materials science with emphasis on adaptive sampling using uncertainties for targeted design. *npj Comput. Mater.* **2019**, *5*, 21. https://doi.org/10.1038/s41524-019-0153-8.
116. Raccuglia, P.; Elbert, K.C.; Adler, P.D.F.; et al. Machine-learning-assisted materials discovery using failed experiments. *Nature* **2016**, *533*, 73–76. https://doi.org/10.1038/nature17439.
117. Raissi, M.; Perdikaris, P.; Karniadakis, G.E. Physics-informed neural networks: A deep learning framework for solving forward and inverse problems involving nonlinear partial differential equations. *J. Comput. Phys.* **2019**, *378*, 686–707. https://doi.org/10.1016/j.jcp.2018.10.045.
118. Shimakawa, H.; Kumada, A.; Sato, M. Prevention of leakage in machine learning prediction for polymer composite properties. *J. Chem. Inf. Model.* **2024**, *64*, 3621–3629. https://doi.org/10.1021/acs.jcim.3c01894.
119. Witman, M.D.; Schindler, P. MatFold: Systematic insights into materials discovery models' performance through standardized cross-validation protocols. *Digit. Discov.* **2025**, *4*, 625–635. https://doi.org/10.1039/d4dd00250d.
120. Kapoor, S.; Narayanan, A. Leakage and the reproducibility crisis in machine-learning-based science. *Patterns* **2023**, *4*, 100804. https://doi.org/10.1016/j.patter.2023.100804.
121. Kapoor, S.; Cantrell, E.M.; Peng, K.; et al. Reforms: Consensus-based recommendations for machine-learning-based science. *Sci. Adv.* **2024**, *10*, eadk3452. https://doi.org/10.1126/sciadv.adk3452.
122. Deka, N.; Jones, T.E.; Falling, L.J.; et al. On the operando structure of ruthenium oxides during the oxygen evolution reaction in acidic media. *ACS Catal.* **2023**, *13*, 7488–7498. https://doi.org/10.1021/acscatal.3c01607.
123. Liang, C.; Rao, R.R.; Svane, K.L.; et al. Unravelling the effects of active site density and energetics on the water oxidation activity of iridium oxides. *Nat. Catal.* **2024**, *7*, 763–775. https://doi.org/10.1038/s41929-024-01168-7.
124. Jia, H.; Yao, N.; Yu, C.; et al. Unveiling the electrolyte cations dependent kinetics on CoOOH-catalyzed oxygen evolution reaction. *Angew. Chem. Int. Ed.* **2023**, *62*, e202313886. https://doi.org/10.1002/anie.202313886.
125. Wang, Z.; Xiao, H. Fleeting-active-site-thrust oxygen evolution reaction by iron cations from the electrolyte. *J. Am. Chem. Soc.* **2024**, *146*, 29540–29550. https://doi.org/10.1021/jacs.4c09585.
126. Zhao, J.; Zhang, Y.; Ye, Y.; et al. Remote iron dynamics of NiFe (oxy)hydroxides toward robust active sites in water oxidation. *Nat. Commun.* **2025**, *16*, 5601. https://doi.org/10.1038/s41467-025-60728-y.
127. Choi, S.; Kim, S.J.; Han, S.; et al. Enhancing oxygen evolution reaction via a surface reconstruction-induced lattice oxygen mechanism. *ACS Catal.* **2024**, *14*, 15096–15107. https://doi.org/10.1021/acscatal.4c03594.
128. Ji, Q.; Tang, B.; Zhang, X.; et al. Operando identification of the oxide path mechanism with different dual-active sites for acidic water oxidation. *Nat. Commun.* **2024**, *15*, 8089. https://doi.org/10.1038/s41467-024-52471-7.

129. Wang, Z.; Goddard, W.A.; Xiao, H. Potential-dependent transition of reaction mechanisms for oxygen evolution on layered double hydroxides. *Nat. Commun.* **2023**, *14*, 4228. https://doi.org/10.1038/s41467-023-40011-8.
130. Li, W.; Zhang, J.; Yang, C.; et al. Modulating iridium coordination to control the oxygen evolution reaction pathway. *J. Am. Chem. Soc.* **2025**, *147*, 40697–40707. https://doi.org/10.1021/jacs.5c13365.
131. Ping, X.; Liu, Y.; Zheng, L.; et al. Locking the lattice oxygen in RuO_2 to stabilize highly active Ru sites in acidic water oxidation. *Nat. Commun.* **2024**, *15*, 2501. https://doi.org/10.1038/s41467-024-46815-6.
132. Wang, F.; Zou, P.; Zhang, Y.; et al. Activating lattice oxygen in high-entropy LDH for robust and durable water oxidation. *Nat. Commun.* **2023**, *14*, 6019. https://doi.org/10.1038/s41467-023-41706-8.
133. He, Z.; Zhang, J.; Gong, Z.; et al. Activating lattice oxygen in NiFe-based (oxy)hydroxide for water electrolysis. *Nat. Commun.* **2022**, *13*, 2191. https://doi.org/10.1038/s41467-022-29875-4.
134. Zhou, C.; Li, L.; Dong, Z.; et al. Pinning effect of lattice Pb suppressing lattice oxygen reactivity of Pb-RuO_2 enables stable industrial-level electrolysis. *Nat. Commun.* **2024**, *15*, 9774. https://doi.org/10.1038/s41467-024-53905-y.
135. Kasian, O.; Geiger, S.; Li, T.; et al. Degradation of iridium oxides *via* oxygen evolution from the lattice: Correlating atomic scale structure with reaction mechanisms. *Energy Environ. Sci.* **2019**, *12*, 3548–3555. https://doi.org/10.1039/c9ee01872g.
136. Xu, J.; Jin, H.; Lu, T.; et al. $IrO_x \cdot nH_2O$ with lattice water–assisted oxygen exchange for high-performance proton exchange membrane water electrolyzers. *Sci. Adv.* **2023**, *9*, eadh1718. https://doi.org/10.1126/sciadv.adh1718.
137. Qu, M.R.; Liu, H.; Feng, S.H.; et al. Temperature-dependent mechanism evolution on $RhRu_3O_x$ for acidic water oxidation. *Nat. Commun.* **2025**, *16*, 9261. https://doi.org/10.1038/s41467-025-64286-1.
138. Liu, H.; Zhou, Q.; Yu, J.; et al. Lattice oxygen refilling for stable acidic water oxidation. *ACS Catal.* **2025**, *15*, 8511–8521. https://doi.org/10.1021/acscatal.5c01382.
139. He, B.; Hosseini, P.; Priamushko, T.; et al. Atomic-scale insights into surface reconstruction and transformation in Co–Cr spinel oxides during the oxygen evolution reaction. *Nat. Commun.* **2025**, *16*, 9895. https://doi.org/10.1038/s41467-025-65626-x.
140. Qian, F.; Cao, D.; Chen, S.; et al. High-entropy RuO_2 catalyst with dual-site oxide path for durable acidic oxygen evolution reaction. *Nat. Commun.* **2025**, *16*, 6894. https://doi.org/10.1038/s41467-025-61763-5.
141. Liang, X.; Yan, W.; Yu, Y.; et al. Electrocatalytic Water Oxidation Activity-Stability Maps for Perovskite Oxides Containing 3*d*, 4*d* and 5*d* Transition Metals. *Angew. Chem. Int. Ed.* **2023**, *62*, e202311606. https://doi.org/10.1002/anie.202311606.
142. Zheng, W.; Zhao, Y.; Jiang, K.; et al. Heteroatom dopants overcome the activity-stability trade-off in RuO_2 for acidic oxygen evolution. *Nat. Commun.* **2025**, *16*, 6716. https://doi.org/10.1038/s41467-025-62036-x.
143. Kim, J.; Kwon, I.S.; Lim, J.; et al. Machine-learning-guided tungsten single atoms promote oxyhydroxides for noble-metal-free water electrolysis. *Nat. Commun.* **2026**, *17*, 2344. https://doi.org/10.1038/s41467-026-68735-3.
144. Wan, Z.; Wang, Q.D.; Liu, D.; et al. Data-driven machine learning model for the prediction of oxygen vacancy formation energy of metal oxide materials. *Phys. Chem. Chem. Phys.* **2021**, *23*, 15675–15684. https://doi.org/10.1039/d1cp02066h.
145. Park, S.; Lee, N.; Park, J.O.; et al. Exploring the latent chemical space of oxygen vacancy formation energy by a machine learning ensemble. *ACS Mater. Lett.* **2024**, *6*, 66–72. https://doi.org/10.1021/acsmaterialslett.3c00636.
146. Li, L.; Zhang, G.; Zhou, C.; et al. Lanthanide-regulating Ru-O covalency optimizes acidic oxygen evolution electrocatalysis. *Nat. Commun.* **2024**, *15*, 4974. https://doi.org/10.1038/s41467-024-49281-2.
147. Pandya, R.; Dorchies, F.; Romanin, D.; et al. Concurrent oxygen evolution reaction pathways revealed by high-speed compressive Raman imaging. *Nat. Commun.* **2024**, *15*, 8362. https://doi.org/10.1038/s41467-024-52536-7.
148. Usama, M.; Razzaq, S.; Hättig, C.; et al. Oxygen evolution reaction on IrO_2(110) is governed by Walden-type mechanisms. *Nat. Commun.* **2025**, *16*, 6137. https://doi.org/10.1038/s41467-025-61367-z.
149. van der Merwe, M.; Lee, Y.; Wibowo, R.E.; et al. Unravelling the mechanistic complexity of the oxygen evolution reaction and Ir dissolution in highly dimensional amorphous hydrous iridium oxides. *Energy Environ. Sci.* **2025**, *18*, 1214–1231. https://doi.org/10.1039/d4ee02839b.
150. Wang, H.; Lin, C.; Tan, L.; et al. Atomic Ga triggers spatiotemporal coordination of oxygen radicals for efficient water oxidation on crystalline RuO_2. *Nat. Commun.* **2025**, *16*, 3976. https://doi.org/10.1038/s41467-025-58346-9.
151. Luo, X.; Zhao, H.; Tan, X.; et al. Fe-s dually modulated adsorbate evolution and lattice oxygen compatible mechanism for water oxidation. *Nat. Commun.* **2024**, *15*, 8293. https://doi.org/10.1038/s41467-024-52682-y.
152. Zhang, K.; Liang, X.; Wang, Y.; et al. Support-tuned iridium reconstruction with crystalline phase dominating acidic oxygen evolution. *Nat. Commun.* **2025**, *16*, 8164. https://doi.org/10.1038/s41467-025-63541-9.
153. Liu, S.; Sun, M.; Dai, L.; et al. Defect-interface coupling for stable lattice-oxygen-driven oxygen evolution at industrial current densities. *Nat. Commun.* **2026**, *17*, 2135. https://doi.org/10.1038/s41467-026-68730-8.
154. Wu, H.; Chang, J.; Yu, J.; et al. Atomically engineered interfaces inducing bridging oxygen-mediated deprotonation for enhanced oxygen evolution in acidic conditions. *Nat. Commun.* **2024**, *15*, 10315. https://doi.org/10.1038/s41467-024-54798-7.
155. Cao, X.; Miao, L.; Jia, W.; et al. Strain heterogeneity in RuO_2 for efficient acidic oxygen evolution reaction in proton exchange membrane water electrolysis. *Nat. Commun.* **2025**, *16*, 6217. https://doi.org/10.1038/s41467-025-58570-3.

156. Zhou, L.; Yang, M.; Liu, Y.; et al. Intrinsic metal-support interactions break the activity-stability dilemma in electrocatalysis. *Nat. Commun.* **2025**, *16*, 8739. https://doi.org/10.1038/s41467-025-63397-z.
157. Kaufman, S.; Rosset, S.; Perlich, C.; et al. Leakage in data mining: Formulation, detection, and avoidance. *ACM Trans. Knowl. Discov. Data* **2012**, *6*, 1–21. https://doi.org/10.1145/2382577.2382579.
158. Roberts, M.; Driggs, D.; Thorpe, M.; et al. Common pitfalls and recommendations for using machine learning to detect and prognosticate for COVID-19 using chest radiographs and CT scans. *Nat. Mach. Intell.* **2021**, *3*, 199–217. https://doi.org/10.1038/s42256-021-00307-0.
159. Huang, J.; Clark, A.H.; Hales, N.; et al. Oxidation of interfacial cobalt controls the pH dependence of the oxygen evolution reaction. *Nat. Chem.* **2025**, *17*, 856–864. https://doi.org/10.1038/s41557-025-01784-1.
160. Liang, C.; Katayama, Y.; Tao, Y.; et al. Role of electrolyte pH on water oxidation for iridium oxides. *J. Am. Chem. Soc.* **2024**, *146*, 8928–8938. https://doi.org/10.1021/jacs.3c12011.
161. Wei, C.; Wang, Z.; Otani, K.; et al. Benchmarking electrocatalyst stability for acidic oxygen evolution reaction: The crucial role of dissolved ion concentration. *ACS Catal.* **2023**, *13*, 14058–14069. https://doi.org/10.1021/acscatal.3c03257.
162. van der Heijden, O.; Eggebeen, J.J.J.; Trzesniowski, H.; et al. Li^+ Cations Activate NiFeOOH for Oxygen Evolution in Sodium and Potassium Hydroxide. *Angew. Chem. Int. Ed.* **2024**, *63*, e202318692. https://doi.org/10.1002/anie.202318692.
163. Chen, B.; Wang, P.; Shin, D.; et al. Effect of electrolyte ions on iridium oxide-based water oxidation catalysis. *ACS Catal.* **2025**, *15*, 16476–16482. https://doi.org/10.1021/acscatal.5c03970.
164. Zhu, S.; Yang, R.; Li, H.J.W.; et al. Reconstructing hydrogen-bond network for efficient acidic oxygen evolution. *Angew. Chem. Int. Ed*. **2024**, *63*, e202319462. https://doi.org/10.1002/anie.202319462.
165. Endrődi, B.; Trapp, C.A.; Szén, I.; et al. Challenges and opportunities of the dynamic operation of PEM water electrolyzers. *Energies* **2025**, *18*, 2154. https://doi.org/10.3390/en18092154.
166. Papakonstantinou, G.; Algara-Siller, G.; Teschner, D.; et al. Degradation study of a proton exchange membrane water electrolyzer under dynamic operation conditions. *Appl. Energy* **2020**, *280*, 115911. https://doi.org/10.1016/j.apenergy.2020.115911.
167. Maoulida, F.; Guilbert, D.; Camara, M.B.; et al. Dynamic electrical degradation of PEM electrolyzers under renewable energy intermittency: Mechanisms, diagnostics, and mitigation strategies—A comprehensive review. *Renew. Sustain. Energy Rev.* **2026**, *225*, 116170. https://doi.org/10.1016/j.rser.2025.116170.
168. Li, A.; Ooka, H.; Kong, S.; et al. Oxygen evolution electrocatalysis resilient to voltage fluctuations. *Nat. Sustain.* **2025**, *8*, 1533–1540. https://doi.org/10.1038/s41893-025-01665-y.
169. Veroneau, S.S.; Hartnett, A.C.; Ryu, J.; et al. A straightforward model for quantifying local pH gradients governing the oxygen evolution reaction. *J. Am. Chem. Soc.* **2024**, *146*, 28925–28931. https://doi.org/10.1021/jacs.4c09521.
170. Kim, Y.J.; Lim, A.; Kim, J.M.; et al. Highly efficient oxygen evolution reaction via facile bubble transport realized by three-dimensionally stack-printed catalysts. *Nat. Commun.* **2020**, *11*, 4921. https://doi.org/10.1038/s41467-020-18686-0.
171. Dastafkan, K.; Wang, S.; Song, S.; et al. *Operando* monitoring of gas bubble evolution in water electrolysis by single high-frequency impedance. *EES Catal.* **2023**, *1*, 998–1008. https://doi.org/10.1039/d3ey00182b.
172. Geuß, M.; Löttert, L.; Böhm, T.; et al. Quantification of iridium dissolution at water electrolysis relevant conditions using a gas diffusion electrode half-cell setup. *ACS Catal.* **2024**, *14*, 11819–11831. https://doi.org/10.1021/acscatal.4c02159.
173. Chan, A.L.; Yu, H.; Reeves, K.S.; et al. Identifying electrochemical processes by distribution of relaxation times in proton exchange membrane electrolyzers. *J. Power Sources* **2025**, *628*, 235850. https://doi.org/10.1016/j.jpowsour.2024.235850.
174. Chen, Z.; Lin, Z.; Zhu, X.; et al. Adsorbed oxygen dynamics at forced convection interface in the oxygen evolution reaction. *Nat. Commun.* **2025**, *16*, 7949. https://doi.org/10.1038/s41467-025-63181-z.
175. Knöppel, J.; Möckl, M.; Escalera-López, D.; et al. On the limitations in assessing stability of oxygen evolution catalysts using aqueous model electrochemical cells. *Nat. Commun.* **2021**, *12*, 2231. https://doi.org/10.1038/s41467-021-22296-9.
176. Tran, H.P.; Nong, H.N.; Zlatar, M.; et al. Reactivity and Stability of Reduced Ir-Weight TiO_2-Supported Oxygen Evolution Catalysts for Proton Exchange Membrane (PEM) Water Electrolyzer Anodes. *J. Am. Chem. Soc.* **2024**, *146*, 31444–31455. https://doi.org/10.1021/jacs.4c07002.
177. Lee, J.K.; Anderson, G.; Tricker, A.W.; et al. Ionomer-free and recyclable porous-transport electrode for high-performing proton-exchange-membrane water electrolysis. *Nat. Commun.* **2023**, *14*, 4592. https://doi.org/10.1038/s41467-023-40375-x.
178. Zhang, M.; An, W.; Liu, Q.; et al. Tunnel-structured IrO_x unlocks catalytic efficiency in proton exchange membrane water electrolyzers. *Nat. Commun.* **2025**, *16*, 7608. https://doi.org/10.1038/s41467-025-62861-0.
179. Weber, C.C.; Wrubel, J.A.; Gubler, L.; et al. How the porous transport layer interface affects catalyst utilization and performance in polymer electrolyte water electrolysis. *ACS Appl. Mater. Interfaces* **2023**, *15*, 34750–34763. https://doi.org/10.1021/acsami.3c04151.
180. Yang, S.; Hou, B.; Xie, Z.; et al. Influence of the porous transport layer surface structure on overpotentials in PEM water electrolysis. *Energies* **2025**, *18*, 4396. https://doi.org/10.3390/en18164396.
181. Mahajan, R.; Aleman, A.M.; Crago, C.F.; et al. A research database for experimental electrocatalysis: Advancing data sharing and reusability. *J. Chem. Phys.* **2025**, *163*, 124704. https://doi.org/10.1063/5.0280821.

182. Jiang, X.; Wang, Y.; Jia, B.; et al. Using machine learning to predict oxygen evolution activity for transition metal hydroxide electrocatalysts. *ACS Appl. Mater. Interfaces* **2022**, *14*, 41141–41148. https://doi.org/10.1021/acsami.2c13435.
183. Zlatar, M.; Escalera-López, D.; Rodríguez, M.G.; et al. Standardizing OER electrocatalyst benchmarking in aqueous electrolytes: Comprehensive guidelines for accelerated stress tests and backing electrodes. *ACS Catal.* **2023**, *13*, 15375–15392. https://doi.org/10.1021/acscatal.3c03880.
184. Sauvé, E.R.; Tang, B.Y.; Razdan, N.K.; et al. Open circuit potential decay transients quantify interfacial pH swings during high current density hydrogen electrocatalysis. *Joule* **2024**, *8*, 728–745. https://doi.org/10.1016/j.joule.2024.01.004.
185. Zhao, Y.; Cai, X.; Liu, S.; et al. Investigation of Metal-Doped IrO_2 in Rotating Disk Electrode and Membrane Electrode Assembly Configurations for Acidic Oxygen Evolution Reaction. *J. Phys. Chem. C* **2024**, *128*, 17552–17562. https://doi.org/10.1021/acs.jpcc.4c04447.
186. Wu, L.; Huang, W.; Li, D.; et al. Unveiling the structure and dissociation of interfacial water on RuO_2 for efficient acidic oxygen evolution reaction. *Angew. Chem.* **2025**, *137*, e202413334. https://doi.org/10.1002/ange.202413334.
187. Tao, Y.; Utsunomiya, T.; Yu, H.; et al. Multimodal operando characterization of cation effects at the iridium oxide–electrolyte interface for alkaline water oxidation. *ACS Appl. Mater. Interfaces* **2026**, *18*, 15699–15710. https://doi.org/10.1021/acsami.5c22249.
188. Spitzenpfeil, H.; Neumann, M.; Hausen, N.; et al. Artificial Intelligence-Assisted Experimental Optimization of Water Oxidation Catalysts. *Chem. Ing. Tech.* **2025**, *97*, 472–478. https://doi.org/10.1002/cite.202400156.
189. Gong, M.; Na, Y. Localized oxygen evolution and transport analysis in PEM water electrolysis on local static pressure, temperature and current density. *Int. J. Hydrogen Energy* **2024**, *68*, 1240–1250. https://doi.org/10.1016/j.ijhydene.2024.04.273.
190. Mohamed, A.; Ibrahem, H.; Kim, K. Machine learning-based simulation for proton exchange membrane electrolyzer cell. *Energy Rep.* **2022**, *8*, 13425–13437. https://doi.org/10.1016/j.egyr.2022.09.135.
191. Sayed-Ahmed, H.; Keller, R.; Toldy, Á.I.; et al. Data-driven degradation analysis of proton exchange membrane electrolyzer stacks under dynamic load operation. *Energy AI* **2026**, *25*, 100790. https://doi.org/10.1016/j.egyai.2026.100790.
192. Sayed-Ahmed, H.; Toldy, Á.I.; Santasalo-Aarnio, A. Dynamic operation of proton exchange membrane electrolyzers—Critical review. *Renew. Sustain. Energy Rev.* **2024**, *189*, 113883. https://doi.org/10.1016/j.rser.2023.113883.
193. Zhong, G.; Xu, S.; Fang, B. Improved oxygen evolution reaction for high-current PEM water electrolysis. *Chem Catal.* **2024**, *4*, 100897. https://doi.org/10.1016/j.checat.2023.100897.
194. Hasa, B.; Aryal, U.R.; Higashi, S.; et al. Porous transport layer influence on overpotentials in PEM water electrolysis at low anode catalyst loadings. *Appl. Catal. B Environ. Energy* **2025**, *361*, 124616. https://doi.org/10.1016/j.apcatb.2024.124616.
195. Milosevic, M.; Dam, A.P.; Rogler, M.; et al. Experimental-modeling framework to unveil iridium degradation pathways during intermittent operation in PEMWE. *Joule* **2026**, *10*, 102309. https://doi.org/10.1016/j.joule.2025.102309.
196. Kimmel, B.; Morawietz, T.; Biswas, I.; et al. Investigation of the degradation phenomena of a proton exchange membrane electrolyzer stack by successive replacement of aged components in single cells. *ACS Sustain. Chem. Eng.* **2025**, *13*, 4330–4340. https://doi.org/10.1021/acssuschemeng.4c07358.
197. Wang, C.R.; Kwon, O.; Spencer, J.; et al. Predictors of membrane electrode assembly activity for iridium oxide catalysts in proton exchange membrane water electrolysis. *ACS Catal.* **2026**, *16*, 12984–12994. https://doi.org/10.1021/acscatal.6c00883.
198. Chan, A.L.; Hayden, S.C.; Harvey, S.P.; et al. Mechanism-informed breakdown: Understanding degradation by controlling voltage-hold patterns in proton exchange membrane water electrolyzers. *ACS Appl. Energy Mater.* **2026**, *9*, 924–937. https://doi.org/10.1021/acsaem.5c03160.